Optical properties of localized excitons in semiconductor nanostructures

Leosson, Kristjan

Publication date:
2002

Document Version
Publisher's PDF, also known as Version of record

Optical properties of localized excitons in semiconductor nanostructures

Ph.D. Thesis

Kristján Leósson

Research Center COM, Technical University of Denmark

November 2001

Abstract

This Ph.D. thesis describes optical investigations of localized excitons in III-V semiconductor nanostructures, with a particular focus on three-dimensional localization in two types of self-organized systems; quantum wells with thickness fluctuations and self-assembled quantum dots.

The impact of in-plane exciton localization on the optical spectra of quantum wells with imperfect interfaces was investigated, using GaAs/AlAs quantum wells with different length scales of interface roughness. Exciton confinement was also probed on a sub-micrometer scale, using microscopic photoluminescence measurements. Spatially localized and spectrally narrow emission lines were observed, indicative of quantum-dot like exciton states. Measurements of the spectral PL linewidth of individual states were supplemented by time-resolved speckle analysis of secondary emission from the localized excitons, providing information about the homogeneous linewidth of the exciton transition.

Excitons localized in self-assembled III-V quantum dots were also studied. Microphotoluminescence spectroscopy on small ensembles of quantum dots revealed a broad distribution of PL linewidths, which was attributed to spectral fluctuations of the individual emission lines due to fluctuating charges in the vicinity of the dots. The homogeneous linewidth of the self-assembled quantum dots was measured using four-wave mixing techniques, demonstrating that the homogeneous broadening is only a fraction of typically observed PL linewidths at low temperature. With increasing temperature, however, the homogeneous linewidth increases rapidly and analysis of the temperature dependence suggests that exciton-LO phonon coupling in the dots is the main scattering mechanism at elevated temperatures in the types of quantum dots studied here.

Experimental apparatus for measuring photoluminescence with high spatial and spectral resolution at low temperature was constructed as a part of this Ph.D. project. Processing techniques were also developed to improve the spatial resolution beyond the diffraction limit of the optical detection. As this thesis demonstrates, spatially resolved microphotoluminescence provides a useful tool for optical investigations of localized excitons in nanostructures. High spectral resolution is generally not sufficient, however, to obtain accurate information about the natural linewidth of sharp emission lines from localized excitons, due to the fact that the quantum-dot energy levels are highly sensitive to variations in the local environment.

Resumé

Denne afhandling beskriver optiske undersøgelser af lokaliserede excitoner i III-V halvleder nanostrukturer. Det drejer sig især om tredimensional lokalisering af excitoner i to typer af selvorganiserede systemer, nemlig kvantebrønde med fluktuerende lagtykkelse og såkaldte selv-dannede kvantepunkter.

Optiske spektre af GaAs/AlGaAs kvantebrønde med grænseflader, der er ru på forskellige længdeskalaer, er blevet undersøgt for indvirkningen af exciton lokalisering i planen. Exciton lokalisering er også blevet studeret med stor rumlig opløsning ved hjælp af mikro-fotoluminescens. Rumligt lokaliserede og spektralt smalle emissionslinier er blevet observeret, hvilket antyder, at de stammer kvantepunkt-lignende exciton tilstande. Målinger af de spektrale liniebredder i fotoluminescens fra individuelle tilstande er blevet suppleret af speckle analyse af den sekundære emission fra de lokaliserede excitoner for at samle information om exciton overgangenes homogene liniebredde.

Excitoner, der er indesluttet i selv-dannede kvantepunkter er også blevet studeret. Mikro-fotoluminescens spektroskopi på små ensembler af kvantepunkter afslører en fordeling af fotoluminescens liniebredder, som er tilskrevet spektrale fluktuationer af de enkelte linier på grund af ladningsfluktuationer i kvantepunkternes omegn. Den homogene liniebredde af selv-dannede kvantepunkter er også målt ved hjælp af firebølge-blanding, hvilket afslører, at den homogene liniebredder kun er en brøkdel af den observerede fotoluminescens liniebredde ved lav temperatur. Ved stigende temperatur vokser den homogene liniebredde imidlertid hastigt, og en analyse af temperaturafhængigheden antyder, at exciton LO-fonon vekselvirkning i kvantepunkterne er den dominerende spredningsmekanisme ved højere temperaturer i den type kvantepunkter, der her er studeret.

Det eksperimentelle apparatur til måling af fotoluminescens ved lav temperatur med høj rumlig og spektral opløsning er blevet konstrueret som en del af projektet, ligesom de nødvendige proces teknikker for at passere diffraktionsgrænsen for den rumlige opløsning i den optiske detektion er blevet udviklet. Denne afhandling demonstrerer at mikro-fotoluminescens med stor rumlig opløsning er et nyttigt værktøj til optisk karakterisering af lokaliserede excitoner i halvleder nanostrukturer. Høj spektral opløsning er imidlertid i almindelighed ikke nok til at bestemme den naturlige liniebredde af skarpe emissionslinier fra lokaliserede excitoner. Dette skyldes at energiniveauerne for kvantepunkter er meget følsomme overfor variationer i de lokale omgivelser.

Preface

The work presented in this thesis was carried out in the Optoelectronics group at Research Center COM, Technical University of Denmark under the supervision of Prof. Jørn M. Hvam. Co-supervisors were Wolfgang Langbein, presently at the University of Dortmund, and John Erland Østergaard, presently at NKT Research and Innovation A/S in Lyngby. I would like to thank all of them for their guidance and for creating a stimulating work environment. I especially thank Wolfgang Langbein for initiating a lot of the work presented in this thesis and for making the necessary arrangements for my visit to Dortmund in August-September 2000.

In addition, I thank Dan Birkedal for excellent collaboration, helpful advice, and constructive criticism. Also, I want to thank Paola Borri for stimulating discussions and companionship. I am indebted to Jesper Bo Jensen, Claus B. Sørensen and Nader Payami at the III-V NanoLab for introducing me to electron-beam lithography and cleanroom processing and Fleming Jensen at the Microelectronic Center for providing the atomic-force microscope. I thank visiting scientists Leigh Smith and Yu Ping for a good collaboration. Jacob Riis Jensen deserves thanks, along with Claus Sørensen and Zhangcheng Xu, for growing the wafers used in this work. In addition, I thank Stig Pedersen at the Microelectronic Center for devoting many hours to machining parts for the micro-PL apparatus.

Last but not least, I thank my parents for their invaluable support throughout my studies, and my wife and daughter for standing by me through thick and thin, and for bearing with my absence during the long hours in the lab and during the writing of this thesis.

Copenhagen, November 2001
Kristján Leósson

Publications authored and co-authored during the course of the ph.d. project:

Refereed Journals

K. Leosson, D. Birkedal, J.M. Hvam: *Homogeneous linewidth of self-assembled III-V quantum dots observed in single-dot photoluminescence*, submitted to Phys. Rev. B.

D. Birkedal, K. Leosson, J.M. Hvam: *Long-lived coherence in self-assembled quantum dots*, Phys. Rev. Lett. 87, 227401 (2001).

S.I. Bozhevolnyi, V. Volkov, K. Leosson: *Surface plasmon polariton propagation along a 90° bent line defect in a periodically corrugated metal surface*, Optics Communications 196, 41 (2001).

S.I. Bozhevolnyi, V. Volkov, K. Leosson, A. Boltasseva: *Bend Loss in Surface Plasmon Polariton Band Gap Structures*, Appl. Phys. Lett. 79, 1076 (2001).

S.I. Bozhevolnyi, V. Volkov, K. Leosson, J. Erland: *Observation of surface plasmon polaritons along line defects in a periodically corrugated metal surface*, Opt. Lett. 26, 734 (2001).

S.I. Bozhevolnyi, J. Erland, K. Leosson, P.M.W. Skovgaard, J.M. Hvam: *Waveguiding in surface plasmon polariton band bap structures*, Phys. Rev. Lett. 86, 3008 (2001).

W. Langbein, K. Leosson, J.R. Jensen, J.M. Hvam, R. Zimmermann: *Instantaneous Rayleigh scattering from excitons localized in monolayer islands*, Phys. Rev. B 61, R10555 (2000).

K. Leosson, W. Langbein, J.M. Hvam: *Exciton localization and interface roughness in growth-interrupted GaAs/AlAs quantum wells*, Phys. Rev. B 61, 10322 (2000).

H.P. Wagner, H.-P. Tranitz, H. Preis, W. Langbein, K. Leosson, J.M. Hvam: *Exciton dephasing and biexciton binding in CdSe/ZnSe islands*, Phys. Rev. B 60, 10640 (1999).

P. Yu, W. Langbein, K. Leosson, J.M. Hvam, N.N. Ledentsov, D. Bimberg, V.M. Ustinov, A.Yu. Egorov, A.E. Zhukov: *Optical anisotropy in vertically coupled quantum dots*, Phys. Rev. B 60, 16680 (1999).

Conference Proceedings

K. Leosson, D. Birkedal, J.M. Hvam: *Dephasing in self-organized InAlGaAs quantum dots*, to be published in Physica Scripta (2001).

K. Leosson, D. Birkedal, J.M. Hvam: *Four-wave mixing in InAlGaAs quantum dots*, Quantum Electronics and Laser Science Conference, OSA Technical Digest (Optical Society of America, Washington DC, 2001) p. 38.

S.I. Bozhevolnyi, J. Erland, K. Leosson, P.M.W. Skovgaard, J.M. Hvam: *Surface plasmon polariton band gap structures: Implications to integrated plasmonic circuits*, ibid., p. 171.

B. Vohnsen, S.I. Bozhevolnyi, K. Pedersen, J. Erland, J.R. Jensen, K. Leosson, J.M. Hvam: *Scanning second-harmonic optical microscopy of self-assembled InGaAs quantum dots*, ibid., p. 135.

L.M. Smith, K. Leosson, J. Erland, J.R. Jensen, J.M. Hvam, V. Zwiller: *Excited state dynamics in InAlGaAs/AlGaAs self-assembled quantum dots*, phys. stat. sol. (b) 224, 447 (2001).

W. Langbein, K. Leosson, J.R. Jensen, J.M. Hvam: *Instantaneous Rayleigh-scattering from excitons localized in monolayer islands*, IQEC 2000 Conference Digest (Nice, France, 2000), p. 69.

K. Leosson, J. Erland, J.R. Jensen, J.M. Hvam: *Exciton dephasing in single InGaAs quantum dots*, Quantum Electronics and Laser Science Conference, OSA Technical Digest (Optical Society of America, Washington DC, 2000), p. 56.

K. Leosson, J.R. Jensen, J.M. Hvam, W. Langbein: *Linewidth statistics of single InGaAs quantum dot photoluminescence lines*, phys. stat. sol. (b) 221, 49 (2000).

Other scientific contributions

D. Birkedal, K. Leosson, J.M. Hvam: *Long-lived coherence in self-assembled quantum dots*, 1300-nm GaAs Workshop and COST 268 MC/WG Meetings (Lecce, Italy, 2001).

K. Leosson and J.M. Hvam: *Quantum dots for optoelectronics*, DOPS-NYT 2, 30 (2001).

J. Erland, S.I. Bozhevolnyi, V.S. Volkov, K. Leosson, J.J. Larsen, J.R. Jensen, J. Broeng, H. Simonsen, A. Bjarklev, P.M.W. Skovgaard, A. Boltasseva, J.M. Hvam: *Photonic bandgap components in optical communication*, Nonlinear Devices and Applications to Photonics (Munich, Germany 2001), invited.

K. Leosson, J.E. Østergaard, J.R. Jensen, J.M. Hvam, *High-resolution photoluminescence studies of single semiconductor quantum dots*, Northern Optics 2000 Program and Summaries of Contributions (Uppsala, Sweden, 2000), p. 148.

K. Leosson, J. Erland, J.R. Jensen, J.M. Hvam: *Photoluminescence studies of single InGaAs quantum dots*, poster presentation, Annual Meeting of the Danish Optical Society, Lyngby (1999).

J. Erland, K. Leosson, J.M. Hvam, N.H. Bonadeo, D. Gammon, D.S. Katzer, D.G. Steel: *Decoherence Times and Distributions in Single and Few Quantum Dot Systems*, poster presentation, NRL Workshop "Physics of Quantum Dots for Quantum Computing", Washington D.C. (1999).

K. Leosson, W. Langbein, J.R. Jensen, J. Hvam: *Photoluminescence and interface roughness in GaAs/AlAs quantum wells*, poster presentation, Annual Meeting of the Danish Optical Society, Aalborg (1998).

Contents

1 Introduction

Den Guds klarsyn falder på
ser det store i det små
Piet Hein

Over the past 15 years, studies of semiconductor quantum dots have evolved from a minor curiosity to becoming one of the major research fields within semiconductor science. In the year 2000, nearly 7% of all internationally published papers within semiconductor science and technology referred to quantum dots.[1] Quantum dots, which bear a strong similarity to atomic systems, not only provide an excellent system for the study of "engineered atoms" but a wide range of possible technological applications has also been suggested. These include using quantum dots as building blocks for quantum computers [1] or neural networks [2], as fluorescent tags for biological labeling [3, 4], as well as spin filters and single-spin memory units [5].

One of the main areas of quantum dot research has been in optoelectronic devices. Quantum dots have been used as single photon detectors in the far-infrared [6], as elements of a miniature integrated spectrometer [7], as optical memory devices [8], and as single photon emitters [9, 10, 11], e.g. for quantum cryptography applications, to name a few examples. Semiconductor lasers using quantum dots as the active material were initially predicted to show a performance superior to bulk or quantum well lasers [12, 13], e.g. lower threshold current and temperature insensitive operation. While significant technological progress has been made from the initial realization of laser diodes based on patterned and etched GaInAsP dots in 1987 [14] and self-organized InGaAs quantum dots in 1994 [15], quantum dot lasers have yet to fulfill the promise of significantly improved performance over quantum well lasers. However, they are at the threshold of becoming a viable alternative to standard technologies in several areas of application.

[1] Source: INSPEC

This thesis will address some of the fundamental physical properties of localized excitons in semiconductor nanostructures, using optical characterization of two different material systems; disordered quantum wells and self-assembled quantum dots. An overview of the basic physics, fabrication techniques and the electronic and optical properties of these nanostructures is given in Chapter 2. Chapter 3 describes the techniques used for growing and processing the samples, as well as the different optical characterization methods used. Investigations of exciton localization in quantum wells with different length scales of interface roughness are described in Chapter 4. Chapter 5 focuses on excitons confined in self-assembled quantum dots. The work is summarized in Chapter 6.

2 Semiconductor nanostructures: Fabrication, structure, and optical properties

Studies of the optical properties of objects smaller than the wavelength of light have a long history. In 1871, light scattering from small particles was found to be responsible for the blue color of the sky, as explained by J. W. Strutt (later Lord Rayleigh) [16]. The same principle was applied to optical filters in 1884, using sub-wavelength-sized particles suspended in a liquid (Christiansen filter[2]) [17]. Different kinds of sub-micron-sized crystals embedded in glass have been widely used in optics for decades to make color filters, where a special heat treatment is required for the crystals to reach the proper size [18]. It was not until 1985, however, that semiconductor microcrystals with controlled sizes down to tens of nanometers were conclusively shown to exhibit a "quantum size effect," i.e. a blue-shift of absorption features directly related to a quantum-mechanical confinement of the electronic wavefunctions in the crystals [19]. At this time, similar effects had already been demonstrated in the absorption spectra of layered semiconductor heterostructures grown by epitaxial techniques [20] which today form the active part of most commercial semiconductor lasers and many types of advanced electronic devices.

The term *nanostructure* is commonly used to describe systems where quantum size effects are observed, since this requires potential variations on a length scale of no more than a few tens of nanometers in at least one dimension. Using present-day terminology, the full range of low-dimensional semiconductor nanostructures is represented by *quantum wells*, where charge carriers are free to move in two dimensions, *quantum wires*, where carriers are confined in two dimensions and free to move only in one dimension and, ultimately, *quantum dots*, where the carriers are fully localized in three dimensions. This thesis deals with optical properties of localized excitons in semiconductor nanostructures. Below, basic concepts in optics of bulk and low-dimensional semiconductors of relevance to the present work will be introduced (Sec. 2.1). Sec. 2.2 describes methods that have been developed to fabricate quantum dot structures in a variety of material systems while Secs. 2.3 and 2.4 give a more detailed description of the structural, electronic and optical properties of the types of nanostructures that are investigated in this thesis.

[2] After C. Christiansen, professor at the *Polytekniske Læreanstalt* in Copenhagen which later became DTU.

Unless otherwise noted, the material in this chapter is based on standard texts in semiconductor physics and optics [22, 23, 24, 25, 26, 27], as well as recent books and reviews on quantum dot systems [28, 29, 30], which the reader can consult for further information. I thank Jacob Riis Jensen, Wolfgang Langbein, Ingibjörg Magnúsdóttir, and Robson Ferreira for providing the code used for model calculations in Sec. 2.4.2.

2.1 Optics of semiconductors and semiconductor nanostructures

2.1.1 Band structure

The concept of a band structure in solids arises from the periodic structure of the crystalline lattice. Electrons moving in a periodic potential propagate only within certain allowed bands of energy. The eigenfunctions of an electron in the crystal (Bloch functions) can be expressed as products of a plane wave $\exp(\mathrm{i}\mathbf{k}\cdot\mathbf{r})$ and a function that has the periodicity of the crystal lattice. The energy bands are conveniently described in reciprocal space, where the electron energy is expressed in terms of the wavevector $\mathbf{k}$. In semiconductors, a band of forbidden energies exists between the highest occupied electron band (valence band) and the lowest unoccupied band (conduction band). In the so-called direct-gap semiconductors, e.g. GaAs, the extrema of these bands in reciprocal space coincide at $k = 0$. To a first approximation, the conduction band around $k = 0$ can be described as parabolic, with $E \propto k^2$ as for free electrons. Electrons that occupy states close to the bottom of the conduction band can therefore be treated as free particles with an *effective mass* which is inversely proportional to the curvature of the energy band in k-space. Describing the dynamics of electrons in crystals in this manner is referred to as the *effective mass approximation*.

If an electron is removed from the valence band, it leaves a positively charged *hole*, which also can be described as a free particle with an effective mass defined by the curvature of the valence band. In most semiconductors, the effective mass of electrons is lower than that of holes, and both are lower than the free electron mass, m_0. In GaAs and InAs, the valence band at $k = 0$ actually consists of three bands with different curvature. Due to the spin-orbit interaction, one of these bands is shifted to lower energy, leaving the top of the valence band in the bulk crystal two-fold degenerate (four-fold degenerate when spin is included). The two degenerate bands have different masses and are referred to as the heavy-hole and light-hole bands. Furthermore, the valence bands are not isotropic, i.e. the effective mass depends on the direction of the k-vector relative to the crystal axes.

In semiconductor heterostructures, a spatial modulation of the conduction and valence band energies is introduced by varying the chemical composition of the structure. In the simple case of a quantum well, a layer of material with lower bandgap is sandwiched between layers with a higher bandgap. As a result, a potential well with finite barriers is

formed, both for electrons in the conduction band and for holes in the valence band.[3] If the quantum well thickness is significantly larger than the interatomic spacing, then the effective mass approximation is still valid. Electrons and holes in a (perfect) quantum well can then be described as particles in a one-dimensional box with finite potential barriers, which is a standard exercise in elementary quantum mechanics. The confinement results in a finite quantization energy which increases the separation of the conduction and valence bands in the well by a value depending on the well thickness. The quantization energies of the confined particles also depend on their effective masses and the confinement therefore results in a lifting of the valence band degeneracy, pushing the light-hole band further down in energy.

Usually, semiconductor heterostructures are grown in a single-crystal configuration using materials with closely matched lattice constants, such as AlGaAs on GaAs substrates or InGaAsP on InP substrates. Nevertheless, heterostructures containing materials with different lattice constants *can* be grown as a single crystal, provided that the layers are thin and the lattice mismatch is not too large. In this case, however, a part of the heterostructure will be strained. Strain implies a modification of the periodicity of the lattice, resulting in a change of the lattice constant and a reduction of symmetry, compared to the unstrained crystal. Consequently, the curvature and position of the conduction and valence bands will be changed. If the crystal symmetry is reduced, the strain will affect the valence bands differently. In compressively strained quantum wells, for example, the light hole band is pushed away from the band edge and the heavy hole mass is reduced considerably. This fact has been used advantageously to improve the performance of semiconductor lasers by using strained InGaAs quantum wells as the active medium.

2.1.2 Excitons

In a bulk semiconductor, an electron in the valence band can be excited to the conduction band, e.g. by the absorption of a photon with an energy exceeding the bandgap. Momentum conservation implies that the electron gains energy but remains in roughly the same position in k-space, since the momentum of the absorbed photon is relatively small. Transfer of electrons between the top of the valence band to the bottom of the conduction band is therefore particularly efficient in direct-gap semiconductors where the band extrema coincide in k-space. The Coulomb interaction between electrons and holes in semiconductors has profound effects on their optical properties, in particular close to the absorption edge. Electrons and holes can pair together and form *excitons*. The exciton

[3] Other types of quantum wells exist but will not be discussed here.

envelope function in a perfect lattice satisfies the two-particle Schrödinger equation:[4]

$$\left[-\frac{\hbar^2}{2m_e}\nabla_e^2 - \frac{\hbar^2}{2m_h}\nabla_h^2 - \frac{e^2}{\epsilon|\mathbf{r}_e - \mathbf{r}_h|}\right]\Phi(\mathbf{r}_e, \mathbf{r}_h) = \mathcal{E}\Phi(\mathbf{r}_e, \mathbf{r}_h), \tag{1}$$

where m_e and m_h are the effective masses of the electron and the hole, respectively, $\mathbf{r}_e$ and $\mathbf{r}_h$ are their positions, and $\mathcal{E}$ is the exciton energy, measured relative to the bandgap energy, E_g. The dielectric screening of the lattice is included through the background dielectric constant, ϵ. Equation (1) separates into parts that depend on the relative and center-of-mass coordinates of the exciton $\Phi(\mathbf{r}_e, \mathbf{r}_h) = \psi(\mathbf{r})\Psi(\mathbf{R})$, with

$$\mathbf{r} = \mathbf{r}_e - \mathbf{r}_h \quad \text{and} \quad \mathbf{R} = \frac{m_e\mathbf{r}_e + m_h\mathbf{r}_h}{M}, \tag{2}$$

respectively, where $M = m_e + m_h$ is the total exciton mass. The equation for the center-of-mass motion becomes

$$-\frac{\hbar^2}{2M}\nabla_R^2\Psi(\mathbf{R}) = \mathcal{E}_R\Psi(\mathbf{R}), \tag{3}$$

which is the equation of motion for a free particle of mass M. The relative motion is described by the *Wannier equation*, which is identical to the Schrödinger equation for the hydrogen atom:

$$\left[-\frac{\hbar^2}{2\mu}\nabla_r^2 - \frac{e^2}{\epsilon r}\right]\psi(\mathbf{r}) = \mathcal{E}_r\psi(\mathbf{r}). \tag{4}$$

The reduced mass of the exciton, μ, is given by $1/\mu = 1/m_e + 1/m_h$. Analogous to the hydrogen atom, the exciton has a Bohr radius and a binding energy (Rydberg energy), given by

$$a_B = \frac{\epsilon\hbar^2}{\mu e^2} \quad \text{and} \quad E_B = \frac{\hbar^2}{2\mu a_B^2}. \tag{5}$$

Due to the low effective masses and high dielectric constants in semiconductor crystals, exciton radii are much larger than the Bohr radius of the hydrogen atom and depend strongly on the material in question, varying from 0.7 nm in wide-band (ionic) semiconductors like CuCl to 70 nm in narrow-band (covalent) materials like InSb. Of particular importance in the present context are GaAs, with $a_B = 14\,\text{nm}$ and $E_B = 4\,\text{meV}$, and InAs, where $a_B = 50\,\text{nm}$ and $E_B = 1\,\text{meV}$.

In low-dimensional nanostructures, Eq. (1) must be modified to take into account the spatial variation of the electron and hole potentials. In quantum wells, for example, $\Phi(\mathbf{r}_e, \mathbf{r}_h)$ separates into two-dimensional relative and center-of-mass envelope functions, as well as the envelope functions in the confinement direction. In the truly two-dimensional limit, the (in-plane) radius of the exciton is reduced by a factor of two compared to the

[4] Only excitons which extend over several lattice constants (Wannier excitons) are considered here, justifying the use of the effective mass approximation. The complete wavefunction of a Wannier exciton is constructed from the envelope function $\Phi(\mathbf{r}_e, \mathbf{r}_h)$ and the atomic parts of the Bloch function for the electron and hole.

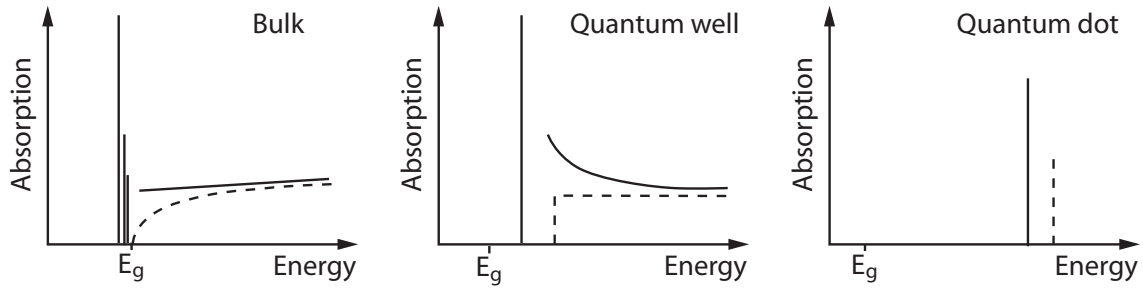

Figure 1: Schematic illustrations of absorption spectra in bulk and low-dimensional semiconductors. The dashed lines show the free carrier absorption and the solid lines indicate the Coulomb enhancement.

bulk value. Correspondingly, the two-dimensional exciton binding energy is increased fourfold. Real quantum wells are not truly two-dimensional and do not have infinite confinement potentials. The binding energy of quantum well excitons therefore increases from the three dimensional value with decreasing well width, but eventually drops again and approaches the exciton binding energy of the barrier material as a larger part of the envelope function penetrates into the barriers. In quantum dots, exciton binding energies depend strongly on the dot geometry. However, unlike the higher-dimensional cases, carriers in a quantum dot have no freedom of movement in any direction. Therefore, the binding energy of an exciton that is strongly confined in a quantum dot does not represent the energy needed to dissociate the electron and hole, but rather the Coulomb-induced shift of the uncorrelated electron and hole energy levels in the dot.

Figure 1 shows schematically the effect of the Coulomb interaction on the optical response of bulk and low-dimensional semiconductors. The free-carrier absorption, which is proportional to the joint electron and hole density of states, is shown with dashed lines. When excitonic effects are included, strong absorption lines appear below the free-carrier absorption edge and the absorption above the band edge is enhanced. The increased oscillator strength at the band edge is primarily related to the ground-state exciton transition (lowest eigenstate of Eq. (4)). In the three-dimensional case, excited exciton states are also shown, whereas in two dimensions their relative absorption strength drops more sharply and they are seldom of importance. In quantum dots, the density of states consists only of discrete energy levels. The position of the electron-hole ground state is shifted with respect to the unperturbed electron and hole levels due to the Coulomb attraction. In the limit of strong confinement, however, this effect is small compared to the confinement energy of the particles and, to a first approximation, the electron and hole wavefunctions are not affected. In reality, features of the absorption spectra are also subject to different broadening mechanisms and, in the case of low-dimensional semiconductors, complicated by appearance of excited states of the confined system and lifting of the valence band degeneracy.

2.1.3 Phonons

The interaction between quantized vibrational modes (phonons) and electrons or holes in semiconductor crystals allows for exchange of energy and momentum between the carriers and the lattice and, therefore, has a large impact on the carrier dynamics. Materials that crystallize in the zincblende structure (including GaAs, InAs, and AlAs) have two types of phonons, acoustic and optical, with distinctly different dispersion relations. Each type of phonon has three separate branches, depending on the direction of lattice vibration relative to the direction of the phonon wave vector, $\mathbf{q}$. Along main crystal directions, one can define two transverse acoustic (TA) branches and one longitudinal acoustic (LA) branch, with a dispersion close to $\nu = cq$ for small values of q, where c refers to the speed of sound in the material. The energies of the two transverse optical (TO) branches and the longitudinal optical (LO) branch, however, have a finite value at $q = 0$ and do not depend strongly on the wavevector. In GaAs and InAs, the LO-phonon energies are close to 30 meV.

The mechanism of the carrier-phonon interaction depends on the type of phonons involved. Long-wavelength acoustic phonons generate a periodic deformation of the crystal which affects the band structure (as periodically modulated strain). In materials lacking inversion symmetry, the deformation also induces a macroscopic polarization. These perturbations result in carrier-acoustic-phonon interactions that are referred to as the deformation potential and piezoelectric interactions, respectively. Optical phonons involve only relative displacements of atoms within the unit cell, which, in a zincblende structure, have opposite charge. Macroscopically, transverse optical phonons are associated with planes of opposite charge sliding parallel to each other, which induces no overall polarization. In GaAs, TO phonons couple only to valence bands, via a deformation potential interaction. For longitudinal optical phonons, however, the distance between the planes of opposite charge oscillates, resulting in a macroscopic polarization in the crystal. The resulting coupling to the valence and conduction bands is called the Fröhlich interaction. The Fröhlich interaction is the dominant mechanism of carrier relaxation in bulk and low dimensional semiconductors (with the possible exception of quantum dots, as discussed below). In the case of excitons, the LO-phonon coupling is expected to vanish if $m_e = m_h$, due to its polar nature. Generally, however, $m_e \neq m_h$ and an exciton-LO-phonon coupling exists, which is maximized when the inverse phonon wavevector matches the exciton radius.

In semiconductor heterostructures, the different materials have different atomic masses and elastic properties and, therefore, different phonon modes. In nanostructures, phonon energies are modified by quantum confinement and have, for example, been used as a sensitive probe of quantum well width and interface structure [31]. Interface phonon modes have also been identified. Built-in strain changes the spring constants of the lattice and, therefore, the phonon frequencies. In strained InAs quantum dots (see Sec. 2.2), the LO-phonon branch is shifted slightly to higher energy compared to unstrained InAs. Furthermore, differences in strain and composition between individual dots result in a

broadening of the optical phonon spectrum, since each dot has a particular LO-phonon frequency.

Phonon-carrier interactions are strongly modified in quantum dots, where the carriers are confined in three dimensions. The deformation potential interaction decreases with decreasing dot size, while interface phonons play an increasingly larger role. For InAs quantum dots, exciton-LO-phonon coupling has been shown to increase, particularly for larger dots, due to the asymmetry of the electron and hole wavefunctions which increases the dipole moment of the exciton [32]. On the other hand, due to the discrete level structure of the dots, the Fröhlich interaction should be suppressed unless the energy level spacing between initial and final states in the scattering process matches an LO-phonon energy. This particular feature of quantum dot systems is referred to as the *phonon bottleneck* effect. A phonon bottleneck can result in a significantly reduced carrier relaxation rate in quantum dots, which can be detrimental to device performance. On the other hand, a reduced phonon scattering of quantum dot excitons is also expected, leading to longer coherence lifetimes as discussed in the following section. The importance of the phonon bottleneck has been heavily debated in the literature, since many observations indicate that fast relaxation and scattering take place in quantum dots, in spite of their discrete level structure.

2.1.4 Exciton coherence

Between the creation and annihilation of an electron-hole pair in a semiconductor, carrier diffusion and different scattering processes come into play. These processes, along with the density of available states, determine the spatial and temporal carrier dynamics in the system. Immediately following the excitation of an electron-hole pair by a coherent light field, the pair forms an oscillating dipole having a well-defined phase with respect to the incident field. This phase relationship is destroyed, however, as soon as the carriers interact with a "bath" of phonons or other carriers. Through interactions with the environment, electrons and holes eventually reach a thermal distribution in equilibrium with the lattice. Electron-hole pairs in the crystal will also recombine, either radiatively by photon emission or non-radiatively by other means, returning the crystal to its ground state.

Coherent dynamics in semiconductors are often discussed in terms of short-pulse resonant excitation of exciton states. The system is described as an ensemble of two-level oscillators, where the lower level is the ground state of the crystal and the upper level is the exciton state:

$$\Psi = C_1|g\rangle + C_2|e\rangle, \tag{6}$$

where C_1 and C_2 are complex coefficients. For convenience, the density matrix for the

two-level system can be written,

$$\rho = \begin{bmatrix} \rho_{22} & \rho_{21} \\ \rho_{12} & \rho_{11} \end{bmatrix} = \begin{bmatrix} C_2 C_2^* & C_2 C_1^* \\ C_1 C_2^* & C_1 C_1^* \end{bmatrix}. \tag{7}$$

The diagonal elements represent the probability of finding an individual oscillator in each of the two states, with $\rho_{11} + \rho_{22} = 1$ for an isolated system. The phase of the coherent superposition state is included in the complex off-diagonal elements $\rho_{21} = \rho_{12}^*$. For N identical two-level oscillators, $N\rho_{22}$ gives the excited state population and ρ_{21} is related to the overall degree of coherence in the ensemble. The Hamiltonian which is applied to the density matrix in order to describe the dynamics of the system can be divided into three parts,

$$\mathcal{H} = \mathcal{H}_0 + \mathcal{H}_{\text{int}} + \mathcal{H}_{\text{rel}}, \tag{8}$$

where $\mathcal{H}_0$ is the basic Hamiltonian of the two-level system, $\mathcal{H}_{\text{int}}$ accounts for the interaction with the radiation field, and $\mathcal{H}_{\text{rel}}$ describes the relaxation mechanisms of the system, e.g. spontaneous emission and elastic carrier-phonon interactions. If the oscillators do not interact with each other, then the time-dependent Schrödinger equation leads to a set of coupled equations, the *optical Bloch equations*, commonly used in atomic physics. For excitons in uncoupled quantum dots, the independent two-level oscillator picture can be considered a fair approximation. In higher-dimensional systems, however, this description is too simple. In particular, the Coulomb interaction between carriers must be included. If this is done, one arrives at the *semiconductor Bloch equations*. In essence, the Coulomb interaction modifies the first two parts of the Hamiltonian in Eq. (8), renormalizing the electron and hole energies as well as their interaction with the light field. The relaxation Hamiltonian, however, is regarded as unaffected.

The simplest and most common way to describe the relaxation Hamiltonian is by using the *relaxation-time approximation*, where $\mathcal{H}_{\text{rel}}$ is characterized by two time constants, called the longitudinal and transverse relaxation times and denoted T_1 and T_2, respectively. In an isolated two-level system, T_1 represents the radiative lifetime of the excited state while the *dephasing time*, T_2, can be understood as a lifetime of the coherent superposition state. T_2 is inversely proportional to the *homogeneous broadening* or natural linewidth of the optical transition (discussed in more detail in Sec. 3.3.1) and can also be related to the decay of the *macroscopic* polarization in a homogeneously broadened ensemble of oscillators (Sec. 3.3.2). The dephasing time depends both on T_1 and the *pure dephasing time*, commonly referred to as T_2^*. The latter is determined by *elastic* scattering events which disturb the phase of the oscillator but do not change its energy, affecting only the off-diagonal elements of the density matrix. The total dephasing rate due to population relaxation and pure dephasing is given by

$$\frac{1}{T_2} = \frac{1}{2T_1} + \frac{1}{T_2^*}. \tag{9}$$

In a realistic system, *inelastic* processes may also scatter the exciton to different states, implying a non-radiative loss of population from a particular exciton state. Conversely,

scattering *into* an exciton state increases its incoherent population. In experiments, the longitudinal relaxation time is therefore affected by the probability of scattering into or out of the ensemble of optically active states within the detection window, as well as the radiative lifetime. The transverse relaxation time, however, describes scattering between states within the detection window, in addition to the pure elastic dephasing of individual states. The two contributions to the dephasing rate are often difficult to separate experimentally. Furthermore, both T_1 and T_2^* can be affected by a number of different carrier-phonon and carrier-carrier scattering processes. Experimental techniques that have been used in this thesis to measure dephasing times of localized excitons are described in Chapter 3.

2.2 Quantum dot fabrication techniques

Quantum dots, i.e. nanostructures that result in three-dimensional carrier confinement, can be made using a variety of methods. Generally, such structures are smaller than the minimum feature size attainable with state-of-the-art optical lithography but other techniques, such as electron-beam lithography, can be used to fabricate quantum dots in a controlled fashion. Quantum dots can also form spontaneously in many systems under the right conditions.[5]

Figure 2 illustrates several ways of realizing quantum dots in semiconductor systems. Standard 2-D layer growth of quantum wells, combined with different processing techniques, can be used to generate a three-dimensional confinement potential. The quantum well can be etched, leaving a free standing quantum dot (a), grown on top of etched holes in a pre-patterned substrate (b), annealed locally using an intense pulsed laser beam (c) or strain modulated using stressors on the sample surface or buried beneath the quantum well (d). In a similar fashion, metal contacts can be deposited on the surface and through externally applied voltage, an attractive potential can be created, typically in a two-dimensional electron gas below the surface. An applied potential that is attractive for electrons repels holes and vice versa so these dots only confine one type of carrier. Complex contact geometries can be used to make special configurations or arrays of dots separated by adjustable potential barriers. Using the technique of cleaved-edge overgrowth, quantum dots can be formed at the intersection of three quantum wells grown perpendicular to each other (e). After growing each of the first two quantum wells, the sample is rotated, cleaved in vacuum and immediately overgrown with a new quantum well. Three-dimensional confinement can also be obtained in a quantum well by allowing the free surfaces to relax in order to form monolayer-high terraces at the interface between the two materials (f). A locally increased thickness of the quantum well results in a potential minimum, which can confine electrons and holes. The island size can be adjusted to obtain an optimum lateral size of potential fluctuations. Interface roughness

[5] The related case of three-dimensional exciton localization due to binding to crystal defects (see, e.g., Ref. [23]) will not be discussed here.

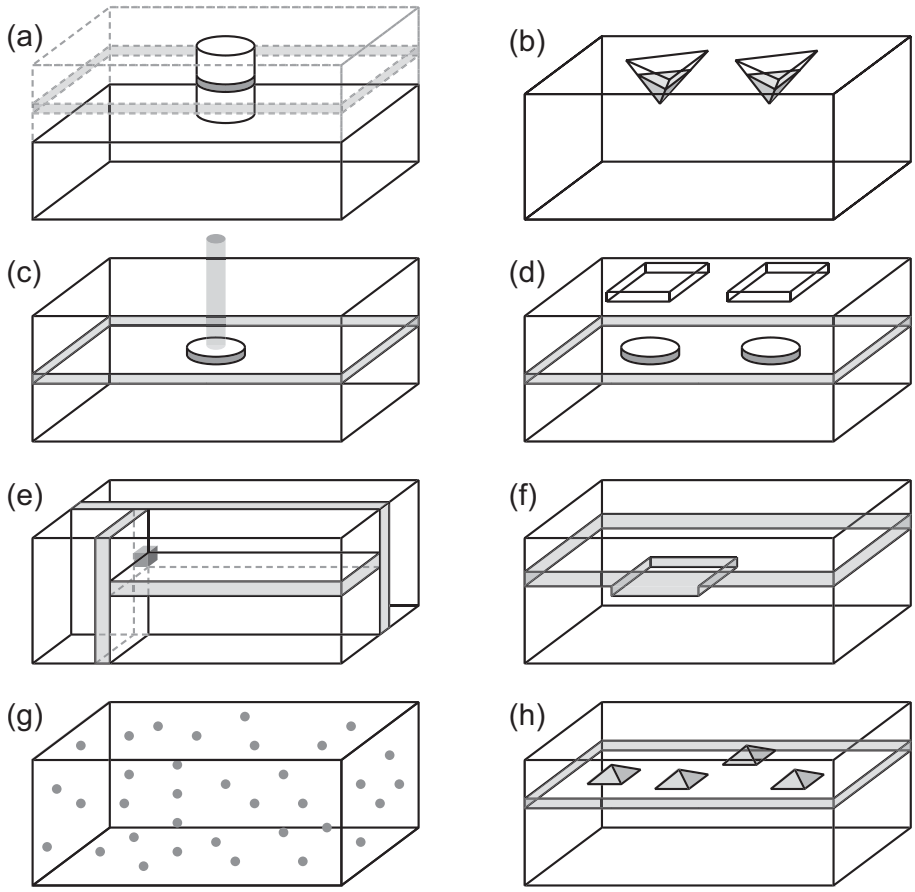

Figure 2: Fabrication methods for quantum dot structures, described in the text.

in AlAs/GaAs heterostructures is discussed in more detail below.

A common problem in most of the methods described above is that the three-dimensional confinement potential is relatively weak (few meV) and carriers are therefore only confined to the dots at cryogenic temperatures, escaping to quantum-wire or quantum-well states at higher temperatures. A minimum requirement for room-temperature operation of quantum-dot-based devices is a confinement potential which is significantly larger than the thermal energy of the carriers ($kT \approx 25\,\mathrm{meV}$). The previously mentioned microcrystals embedded in a glass matrix (Fig. 2g) provide one alternative where carriers can be strongly confined. The matrix can consist of organic or inorganic glasses as well as polymers. Semiconductor microcrystals in a conducting polymer have been used to realize optoelectronic devices such as light-emitting diodes.

The final method of fabricating quantum dots shown here involves the self-assembly of islands during epitaxial growth of lattice-mismatched materials (Fig. 2h). If a material with a larger lattice constant than the substrate is deposited under the right conditions, strain relaxation can occur through the formation of large clusters of atoms on the surface. These clusters can reach tens of nanometers in size and are commonly referred to as *self-assembled quantum dots*. In order to provide confinement for electrons and holes, the bandgap of the dot material must lie within the bandgap of the underlying (barrier) material. Following the formation of dots, the wafer can be overgrown with barrier material. Self-assembled quantum dots have been realized in many semiconductor systems; III-V's, II-VI's, nitrides, and even by growing Ge or InAs on silicon. Using this method, quantum dots with strong confinement can be embedded in a semiconductor material, compatible with standard device processing techniques and ideal for optoelectronic applications. Structural, electronic and optical properties of self-assembled quantum dots are addressed in the following sections.

2.3 Self-ordered nanostructures

Two of the fabrication techniques described above involve different self-ordering phenomena that occur on crystal surfaces during epitaxial growth. Monolayer (ML) islands at heterointerfaces and self-assembled quantum dots represent nanometer-sized structures that are formed naturally under specific growth conditions. Such structures are easily implemented in a semiconductor heterostructure and require no post-processing. Self-ordered nanostructures generally exhibit a certain degree of randomness in position, size, and shape, due to the stochastic nature of the epitaxial growth. However, the energy balance between the cost of forming extra edges or surfaces and the gain due to elastic relaxation may imply a certain optimum period in the self-ordering process, resulting in characteristic length scales in the system.

Advanced characterization techniques involving atomic-resolution microscopy and diffractive methods, both *in-situ* and *ex-situ*, are used to investigate crystal surfaces and

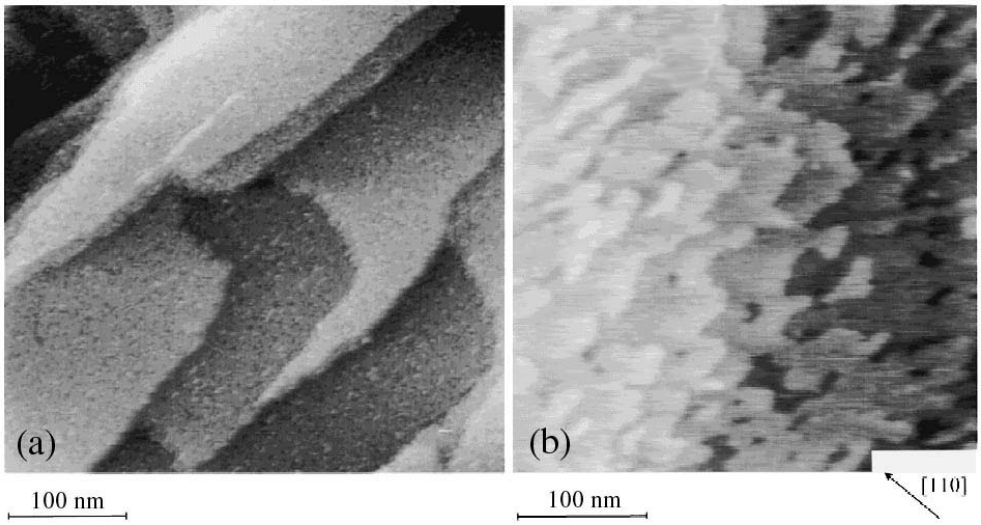

Figure 3: Scanning tunneling microscope images depicting relaxed (a) GaAs (001) and (b) AlAs (001) surfaces (from Ref. [33])

interfaces in MBE-grown structures. The most extensively studied material system for fabricating semiconductor nanostructures is the $Al_xGa_{1-x}As$ system which is ideal for heterostructure growth due to the small lattice mismatch and large bandgap difference of GaAs ($a = 0.56503\,\text{nm}$, $E_g = 1.52\,\text{eV}$) and AlAs ($a = 0.56611\,\text{nm}$, $E_g = 3.1\,\text{eV}$).[6] Strained layers with a reduced bandgap can be grown by introducing indium into the system. The lattice mismatch of GaAs and InAs ($a = 0.60583\,\text{nm}$, $E_g = 0.43\,\text{eV}$) is about 7%.

2.3.1 Quantum well interfaces

The growth of semiconductor crystals by molecular beam epitaxy is a complicated issue and not yet fully understood, despite decades of research. The roughness of interfaces between two materials has received particular attention, due to its importance in fabricating high-mobility two-dimensional electron gases as well as high-quality quantum wells and superlattices. On the atomic scale, significant surface roughness is typically present during MBE growth, resulting in imperfect interfaces when one material is grown on top of another. Growing AlAs on top of GaAs or vice versa also reveals significant differences between the formation of "normal" (AlAs on GaAs) and "inverted" (GaAs on AlAs) interfaces, due to different underlying surface kinetics that governs the interface formation [34]. Consequently, a quantum well consisting of a layer of GaAs sandwiched between layers of AlAs has a thickness variation on the atomic scale, which is defined by the structure of two interfaces with different roughness characteristics.

[6] Values of E_g given here are for $k = 0$ and temperatures approaching 0 K. AlAs actually has a lower indirect bandgap.

The roughness of the as-grown crystal surface can be reduced significantly by interrupting the MBE growth for a period of time. When growth is interrupted, surface diffusion reduces the number of atomic steps and lowers the total energy of the surface. On the other hand, even in the ultra-high vacuum of the MBE reactor, extended growth interruptions also result in an increased incorporation of impurities at the surface, which eventually deteriorates the quality of the material. Many research groups have demonstrated that within 1–2 minutes, both GaAs and AlAs surfaces can relax to form large monolayer-high islands or terraces while maintaining a reasonable purity of the material. Scanning tunneling microscope (STM) images of GaAs and AlAs surfaces, recorded after slow cooling from the growth temperature, are shown in Fig. 3. In both cases, monolayer-flat terraces are observed, extending laterally over tens or hundreds of lattice constants. In general, the surface structure can be characterized by reasonably well-defined length scales that vary for the different materials and crystal axes.

2.3.2 Strain-relaxed islands

Epitaxial growth of material A on top of a closely lattice-matched material B occurs in a layer-by-layer growth mode if the balance of surface and interface energies is such that material A *wets* the underlying material B (by analogy with a liquid wetting a solid surface). If the two materials are not lattice matched, an additional energy term due to the deformation of the crystal surface is introduced (here the analogy with liquids no longer holds since liquids are incompressible). A strained layer with a small interface energy initially grows in a layer-by-layer fashion. The strain energy increases with increasing layer thickness until it reaches a critical value, typically resulting in the formation of dislocations (crystal faults) that severely degrade the optical quality of the material. However, an alternative mechanism of energy relaxation exists, which can prevent the formation of dislocations. Under the correct growth conditions (lattice mismatch, substrate temperature, growth rate, etc.), strain-relaxed and dislocation-free islands are formed on top of a thin two-dimensional strained layer (*wetting layer*) that covers the entire surface. The height of the islands can easily reach tens of monolayers while the wetting layer thickness is only a few monolayers. In essence, the islands form because the energy associated with forming extra surfaces is smaller than the reduction in the elastic energy obtained by piling up material away from the strained interface. The details of island formation depend strongly on the material system and only the case of $In_xGa_{1-x}As$ ($0.5 \leq x \leq 1$) deposited on GaAs will be considered here.

Despite the random nature of the growth process, InGaAs and InAs islands formed on GaAs show a certain homogeneity in shape and size, which persists after extended growth interruption times. In cases where the areal density of islands is high, ordered arrays have also been observed. Structures of this kind are therefore properly classified as self-ordered nanostructures, or *self-assembled quantum dots*. For a given dot volume, an equilibrium shape exists, typically with facets defined by low-index crystal planes. InGaAs and InAs

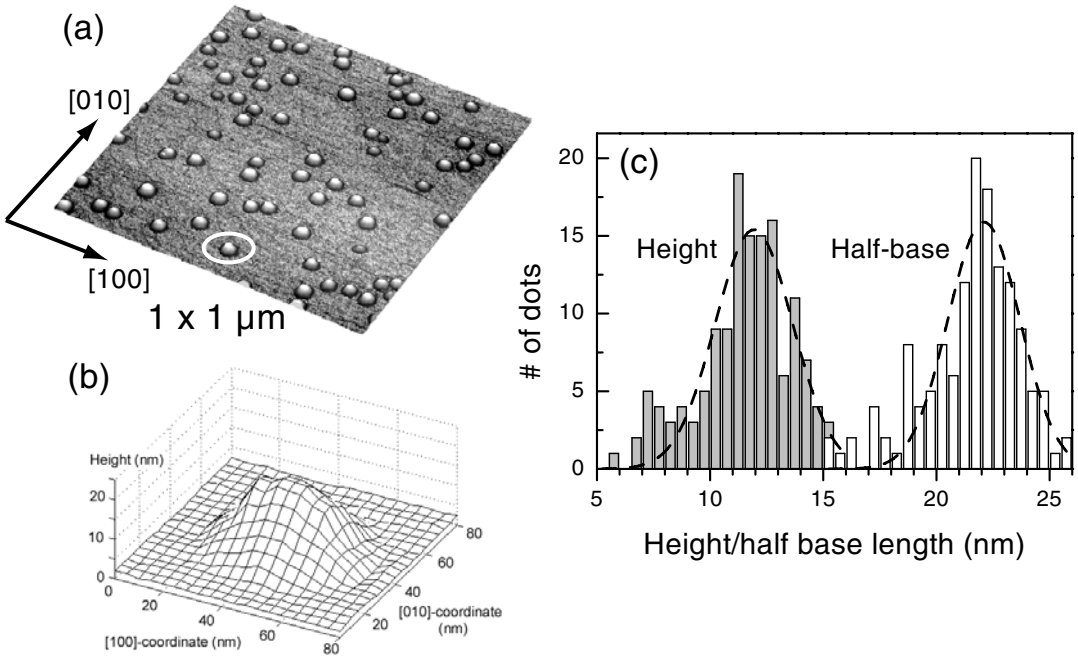

Figure 4: (a) Atomic-force microscope scan of a GaAs surface covered with $In_{0.5}Ga_{0.5}As$ quantum dots. (b) Enlarged view of a single quantum dot. (c) Distribution of heights and average base lengths for 140 dots, determined from AFM scans.

dots are most often reported as having a lens, cone, or pyramid shape, with a base length of a few tens of nanometers and a height of several nanometers. Detailed shape investigations, however, are often hampered by limited experimental resolution. Furthermore, shapes and sizes of uncapped dots are not necessarily preserved upon overgrowth. Covering strain-relaxed dots with barrier material reintroduces strain into the structure and is energetically unfavorable. Initially, therefore, the barrier material only covers the wetting layer and atoms from the dots have a tendency to evaporate onto the overgrown layer, leading to a decrease in the dot size and a segregation of indium into the barrier. If overgrowth is allowed to proceed at typical growth rates, however, the dots are eventually covered with barrier material and no further segregation occurs.

For pure InAs on GaAs, deposition of less than two monolayers is required for island formation to occur. More material is needed when depositing InGaAs alloys on GaAs, since the lattice mismatch is smaller and less strain energy is introduced per monolayer. Fig. 4a shows an atomic-force microscope (AFM) scan of a GaAs (001) surface after the deposition of 5 ML of $In_{0.5}Ga_{0.5}As$, just above the layer-to-island transition. The sample was grown uncapped, cooled rapidly, and transported in vacuum to the AFM chamber to minimize oxidation of the surface. The dot marked with a circle in Fig. 4a is shown enlarged in Fig. 4b. This dot shape, which has trapezoidal and triangular cross sections, has been referred to as a prism shape. The curvature of the AFM tip is around 0.2-0.4 nm

and the tip size therefore has only a minor influence on the observed dot shape. The facet angles vary slightly between dots but correspond roughly to the {102} and {101} crystal planes. Figure 4c shows the size distribution of 140 quantum dots. Both the height, h, and the average base length, b, are fairly well described with Gaussian distribution functions, giving $h = 12 \pm 2\,\mathrm{nm}$ and $b = 44 \pm 4\,\mathrm{nm}$, where the uncertainties cover the Gaussian full width at half maximum (FWHM). The base lengths along the two directions are similar, with $(b_{[100]} - b_{[010]})/(b_{[100]} + b_{[010]})$ lying in the range -.05 – 0.1.

Capping the dots with barrier material results in a partial evaporation of the dots and segregation of indium into the barrier, as pointed out above. Recent attempts to map the chemical profile of overgrown dots with atomic resolution have suggested significant variations in chemical composition through the quantum dot (see Ref. [35] and references therein). In InGaAs dots, a higher-than-nominal indium concentration inside the dot has been observed, suggesting that the indium is distributed non-uniformly in the dot prior to capping, presumably to minimize the elastic energy [36]. Another important consequence of overgrowth is that the previously strain-relaxed islands become embedded in a material with a smaller lattice constant which introduces considerable strain. The strain occurs mainly in the islands and not in the barrier (materials with a larger bandgap have greater stiffness), strongly affecting the band structure in the dot and the resulting confinement potential. Furthermore, the strain can induce a piezoelectric potential inside and around the dots. A detailed knowledge of the strain distribution is therefore essential for accurate modeling. A realistic calculation of the strain components in a quantum dot (including arbitrary dot shapes, varying composition, and anisotropic elastic constants) is complicated but can be carried out numerically, e.g. using finite-element methods. Strain calculations have been carried out for pure InAs dots of various shapes but very limited data is available on InGaAs dots and dots with a varying composition profile.

2.4 Electronic and optical properties

2.4.1 Disordered quantum wells

Equation (1) can be modified to include the spatially varying electron and hole potentials and effective masses in a semiconductor heterostructure:

$$\left[-\frac{\hbar^2}{2}\left(\nabla_e \frac{1}{m_e(\mathbf{r_e})}\nabla_e\right) - \frac{\hbar^2}{2}\left(\nabla_h \frac{1}{m_h(\mathbf{r_h})}\nabla_h\right) - \frac{e^2}{\epsilon|\mathbf{r}_e - \mathbf{r}_h|} + V_e(\mathbf{r}_e) + V_h(\mathbf{r}_h)\right]\Phi(\mathbf{r}_e, \mathbf{r}_h) = \mathcal{E}\Phi(\mathbf{r}_e, \mathbf{r}_h), \quad (10)$$

where the same dielectric constant has been assumed throughout the structure. Here, the case where V_e and V_h represent a quantum well potential will be considered. Fluctuations in well width due to imperfect interfaces result in a spatially varying quantization

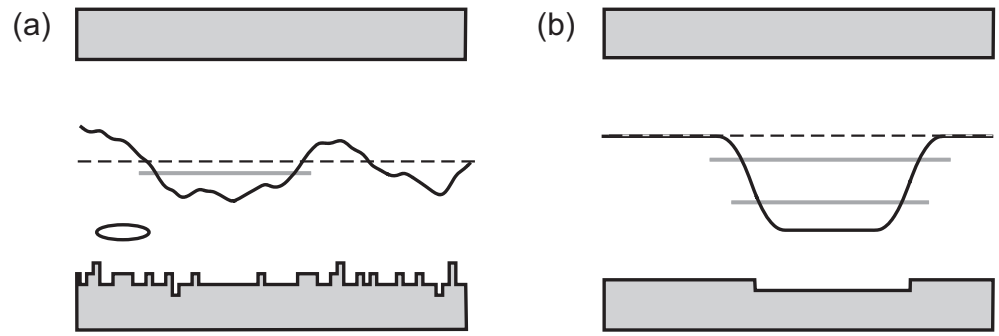

Figure 5: Averaged exciton potential for two length scales of interface roughness; (a) smaller and (b) larger than the exciton size. The gray areas represent the quantum well barriers and the in-plane exciton-averaged potential resulting from the thickness fluctuations is plotted. Dashed lines indicate the transition from localized to delocalized exciton states. Possible discrete energy states of the localized excitons are also shown.

energy for electrons and holes in the quantum well plane.[7] If potential fluctuations are small compared to the exciton binding energy, and Coulomb interactions in the growth direction are ignored, then to a good approximation the exciton envelope function is still separable into relative and center-of-mass envelope functions in the quantum well plane, and confined electron and hole envelope functions in the growth direction (z-direction) [37]:

$$\Phi(\mathbf{r}_e, \mathbf{r}_h) = \psi(\mathbf{r})\Psi(\mathbf{R})u_e(z_e)u_h(z_h), \tag{11}$$

where $\mathbf{r}$ and $\mathbf{R}$ are now understood as two-dimensional coordinates. The center-of-mass motion of the exciton obeys

$$\left[-\frac{\hbar^2}{2M}\nabla_R^2 + \widetilde{V}(\mathbf{R})\right]\Psi(\mathbf{R}) = \mathcal{E}_R\Psi(\mathbf{R}), \tag{12}$$

where the spatially varying confinement potential, $\widetilde{V}(\mathbf{R})$, is averaged separately over the relative electron and hole envelope functions. From Eq. (12), the center-of-mass eigenstates can be computed for a given random potential and used to determine the optical density of the system:

$$\alpha(\hbar\omega) \propto \sum_n M_n^2 \; \pi \; \delta(\hbar\omega - \mathcal{E}_n), \tag{13}$$

where M_n is proportional to the overlap of the electron and hole wave functions of exciton eigenstate n, and $\hbar\omega$ is the photon energy. An expression for the optical density of a one-dimensional Gaussian random potential is given in Eq. (26) in Chapter 4.

[7] Spatial variations in the exciton binding energy due to well width fluctuations also occur but are usually much smaller.

Two limiting cases of thickness fluctuations in quantum wells can be considered. The analysis sketched above covers the case where interface disorder occurs on a length scale smaller than the exciton size. This situation is shown schematically in Fig. 5a. For purposes of illustration, one interface is considered flat. The averaging over the electron and hole wavefunctions results in a smoothly varying random potential with a correlation length corresponding to the exciton size. In such a system, one expects to find a transition from a localized regime to a delocalized regime at the average value of the fluctuating potential (the percolation limit). In quantum wells, this limit has been referred to as the "effective mobility edge," defining the energy above which the two-dimensional excitons can be considered as delocalized (within their recombination lifetime) in the quantum well plane. A continuum of states exists above the mobility edge while a tail of discrete energy states is found below the mobility edge. The other limiting case involves a length scale of interface fluctuations which exceeds the size of the exciton (Fig. 5b), e.g. in a growth-interrupted quantum well. Here, the averaging of the potential becomes less important and, consequently, the potential fluctuations directly reflect the interface structure. The amplitude of the potential fluctuations (per monolayer) also increases. A finite quantization energy associated with in-plane localization is observed when the lateral size of a potential dip is sufficiently small, while still large enough to have a bound state. In the simple case shown here, the transition from localized to delocalized excitons coincides with the top of the confinement potential. This type of quantum well potential can, to a first approximation, be modeled as a collection of two-dimensional box-like quantum dots with low barrier height, corresponding to a monolayer thickness difference of the quantum well.

Following first observations in 1994 [38, 39, 40], *individually* localized excitons in quantum wells have been investigated in detail using linear and non-linear spectroscopic techniques with a high spatial resolution, both in the coherent and incoherent regime (see, e.g., Refs. [30, 41, 42, 43, 44]). Recently, microscopic imaging techniques (250 nm resolution) were applied to determine the origin of photoluminescence from a narrow (2.8 nm) $GaAs/Al_{0.3}Ga_{0.7}As$ growth-interrupted quantum well at low temperature [45]. The results indicated that all excitons contributing to the photoluminescence spectrum are spatially localized in potential minima, having a typical lateral size of 40–50 nm. The individual localized excitons share a common absorption line which was attributed to the delocalized exciton state. Larger (μm-sized) growth islands were also identified, differing in effective thickness by one monolayer. These observations are consistent with two distinct length scales of interface roughness; presumably arising from large growth islands formed on the GaAs surface and a shorter-scale interface roughness on the $Al_{0.3}Ga_{0.7}As$ surface.

2.4.2 Self-assembled quantum dots

Understanding the electronic structure of self-assembled quantum dots is substantially more difficult than for most other quantum dot systems, for several reasons: (i) The

dot and the barrier consist of different materials which can be partially intermixed, (ii) the dots have a complicated shape with a low degree of symmetry, and (iii) the dot material has a complex strain distribution, which affects the band structure and induces piezoelectric fields. Furthermore, the large variations in bandstructure on a small length scale mean that the effective mass approximation is no longer valid. In order to provide a proper description, more elaborate models are used, e.g. based on 8-band $\mathbf{k} \cdot \mathbf{p}$ theory or atomic pseudopotential methods.[8] The majority of model calculations available in the literature assumes one type of material for the dots and another for the barrier (usually InAs and GaAs, respectively) with sharply defined interfaces. Only recently, simulations of realistic dots have been reported, with geometry and chemical composition obtained from experiments [35]. Generally, however, the agreement between different models is not particularly good, due to their complexity and the number of physical parameters required, some of which have not been accurately measured.

When large ensembles of dots are studied experimentally, the *inhomogeneous broadening* of the system often masks the detailed electronic structure. Each dot has a different confinement potential, due to variations in dot size, shape and composition, resulting in a distribution of ground state energies and differences in the structure of excited states. Nevertheless, the experimentally determined level structure of strongly confined self-assembled quantum dots often looks surprisingly simple, with equally spaced and increasingly degenerate energy levels. Experimental results have therefore often been explained using an effective mass approximation and simplified geometries, e.g. describing the quantum dot as a hard-walled sphere, three-dimensional box, or as a harmonic-oscillator potential in two or three dimensions. In some cases, first-order strain effects are included by uniformly shifting the conduction and valence bands within the dots and replacing effective masses with their strained values. Although such models are far from providing a realistic picture, they provide rough estimates of energy level positions and sometimes yield valuable insight into the energy level structure.

The geometry of the $In_{0.5}Ga_{0.5}As$ dots in Fig. 4 can be used as a starting point for a simple model of the electronic structure. The thickness of the wetting layer can be estimated from the deposited thickness, after subtracting the volume of the dots. For a dot density of $\approx 1 \times 10^{10}\,\mathrm{cm}^{-2}$, determined from the figure, a wetting layer thickness of 3 ML is obtained. A realistic chemical composition profile of the (nominally $In_{0.5}Ga_{0.5}As$) three-monolayer thick quantum well is determined using a segregation model, because of the strong tendency of indium to "float" on the growth surface. Microscopically, when the InGaAs layer is overgrown with a single monolayer of GaAs, an indium atom may switch sites with a gallium atom on the surface. The fraction of indium segregating to the next monolayer can be calculated from the relevant energy balance and the growth temperature, using the law of mass action. This segregation model has been used to accurately predict transition energies in InAlGaAs quantum wells as described in more detail in Refs. [46, 47]. Using the resulting chemical profile, the band structure and the

[8] For a detailed description of these methods, see Ref. [24].

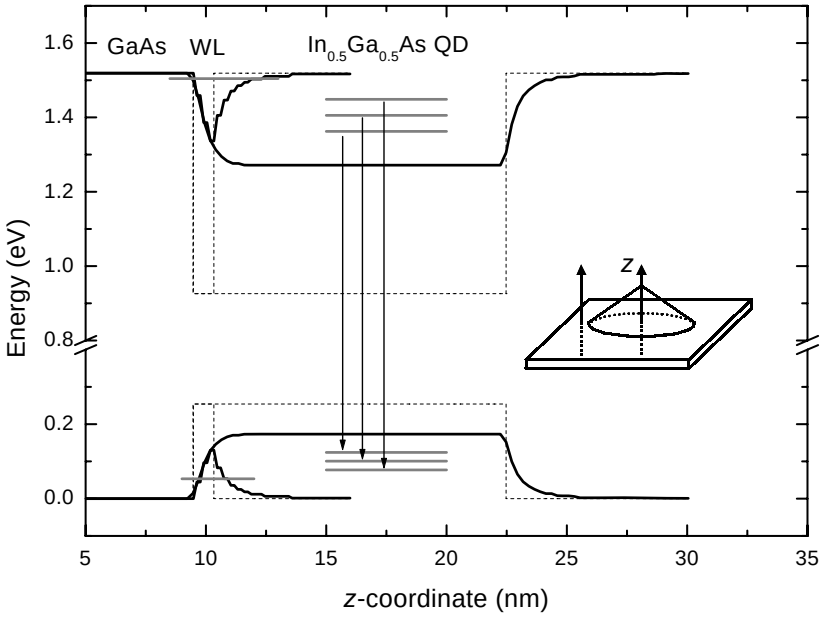

Figure 6: Calculated energy levels of a conical $In_{0.5}Ga_{0.5}As$ quantum dot, using parameters described in the text. Solid lines represent strained band edge potentials, including segregation effects, for cuts through the wetting layer and through the center of the dot, respectively. The dashed lines indicate the nominal unstrained band profile. Gray lines indicate the energy level positions in the dot and the wetting layer. The strongest optically active interband transitions in the dot are shown with vertical arrows.

effective masses can be calculated, including the effect of the biaxial strain in the well. The results are shown in Fig. 6. A similar calculation was made for a quantum well with a thickness corresponding to a typical quantum dot height. For comparison, the unstrained, nominal quantum well potentials are shown with dashed lines in the figure, illustrating the importance of including strain and segregation effects. Ground-state electron and heavy-hole energies for the wetting layer were calculated in a one-dimensional model, assuming an isotropic conduction band and using a 6-band $\mathbf{k} \cdot \mathbf{p}$ Hamiltonian for the valence band [48]. Subtracting an exciton binding energy given by the bulk value for GaAs (thin quantum well limit) gives a predicted wetting layer transition energy of 1.447 eV. For these calculations, a 30% valence band offset ($\Delta E_v / \Delta E_g$) between GaAs and InGaAs was used. It should be noted, however, that the actual band lineup of the two materials is not well known, and values ranging from 5% to 35% have been used for calculations in previous literature.

As a first approximation, the strain in the quantum dot can be taken as homogeneous and equal to that of the quantum well. This is partially justified by the relatively small lattice mismatch and flat shape of the dots, as compared to InAs quantum dots. The strained band-edge values and effective masses for an $In_{0.5}Ga_{0.5}As$ quantum well were used as input parameters for a conical quantum dot model [49]. A dot height of 12 nm and base diameter of 44 nm were assumed for the calculation, corresponding to typical dots shown in Fig. 4. The positions of the three lowest electron and heavy-hole states are shown in Fig. 6. The ground-state transition energy equals 1.238 eV (not including the Coulomb correction). The dot size distribution shown in Fig. 4 leads to an inhomogeneous broadening of the ground state transition of approximately 55 meV (FWHM).

When the electron and hole wavefunctions corresponding to each state are orthonormal (as would be the case for, e.g., a box-shaped or spherical dot with infinite potential barriers and no Coulomb interaction), interband transitions between states with different quantum number are not allowed. For real dots, the wavefunctions are no longer orthonormal and these "forbidden transitions" become weakly allowed. The main contribution to the optical response, however, results from the transitions shown in Fig. 6. A 67-meV splitting of the ground state (e1-hh1) and the first excited state (e2-hh2) is predicted by the calculation. The Coulomb interaction between the electron and hole shifts the energy levels by an amount that depends on the detailed shape of the electron and hole wavefunctions. For the envelope functions calculated here, a binding energy of 14 meV is predicted [50]. These simplified calculations are compared with experiments in Chapter 5.

3 Experimental Techniques

This chapter describes the experimental techniques that were used to fabricate and characterize the samples investigated in this thesis. Growth and processing of samples was carried out at III–V Nanolab, a laboratory run jointly by Research Center COM and the University of Copenhagen. The growth techniques will not be discussed in detail, since comprehensive accounts have previously been given by J.R. Jensen [47] and C.B. Sørensen [51], who also are responsible for growing the wafers used here. A brief description of growth conditions and sample structure is given in Sec. 3.1.1. Electron-beam lithography and related processing of samples used for single-quantum-dot spectroscopy are addressed in Sec. 3.1.2. Standard characterization methods such as photoluminescence (PL) and photoluminescence excitation (PLE) spectroscopy will not be covered — the reader is referred to readily available texts on the subject, e.g. Ref. [52]. However, a description of equipment specifically constructed for reaching high spatial and spectral resolution will be given in Sections 3.2.1 and 3.2.2, respectively. Finally, in Sec. 3.3, techniques employed for measurements of exciton coherence will be outlined.

3.1 Sample growth and processing

3.1.1 Molecular-beam epitaxy

Samples were grown by molecular-beam epitaxy in a Varian Modular GEN II reactor on 2-inch undoped GaAs wafers. After degassing at 400°C, substrate wafers are mounted on a holder in the growth chamber, facing a circular arrangement of eight elemental sources (Fig. 7). The sources are heated and carefully temperature-regulated to maintain a constant flux of atoms or molecules from each source. Growth of heterostructures is achieved by using computer-controlled mechanical shutters to turn the individual atomic beams on and off. The sources contain pure Ga, As, In, and Al, as well as Si and Be for n and p-type doping, respectively. All samples used in the present work were grown without doping but nominally undoped GaAs grown in the MBE machine is weakly n-type, with a carrier density of 10^{14}–$10^{15}\,\mathrm{cm}^{-3}$, due to impurities and native defects. During growth on the (001) surface, the As source remains open and the growth is controlled by the flux of group-III materials only, operating with a V/III flux ratio of approximately 8–10. Typical growth rates used here were around 0.8 ML/s for GaAs and 0.3 ML/s for AlAs, with the substrate maintained at a temperature around 630°C. Growth rates

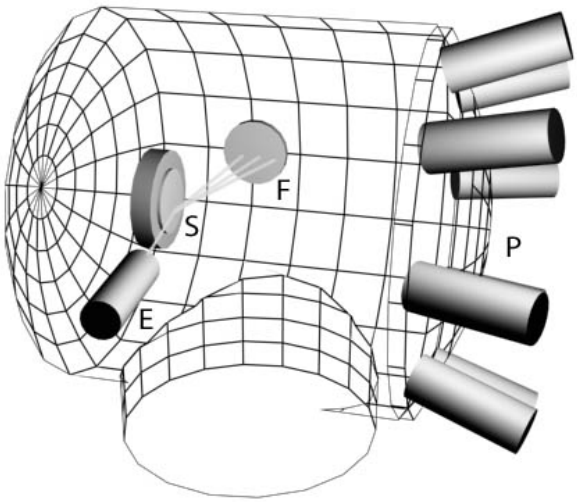

Figure 7: Geometry of the MBE growth chamber, showing the substrate holder (S), panel of elemental sources (P), electron gun (E) and fluorescent screen (F).

and substrate temperatures were modified when growing indium-containing material, as discussed below.

Growth rates were calibrated using reflection high energy electron diffraction (RHEED) on a reference wafer prior to mounting the sample wafer on the substrate holder. The RHEED calibration involves monitoring the diffraction pattern of a beam of 15-keV electrons incident at a grazing angle to the substrate. The diffraction pattern is imaged on a fluorescent screen and the fluorescence intensity at a particular spot can be monitored with a photodetector. During growth, oscillations appear in the diffracted signal as the surface structure changes. The period of the RHEED oscillation corresponds to the time required to grow a single monolayer of material. Due to the fact that the sources are mounted at an angle to the substrate normal, a variation is expected in the amount of material reaching different parts of the wafer. For the particular geometry of the growth chamber, a variation of 5%/cm has been estimated [47], which amounts to a 20–25% variation in the rate of deposition across the usable area of the wafer. Furthermore, the direction of the thickness gradient varies for different materials. The substrate can be rotated during growth in order to obtain a more uniform deposition. However, the variation in growth rate across the wafer can also be used advantageously to obtain a continuously varying thickness and (in the case of ternary and quaternary alloys) composition of deposited layers on a single wafer.

For the study of exciton localization in disordered quantum wells (Chapter 4) four wafers were grown, each containing three GaAs quantum wells, nominally 10 nm, 7 nm, and 5 nm wide. Pure AlAs was used for the barriers. The use of binary barrier and well materials eliminates effects of alloy disorder and variations in alloy composition across

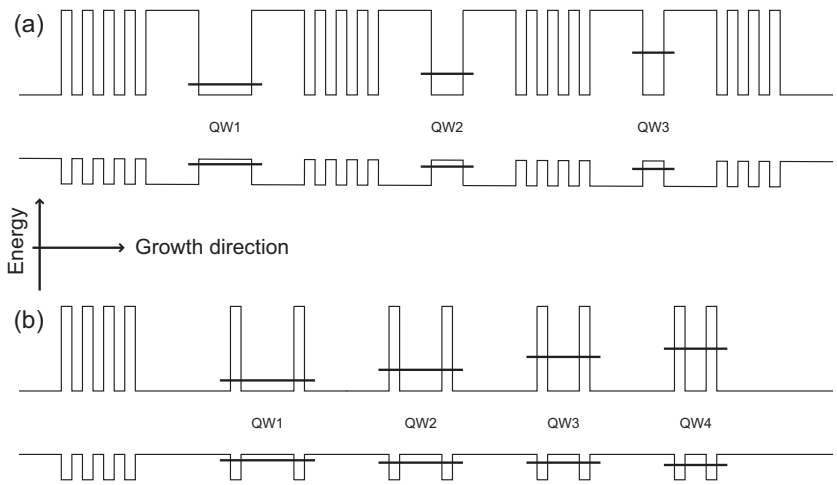

Figure 8: Schematic band structure of wafers fabricated with growth interruption on both sides of the quantum wells. The lower structure is designed to minimize charging (trion formation) in the quantum wells.

the wafer. One of the wafers was grown continuously, without any growth interruption. A second wafer was grown with a 120-s growth interruption *before* growing each well, while for the third wafer, growth was interrupted for 120 s *after* growing the wells. The fourth wafer was fabricated with a growth interruption both before and after growing the wells. GaAs/AlAs short-period superlattices were grown between wells in order to trap impurities and to improve the surface structure. Rotation of the substrate was stopped only during the growth of the wells in order to achieve a continuous variation in well width across the wafer while maintaining a constant barrier thickness. The bandstructure for the sample is shown schematically in Fig. 8a. In a later run, a wafer with four GaAs quantum wells, growth-interrupted at both interfaces, was fabricated under similar growth conditions. The nominal quantum well widths were 11 nm, 8.5 nm, 6.5 nm and 5 nm. Narrow (8 nm) AlAs barriers and 50 nm GaAs spacers were grown between the wells, as illustrated in Fig. 8b. This particular structure was designed to reduce the probability of forming charged excitons in the quantum wells.

Strain-induced self-assembled quantum dots (Chapter 5) were grown by incorporating indium into the structure. Pure InAs grown on GaAs forms strain-relaxed islands already at < 2 ML of coverage, making a straightforward growth calibration of pure InAs by RHEED impossible on a GaAs substrate. The RHEED pattern, however, clearly reflects the transformation from 2-D layer growth to island growth, as shown in Fig. 9. This can be used as an *in-situ* indication of quantum dot formation, provided that the wafer is not rotated during the growth of the dots. The growth rate of InAs is calibrated by comparing the GaAs growth rate with that of $In_xGa_{1-x}As$, where $x \approx 0.15$. In this case, thick layers can be grown without strain relaxation because of the relatively small lattice mismatch of about 1%. Typically, InAs growth rates of approximately 0.15 ML/s were

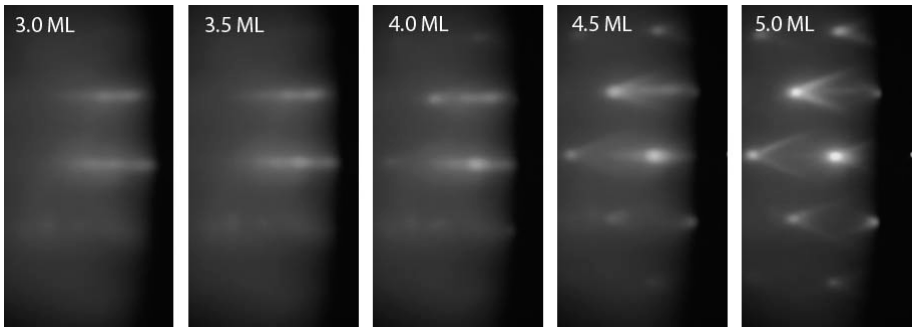

Figure 9: RHEED patterns after successive half-monolayer deposition cycles of $In_{0.5}Ga_{0.5}As$ on GaAs showing a distinct change in the electron diffraction pattern from lines to spots due to a strain-induced restructuring of the grown layer.

used. Furthermore, in order to increase the sticking probability of indium on the surface, the substrate temperature was lowered to 470–500°C during growth of indium-containing material. In all quantum dot samples, thin AlAs layers were placed 20 nm above and 100 nm below the dot layer to prevent diffusion of optically excited carriers to the surface and substrate. After capping with GaAs, the dots are buried approximately 50 nm below the sample surface.

$In_{0.5}Ga_{0.5}As$ quantum dots were grown by reducing the Ga source temperature to match the InAs growth rate and depositing single or half monolayers of $In_{0.5}Ga_{0.5}As$ at a time, interrupting growth for several seconds between cycles. A 20-nm layer of GaAs was deposited before growing the dots, using the reduced growth rate and lower substrate temperature, to avoid stopping growth at the dot layer while waiting for the source and substrate temperatures to stabilize. The cap layer was also grown without interruption under the same conditions. After depositing 4.5–5 ML of $In_{0.5}Ga_{0.5}As$, the layer relaxed to an island structure, in agreement with published data on the layer-to-island transition [53, 54]. AFM investigations on similarly prepared and uncapped dots were presented in Sec. 2.3.2. $In_{0.5}Ga_{0.5}As$ dots were also grown embedded in $Al_{0.35}Ga_{0.65}As$ barriers. The same critical layer thickness for dot formation was observed in this case.

Quaternary $In_xAl_yGa_{1-x-y}As$ dots were grown using a sub-monolayer deposition technique, i.e. by alternately depositing 0.5-ML thick layers of InAs and AlGaAs. Here, the deposited thickness was controlled by adjusting the shutter times rather than by changing the AlGaAs growth rate. Growth was interrupted for several seconds after completing each monolayer. A net indium molefraction of $x = 0.5$ was used to ensure the same lattice mismatch as for $In_{0.5}Ga_{0.5}As$ dots. The fraction of aluminum was $y = 0.04$–0.05. The same relative Al-to-Ga concentration was used in the dots and the barriers to avoid changing the temperature of the sources,[9] giving $Al_{2y}Ga_{1-2y}As$ barriers for $x = 0.5$. Islands were

[9] At the time of growth, only one Al source was available in the MBE. Since then, a second Al source has been added, increasing the flexibility of the system.

formed after depositing 6 ML of InAlGaAs, consistent with reported observations that the presence of aluminum in the dot material slows down the layer-to-island transformation [55]. A ten-layer sample of $In_{0.5}Al_{0.05}Ga_{0.45}As$ quantum dots was also grown, using 50-nm spacer layers of $Al_{0.1}Ga_{0.9}As$ between the dot layers. This spacer layer thickness is sufficient to avoid vertical coupling and strain-induced stacking of dots [56].

3.1.2 Electron-beam lithography

The areal density of self-assembled quantum dots normally lies in the range 10^{10}–$10^{11}\,\mathrm{cm}^{-2}$. The distance between dots, therefore, is of the order of 100 nm or below. Exciton localization in growth-interrupted quantum wells also occurs on similar length scales. The spatial resolution of standard far-field optics is ultimately limited by the wavelength of the detected light (see Sec. 3.2.1) and is typically insufficient to resolve emission from individual dots. In order to get around this limit, the detection area can be reduced by masking or removing an area of the sample, leaving only sub-wavelength-sized regions for inspection. In order to allow for optical investigation of few quantum dots in the present work, MBE-grown samples were patterned using electron-beam lithography.

Electron-beam lithography (EBL) is used mainly to fabricate masks for standard optical lithography, for prototyping and small-scale fabrication of advanced electronic and photonic integrated circuits, and for research in mesoscopic physics and quantum phenomena. The EBL technique is described in detail in Ref. [57]. The lithography system used here is a modified field-emission scanning electron microscope (JEOL JSM-6320F). An external processor unit (Raith GmbH) controls the scanning of the electron beam. A separate beam blanker is also used to rapidly switch the electron beam on and off. The system is controlled by a desktop computer, which translates predefined mask files (GDSII standard) into exposure instructions. Electron beam lithography is carried out by coating a sample surface with a thin layer of *resist*, typically polymethyl methacrylate (PMMA), and scanning selected areas with the electron beam. When PMMA is exposed to the electron beam, its polymer chains are broken into fragments that are easily dissolved in a developer solution. The resist pattern can be transferred to the sample, e.g. by a *lift-off* process, where a layer of metal is deposited on the surface and the remaining unexposed resist is subsequently removed, leaving a metal coating only in those areas where the resist was exposed. Pattern transfer can also be achieved by etching the sample in areas not protected by resist. These two methods can also be combined, e.g. when a high etch resistance of the cover layer is required, by using the patterned metal layer as an etch mask. Different types of electron-beam resist exists, having different sensitivity, contrast and resolution. *Negative resist* is also available, where electron-beam exposure induces a cross-linking of polymer chains, making the exposed resist *less* soluble in developer. In practice, the resolution of the EBL process is defined by the type and thickness of resist, as well as the method of pattern transfer, rather than by the resolution of the electron microscope itself. Furthermore, although the electron beam can be focused down to a

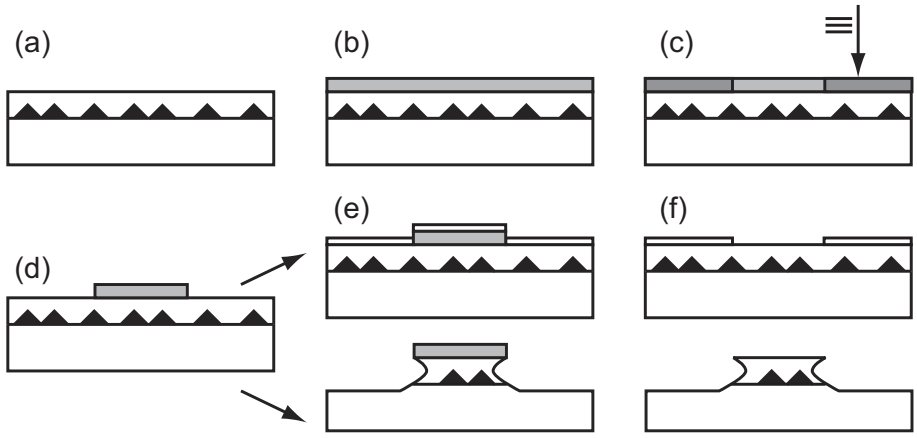

Figure 10: Processing steps used in preparing samples for single-quantum-dot spectroscopy.

10-nm spot, a larger area is partially exposed by electrons that are backscattered from the sample (*proximity effect*). This has to be taken into account when designing masks with small features.

Negative resist is a convenient choice when larger regions of the sample are to be etched or coated with metal, leaving smaller areas unaffected. Experiments were made using a standard high-resolution negative resist, SAL-601 (Shipley Inc.). The adhesion of SAL to GaAs was found to be poor and small features were prone to gliding around on the sample surface during developing. The exposure mask was therefore inverted and a positive resist used instead. This involved exposing a large part of the writing field (typically 130 μm $\times$ 130 μm). Exposure time was decreased considerably without sacrificing resolution by using a sensitive ZEP-520 resist (Nippon Zeon Co.) instead of the standard PMMA. With ZEP resist, the entire writefield can be exposed in a few minutes with a beam current of about 40 pA, using a typical exposure of 20 μC/cm^2. The charge per area is adjusted by varying the beam dwell time as it is scanned across the surface.

Figure 10 shows the process steps used in preparing samples for optical investigations. (a) The sample contains a layer of quantum dots close to the surface. The surface is cleaned using acetone, methanol and isopropanol, in that order, and blown dry with nitrogen. (b) The sample is coated with ZEP-520 by spinning at 2000–6000 rpm. The resist thickness can be varied from 500 nm to 300 nm by changing the spin speed. ZEP can also be diluted in anisole to obtain a thinner resist layer. A 1:1 mixture gives a resist thickness in the range 100–200 nm. Solvent is removed from the resist after spinning by heating the sample to 185°C for 3 minutes on a hotplate. (c) The sample is loaded into the SEM and areas to be exposed are scanned with the electron beam. (d) The sample is removed from the SEM and immersed in ZED N-50 developer (n-amyl acetate) for 30 s. Immediately afterwards, the sample is dipped into a ZMD-B rinse solution (89% methyl isobutyl ketone,

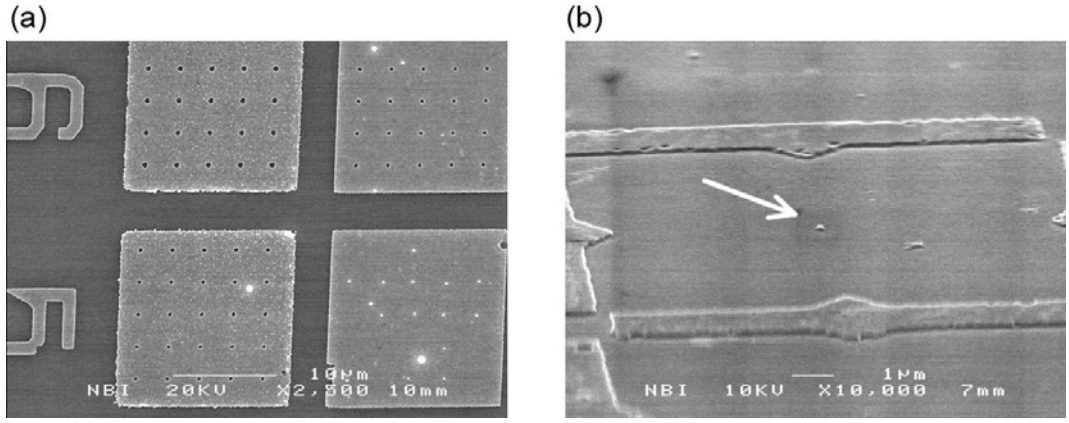

Figure 11: Examples of samples processed by electron-beam lithography. (a) Apertures in 75-nm gold film. Each row of metal pads has a different nominal aperature size (decreasing from top to bottom) and each column has a different exposure dose (increasing from left to right). Larger doses give smaller apertures, as a result of the proximity effect. (b) Etched 200-nm mesa. The features surrounding the mesa serve as markers.

11% isopropyl alcohol) to clean off the remaining developer. (e) Two methods are used to optically isolate the unexposed areas. Samples are coated with a thin layer of gold or silver, or wet-etched through the quantum-dot layer using a H_3PO_4:H_2O_2:H_2O (1:1:38) mixture, which etches GaAs isotropically at a rate of 100 nm/min. (f) Finally, the remaining resist is stripped off using NMP (n-methyl-2-pyrrolidone). In some cases, Al layers were used as an etch mask and removed afterwards by etching in KOH for 60 s.

As mentioned above, the smallest feature size obtained with EBL depends on several factors. For the process described here, the lateral resolution of the developed resist pattern is similar to the resist thickness. When samples were coated with metal, a resist layer with 2–3 times the thickness of the metal layer was used, in order to ensure proper lift-off. Given that the metal must be sufficiently thick to block incident radiation and/or emitted luminescence, this puts a limit on the obtainable aperture size. Using a resist thickness of 300 nm, apertures with sizes down to 200–300 nm were reproducibly fabricated in a 75-nm gold film using the process steps described above (Fig. 11a). The shape of the apertures is slightly irregular due to a grain structure in the deposited film. In the case of etched structures (Fig. 11b) there is no lower limit on the mesa size since the mesa is also etched laterally from the sides.

GaAs has a high density of surface states around the middle of the bandgap which induces an electric field and bends the energy bands close to the surface. The surface potential ($eV_S = 0.63$ eV for GaAs(001)) is unaffected by the presence of the dots if the cover layer is more than a few ML thick [58]. Coating GaAs with metal only has a small effect on the band bending and the metal-semiconductor contact potential (Schottky barrier) is determined primarily by the surface states rather than the type of metal used

[59]. Schottky barriers around 0.8 eV have been measured for gold on insulating GaAs(001) [60]. Gauss's law can be applied to calculate the built-in electric field extending a distance w into the semiconductor from a flat surface:

$$E_z(z < w) = -\frac{eN_d}{\epsilon}(w - z), \tag{14}$$

assuming a uniform donor concentration, N_d, in the material. The electric field sweeps free carriers out of the region $0 < z < w$, referred to as the *depletion region*, leaving the donors ionized. Eq. (14) can be integrated to obtain a relation between the surface potential and the width of the depletion region

$$w = \sqrt{\frac{2\epsilon V_S}{eN_d}}, \tag{15}$$

which is close to $1\,\mu$m for $N_d = 10^{15}\,\mathrm{cm}^{-3}$. Quantum dot layers close to the surface therefore experience an electric field of the order of $10\,\mathrm{kV/cm}$ in the growth direction, irrespective of whether the surface is coated with metal or not. In etched mesa structures, however, new surfaces with different surface state densities are formed and the built-in electric-field pattern inside the mesa becomes more complicated.

3.2 Photoluminescence characterization

3.2.1 Micro-photoluminescence apparatus

Recent years have seen a large increase in the application of local-probe spectroscopy for investigating semiconductor nanostructures. A comprehensive review of various local-probe techniques can be found in Ref. [41]. The most common methods involve excitation and/or detection through a microscope objective (micro-PL) or through a tapered optical fiber placed very close to the surface (scanning near-field optical microscopy). Less common techniques include far-field detection of luminescence which is locally excited by a focused electron beam (cathodoluminescence) or through the tip of a scanning tunneling microscope (scanning tunneling luminescence). In many cases, semiconductor materials are investigated at low temperatures (typically 4–10 K) and combining a high-spatial-resolution detection system with cryogenic cooling apparatus can be a challenging task.

In far-field optics, the diffraction limit for resolving two point sources, separated by a distance D, is given by

$$D \approx \frac{1.2\lambda}{2n\sin\theta}, \tag{16}$$

where λ is the wavelength of the emitted light and $n\sin\theta$ is the numerical aperture (NA) of the detection system (n is the refractive index of the material between the sample and the lens and 2θ is the angle subtended by the lens). The resolution of a detection system therefore increases linearly with its NA. A large numerical aperture also improves the light

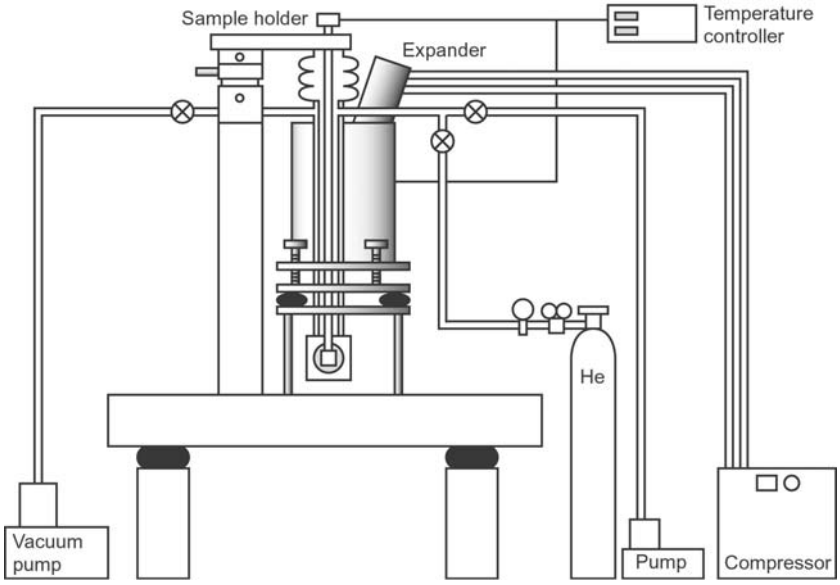

Figure 12: Cryogenic cooling system used for optical investigations.

collection efficiency, which is proportional to the square of NA. In practice, Eq. (16) limits the resolution to about 0.7λ for a sample in air. This can be improved by introducing immersion oil between the sample and the objective, increasing n to about 1.5. This technique, however, is not applicable at cryogenic temperatures. Instead, so-called solid immersion lenses (typically small high-n hemispheres in contact with the sample) have been used to increase the NA. This technique has been used for spatially resolved PL imaging with a resolution of 0.33λ [45]. Eq. (16) can also be taken as a measure of the minimum (diffraction-limited) spot size of a focused laser beam. A small area of the sample can therefore be simultaneously excited and detected through the same objective lens (*confocal microscopy*). In some cases, scanning confocal microscopy can be used to improve the spatial resolution beyond the diffraction limit [41]. This is rarely possible in semiconductors, however, where significant drift and diffusion of excited electrons and holes typically takes place before they recombine and emit radiation.

As a part of the present project, a micro-photoluminescence system was constructed and used in conjunction with the previously described EBL patterning. Spectroscopy beyond the diffraction limit is possible in this case, but only on areas predefined in the lithographic process. This is in many cases practical, however, since it is possible to reproducibly measure *exactly* the same spot on the sample. A closed-cycle He cryostat (APD Cryogenics) was also set up for using with the micro-PL apparatus. Micro-PL systems used for low-temperature investigations are usually constructed with optics external to the cryostat, with the main advantage that focusing and scanning of the sample surface can be carried out by moving the external optics and the cryostat with respect to each other. This allows for a simple construction with a large translation range, so that

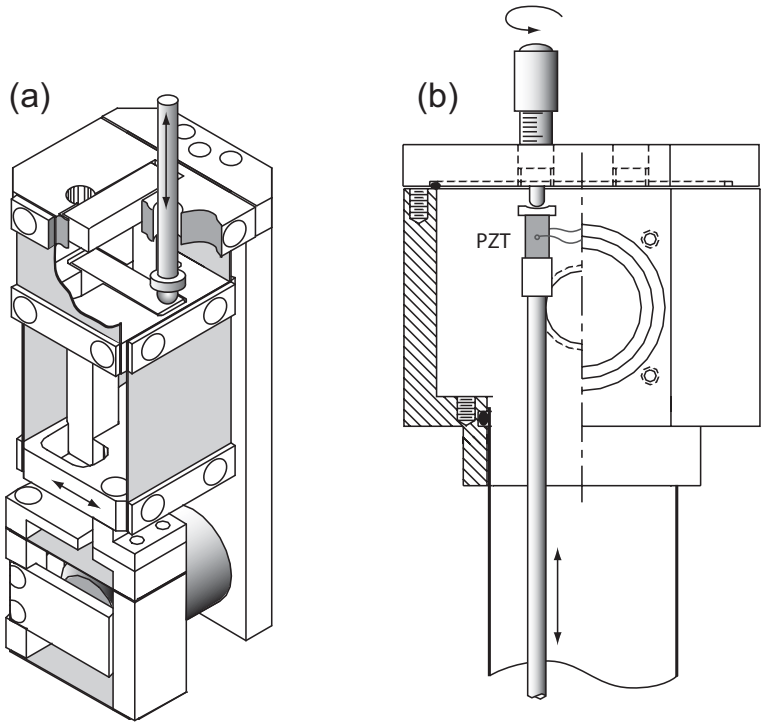

Figure 13: Sample holder for micro-photoluminescence measurements.

several samples can be mounted, cooled, and measured simultaneously. Typically, small "pancake"-type liquid-He continuous-flow cryostats are used for this purpose, since they are compact and largely free of mechanical vibrations. A disadvantage of this configuration is that the sample and the microscope objective are placed several millimeters apart, separated by the cryostat window. This limits the resolution and collection efficiency unless aberration-corrected long-working-distance optics are employed. Furthermore, a supply of liquid He is required. The micro-PL system used here, however, was placed *inside* the closed-cycle cryostat. This involves cooling the microscope objective and the mechanism for focusing and translating the sample. Fig. 12 shows the construction of the cryogenic system. A special feature of this system is that the sample holder is vibration-isolated from the cryostat with rubber bellows and attached directly to the optical table. Furthermore, the sample well of the cryostat has a relatively large diameter of about 40 mm. During cooling, the well is filled with He gas at a slight overpressure (≈ 10 mbar). A membrane pump is used to purge the sample well of atmospheric gases prior to cooling. The cryostat itself is mounted on viscoelastic damping pads (Sorbothane Inc.) to reduce the amount of vibration carried to the optical table. The sample well is surrounded by a vacuum shroud for thermal isolation. An oil-free pump station (Varian), consisting of a turbomolecular pump and a membrane backing pump, maintains a base pressure of around 2×10^{-4} mbar. With a sample holder in place, the system can reach a minimum temperature of 9–11 K.

The sample holder constructed for micro-PL investigations (Fig. 13) fits into the sample well of the cryostat. Three dimensional movement of the sample is achieved using a system of rods, levers and flexible steel plates (Fig. 13a). Sample movement is controlled through the top housing (Fig. 13b), using micrometer screws and piezoelectric actuators. The microscope objective contains the lens configuration of a standard DIN 60× objective (Edmund Scientific), with an NA of 0.85 and a working distance of 0.3 mm. The sample holder is not in direct contact with the cryostat and no vibration of the sample relative to the lens is observed on a micrometer scale. Furthermore, the mechanical and thermal stability of the system is sufficient for a laser spot to stay centered on a sub-micron sized aperture for at least 24 hours, with the compressor/expander unit running. The sample holder, including the top housing, forms a part of the sample well and is therefore vacuum-tight to prevent leaks of atmospheric gases into the well. Electrical feedthroughs are provided for the piezoelectric crystals as well as for a temperature sensor and resistive heater (not shown in the figure). The sample temperature is more conveniently controlled, however, by heating the He gas in the sample well directly, using a built-in heater circuit in the cryostat. This ensures that the sample, objective, and surrounding gas have the same equilibrium temperature.

The micro-PL system has been used for studying various low-dimensional semiconductor systems. Fig. 14a shows a line scan across a thin (2.4 nm) GaAs quantum well grown on a GaAs(110) surface [61]. Strong exciton localization is observed, evidenced by the spatially varying pattern of sharp PL peaks. A cut through one of these peaks, shown on the left, confirms that the spatial resolution is 0.5 μm as predicted by Eq. (16). A similar line scan across a series of quantum wires, formed by cleaved-edge overgrowth [47, 61], is shown in Fig. 14b. The spatial origin of signals from the single overgrown quantum well (SQW), the multiple quantum wells (MQW), and the quantum wires (QWR), can be clearly identified. The total width of the MQW region in this case was 2.5 μm. Fig. 14c shows micro-PL images of a patterned GaAs surface overgrown with a quantum well structure (cf. Fig. 2b).[10] The local thickness of the quantum well is increased at the bottom and the edges of the triangular pyramid-shaped holes, resulting in dot-like states (at energy E_1) and wire-like states (at energy E_2) [62]. Luminescence from the two sets of states is separated using different band-pass filters and the filtered PL is imaged directly onto a silicon charge-coupled device (CCD) chip. Apart from the work presented in this thesis, the micro-PL system was also used for investigating localized excitons in CdSe/ZnSe quantum dots [63].

3.2.2 High-resolution spectrometer

Three-dimensional localization of excitons results in a discrete density of states and narrow transition lines (Fig. 1). Commonly, the narrow transition linewidth is masked by a much larger inhomogeneous broadening, e.g. in disordered quantum wells and quantum dots

[10] Samples courtesy of H. Matsueda

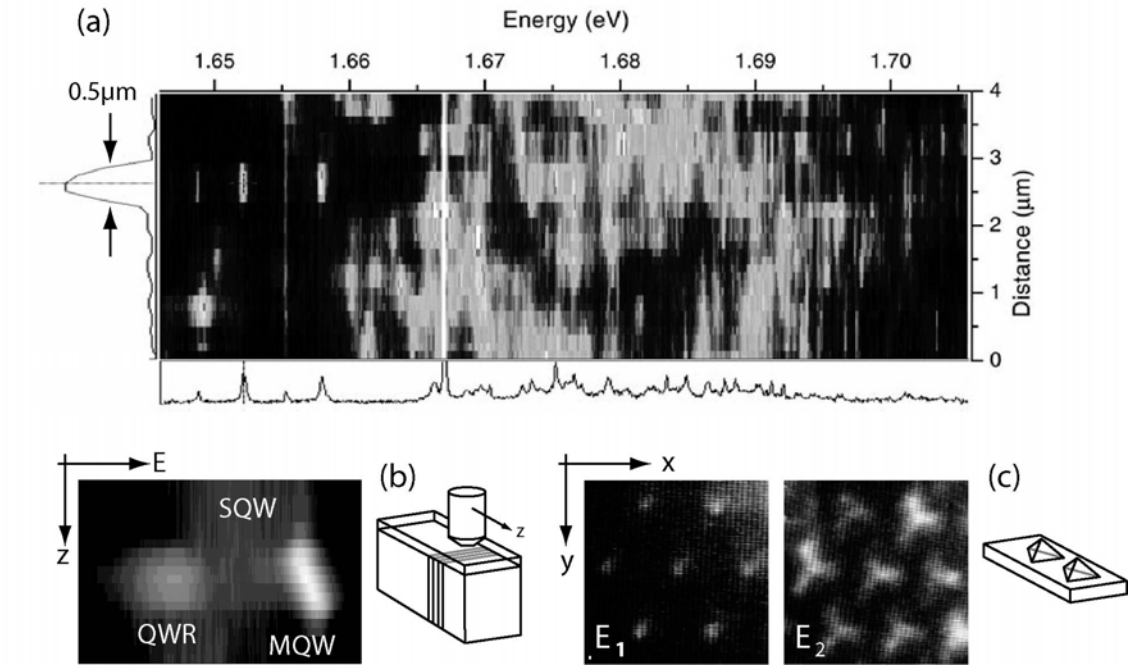

Figure 14: Examples of micro-photoluminescence measurements. (a) Localized excitons in a thin quantum well. The cross section on the left demonstrates the spatial resolution of the system. (b) Line scan across a set of T-shaped quantum wires (QWR) formed at the intersection between a single quantum well (SQW) and multiple quantum wells (MQW). (c) PL image of an array of quantum dots in etched pyramid-shaped holes, emitting at energy E_1. The imaging confirms that luminescence emitted at a different energy E_2 arises from quantum wires running along the sides of the pyramids.

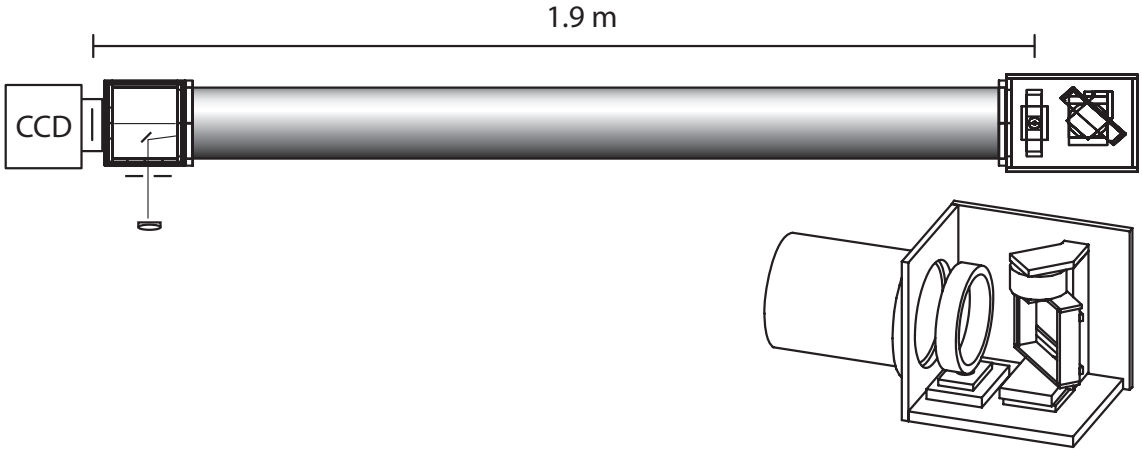

Figure 15: High-resolution spectrometer. The grating and lens assembly is enlarged.

with size fluctuations. High spatial resolution, however, allows optical probing of individually localized excitons within the inhomogeneously broadened ensemble. A spectrometer with a high spectral resolution was therefore constructed to complement the micro-PL apparatus described above. The spectrometer design is based on the Littrow configuration [64], which allows for simultaneous imaging of the input slit and the PL spectrum at the spectrometer output. Spectrally and spatially (1-D) resolved photoluminescence spectra can therefore be directly obtained by detecting with a CCD array.

The layout of the spectrometer is shown in Fig. 15. The sample surface is imaged in the plane of the input slit. The light passing through the slit is collimated by a 128-mm diameter, f=1900-mm focal length achromatic lens, placed at the other end of the spectrometer. The collimated light is incident on a 128-mm wide holographic grating with 1500 lines/mm. The angle of the grating is adjusted so that the first diffraction order passes back through the lens which focuses it onto a CCD chip (width $\times$ height = 1024 $\times$ 256 pixels, pixel size 26 μm). The grating is attached to a rotation stage for wavelength selection and the lens is mounted on a translation stage (used to correct for chromatic aberration). The relationship between the wavelength and the the angle of incidence/diffraction, Θ, can be obtained from the grating equation [64]:

$$\lambda = 2d \sin \Theta, \tag{17}$$

where d is the groove spacing. The (linear) chromatic dispersion at the CCD chip is given by

$$\frac{\Delta\lambda}{\Delta x} = \frac{d \cos \Theta}{f}. \tag{18}$$

The calculated dispersion is plotted in Fig. 16a, along with measured values. The angular position of the grating, as read off the rotation stage, is also shown for different wavelengths. The position of the rotation stage corresponds to $\Theta(\lambda) + 136°$.

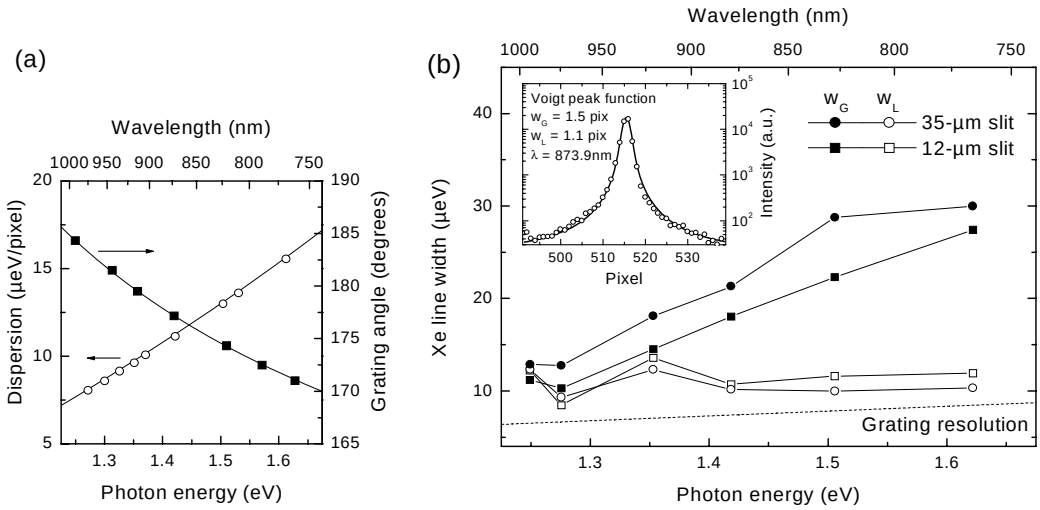

Figure 16: (a) Chromatic dispersion (open circles) and angular setting of the grating (closed squares) measured for different wavelengths. Solid lines are calculated from Equations (18) and (17), respectively. (b) Width parameters of Voigt functions fitted to atomic transition lines emitted from a low-pressure calibration lamp. The inset shows one such line, along with the fitted peak function. The dashed line indicates the resolution limit imposed by the finite size of the grating.

The resolution of the grating (in first order)[11] is given by the total number of grating lines ($\lambda/\Delta\lambda = N \approx 2 \times 10^5$) and is shown with a dashed line in Fig. 16b. The actual resolution of the spectrometer, however, is also limited by its imaging properties and the size of the detector elements. Spectral lines from a low-pressure Xe calibration lamp were used to calibrate the spectrometer and to investigate its instrumental broadening. In reality, atomic spectral lines have a complicated fine structure [65] which can result in irregular lineshapes. In can be assumed, however, that the *lower limit* of the actual linewidth is given by the Doppler broadening, which for Xe amounts to 1–2 μeV (FWHM) in the wavelength range investigated here [66]. The shape of Xe lines measured with the high-resolution spectrometer was, in most cases, well described by a Voigt peak function (inset of Fig. 16b), which is a convolution of a Lorentzian and a Gaussian lineshape. The widths of the Gaussian and Lorentzian components of the fitted peak function (w_G and w_L, respectively) are plotted for several Xe lines in Fig. 16b. The width of the Lorentzian part is close to 10 μeV and does not depend strongly on wavelength. The Gaussian width is larger, increases for shorter wavelengths and depends on the width of the input slit. It can be concluded that w_G is defined by the imaging properties of the spectrometer. At shorter wavelengths, the chromatic dispersion is higher and a given spot size corresponds to a greater spread in energy, resulting in the observed wavelength dependence. A slit width of 12 μm is below the diffraction limit of the focusing lens in the whole wavelength range shown here, and therefore represents the ultimate resolution limit of the spectrometer. The FWHM of the Voigt profile varied from 16 μeV (1.9 pixels) at 971.8 nm to 34 μeV (2.2 pixels) at 764.2 nm.

For spectrally narrow emission lines, the discretization of the spectrum by the detector elements becomes an important factor in the fitting process. In order to investigate this effect, peak functions of different width were piecewise integrated to represent the CCD pixels and subsequently fitted with the original peak functions. Fitted widths of Lorentzian peaks with $w_L = 1$–2 pixels can exceed the actual width by up to 30% depending on whether the line is centered on or between pixels. In the case of Voigt functions with $w_G \approx w_L = 1$–2 pixels, however, the fitted peaks correspond well to the originals and show $< 2\%$ variation for different positions of the line relative to the detector elements. In single-quantum-dot spectroscopy, the signal strength is often low and the full dynamic range of the CCD camera can not be used. The tails of the peak function rapidly fall below the background noise level of the detector, adding considerable uncertainty in the fitted linewidth. If the actual shape of the measured PL line is Gaussian or Lorentzian, or a convolution of the two, then the measured lineshape will be given by a Voigt function. However, fitting such a complex non-analytical function to a limited data set is difficult and unreliable. In this thesis, measured PL peaks are therefore fitted with Lorentzian or Gaussian functions. Where accurate linewidth information is required, the resulting fitting parameters are corrected numerically, based on similar fits to calculated Voigt profiles obtained through a convolution of hypothetical PL line shapes and the spectrometer response.

[11] Often called *resolving power*.

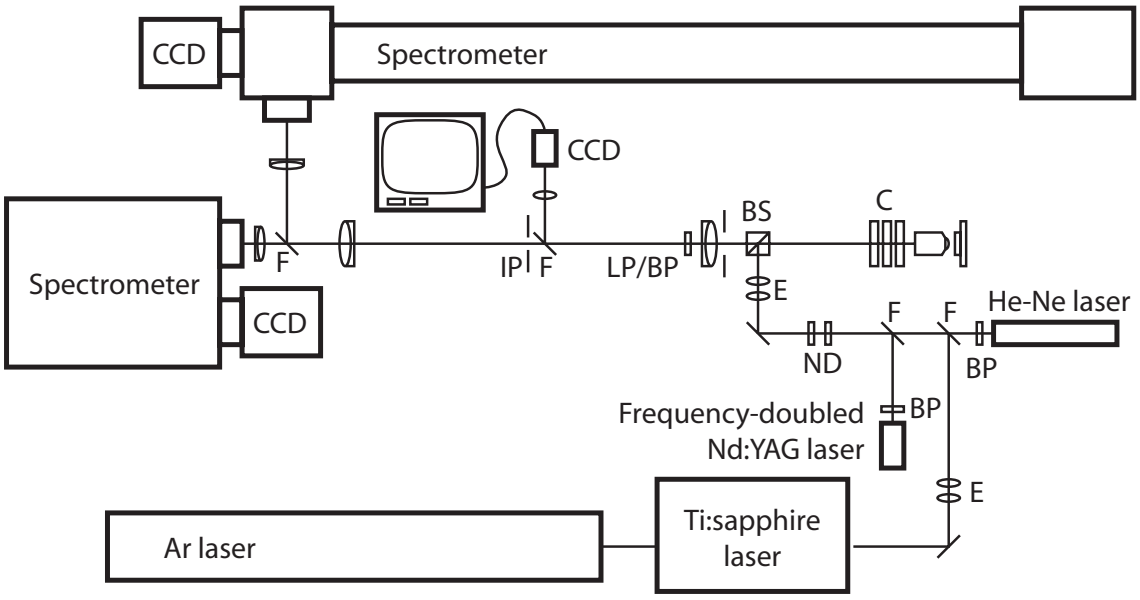

Figure 17: Setup for micro-photoluminescence experiments. Flip mirrors (F) were used to switch between different configurations of excitation and detection. Laser light was filtered using suitable band-pass (BP) filters and attenuated with adjustable neutral-density (ND) filters. A beam expander (E) was used to adjust the divergence of the beam. The beam passes through a (non-polarizing) beam splitter (BS), the cryostat windows (C), and the microscope objective. The objective collects the emitted photoluminescence, which passes back through the beam splitter. Reflected laser light is blocked using appropriate long-pass (LP) or band-pass filters. The PL is focused to an intermediate image plane (IP) where it is spatially filtered through an aperture and can be inspected using a CCD camera and monitor. Finally, the PL is dispersed in one of two spectrometers and detected with a thermo-electrically cooled CCD detector.

The spectrometer projects an image of the input slit along the vertical axis of the CCD, as pointed out above. The spatial resolution is given by the NA at the sample side, as well as the imaging properties of the spectrometer. Figure 17 shows the basic experimental setup used for micro-PL measurements. The microscope objective is focused to infinity and PL emitted from the sample is therefore collimated as it passes through the cryostat windows. The PL is focused to an intermediate image plane with a $100\times$ magnification, where it can be spatially filtered. The PL is again collimated and finally focused onto the input slit of one of the two spectrometers. For the high-resolution spectrometer, the image size at the input slit is $50\times$ magnified and the imaging onto the CCD chip is 1:1. Hence, one pixel corresponds to a distance of about $0.5\,\mu$m on the sample, which equals the spatial resolution of the objective at $\lambda \approx 700\,$nm.

3.3 Measurements of coherence times

The coherence time of three-dimensionally localized excitons is presently a topic of interest within the fields of semiconductor physics [26], optoelectronics [28], nano-optics [44], and the emerging field of quantum information technology [67]. Coherent spectroscopy has been applied for decades to study atoms, molecules and solids. The continuing developments in ultra-fast laser sources have pushed these investigations to ever shorter timescales, presently down to the femtosecond regime (see Ref. [26] and references therein). Numerous techniques have been applied to measure the coherence of excitons in semiconductors and semiconductor nanostructures. Two methods that have been employed for the study of exciton coherence in this thesis will be described below. Straightforward analysis of spectral linewidth can also yield information about the coherence time of localized excitons, and will be discussed first.

3.3.1 Linewidth analysis

The transition linewidth of a quantum mechanical system is related to the imaginary part of its frequency-dependent susceptibility. An evaluation of the susceptibility of a two-level system, with the inclusion of a radiative relaxation of the excited state [27], results in the characteristic Lorentzian lineshape for the absorption or emission process:

$$\alpha(\omega) \propto \frac{\gamma_{\mathrm{rad}}/\pi}{(\omega_0 - \omega)^2 + \gamma_{\mathrm{rad}}^2}, \tag{19}$$

where $\hbar\omega_0 = E_2 - E_1$ is the energy difference between the two levels, and $2\gamma_{\mathrm{rad}} = 1/T_1$ (see Sec. 2.1.4). The factor of two in the last expression arises because T_1 is associated with the radiative decay of the excited state *population*, $N_2 = N|C_2(t)|^2 = N_2(0)\exp(-2\gamma_{\mathrm{rad}}t)$. The FWHM spectral width of the radiatively broadened Lorentzian line in energy units is given by $2\hbar\gamma_{\mathrm{rad}}$.

The radiative lifetime is not the only factor affecting the transition linewidth. A "collisional" term should also be included (by analogy with the kinetic theory of gases) representing interactions with phonons or other carriers. As a simple approximation, the probability for an oscillator to stay unperturbed by collisions can be estimated to decay exponentially with time. The time decay is described by a time constant that can be thought of as representing the mean time between collisions. In the case of elastic collisions, only the phase of the wavefunction is affected and the collision rate equals the so-called pure dephasing rate, expressed as $\gamma_{\text{coll}} = 1/T_2^*$. Including γ_{coll} in the derivation of the susceptibility also results in a Lorentzian lineshape for absorption and emission. On the basis of lineshape analysis, it is therefore not directly possible to separate radiative and collisional broadening. The combined Lorenztian linewidth is given by $2\hbar(\gamma_{\text{rad}} + \gamma_{\text{coll}})$ or, equivalently, by $2\hbar/T_2$ (Eq. (9)).

With the detection system described in the previous section, it is possible to measure emission linewidths down to the order of the spectral resolution, shown to be as low as $16\,\mu$eV for wavelengths around $1\,\mu$m. This corresponds to measuring radiative lifetimes up to $T_1 \approx 50\,$ps for purely radiatively broadened transitions, or dephasing times up to $T_2^* \approx 100\,$ps for pure collision broadening, assuming that the emission lines are not broadened by spectral fluctuations (see below). In self-assembled InAs quantum dots at room temperature, T_2 is in the 100-fs range [68], corresponding to a homogeneous linewidth around 10 meV. Emission linewidths in this range have been observed in single-dot photoluminescence at room temperature, where near-field microscopy was used to isolate individual dots [69]. With decreasing temperature, however, the dephasing time increases, along with the spectral resolution required to measure the single dot linewidth. Results of linewidth analysis of three-dimensionally localized excitons in quantum wells and self-assembled quantum dots at low temperature are presented in Chapters 4 and 5, respectively.

In atomic systems, radiative and collisional broadening represent cases of *homogeneous* broadening, i.e. a broadening of absorption or emission occurring in indistinguishable atoms. Localized excitons in a solid-state system, on the other hand, are *not* indistinguishable. Wavefunctions of individual excitons differ, depending on the detailed shape of the confinement potential, affecting both the radiative rate and interactions with the environment. The definition of what constitutes homogeneous broadening in quantum dots is therefore somewhat blurred. In more general terms, the homogeneous linewidth reflects the time-energy uncertainty principle, with $\Delta E \Delta t \geq \hbar$, where Δt represents the time during which the particular state is unperturbed. It is therefore meaningful to talk about a homogeneous broadening in light emission from a single quantum dot, whereas an ensemble of dots cannot, strictly speaking, be characterized by one value of homogeneous broadening. In a realistic multi-level system the situation is further complicated by the fact that the contributions to the homogeneous broadening do not necessarily correspond to pure radiative and collisional broadening, as already discussed in Sec. 2.1.4. To prevent confusion, the symbols γ_{rad} and γ_{coll} will therefore be avoided and $\gamma_1 = 1/2T_1$ and $\gamma_2 = 1/T_2^*$ will be used to represent the different relaxation processes.

For a collection of atoms, *inhomogeneous* broadening is defined as arising from differences in the transition energies of individual oscillators, e.g. due to different velocities of atoms in a gas or due to differences in the local environment of atoms embedded in a solid [27], which makes the individual atoms distinguishable. This type of broadening has a clear parallel in quantum dot systems where transition energies can vary considerably between dots. However, the transition energy of *individual* dots can also vary on a time scale much longer than constitutes the homogeneous broadening, as discussed in Chapter 5. This broadening, caused by random fluctuations of local fields, represents a kind of inhomogeneous broadening of a single system in the time domain. The term inhomogeneous broadening, however, is usually applied to characterize an ensemble of oscillators and will therefore not be used here to describe broadening of single dot emission lines due to fluctuating fields. This kind of broadening cannot be considered as homogeneous either, since it does not involve a perturbation of the quantum mechanical state within the lifetime of the exciton and therefore does not enter into the time-energy uncertainty.

3.3.2 Four-wave mixing

A widely used method for measuring coherence times in semiconductors is four-wave mixing (FWM) [22, 23, 26], which involves interfering two intense laser beams at the sample position, inducing a periodic modulation of the refractive index of the medium through its non-linear response. This periodic modulation can diffract a third beam into a fourth direction (hence the name), and the diffracted signal is measured to obtain information about the response of the material. The temporal response can be investigated by using short laser pulses, delayed with respect to each other. A variant of the FWM technique is the two-beam degenerate FWM, which has been used in this work to measure dephasing times in self-assembled quantum dots. Special considerations were made because of the extremely low signal level from the dots, which is a consequence of their low absorption strength.

The setup for FWM experiments is shown in Fig. 18. A pulsed Ti:sapphire laser emits a train of short pulses, at a wavelength tunable from 780–920 nm (in the presently used configuration). The pulse duration is 120 fs, giving a transform-limited spectral width of about 15 meV. No additional pulse shaping was employed. The pulsed laser beam is split up into two arms which are modulated at different frequencies using a mechanical chopper. One pulse train can be delayed with respect to the other, using a computer-controlled delay stage. The laser beams are focused to the same spot on the sample where they interfere (when the two pulses arrive simultaneously). The sample was mounted in a liquid-He cryostat. In the present setup, the beams were focused from the back of the sample which is transparent at the wavelength of interest. This geometry was found to be favorable with respect to suppressing unwanted signals due to scattered light and multiple reflections within the samples. Multiple internal reflections were also significantly reduced by applying an anti-reflection coating (SiO_2) to the backside of the sample.

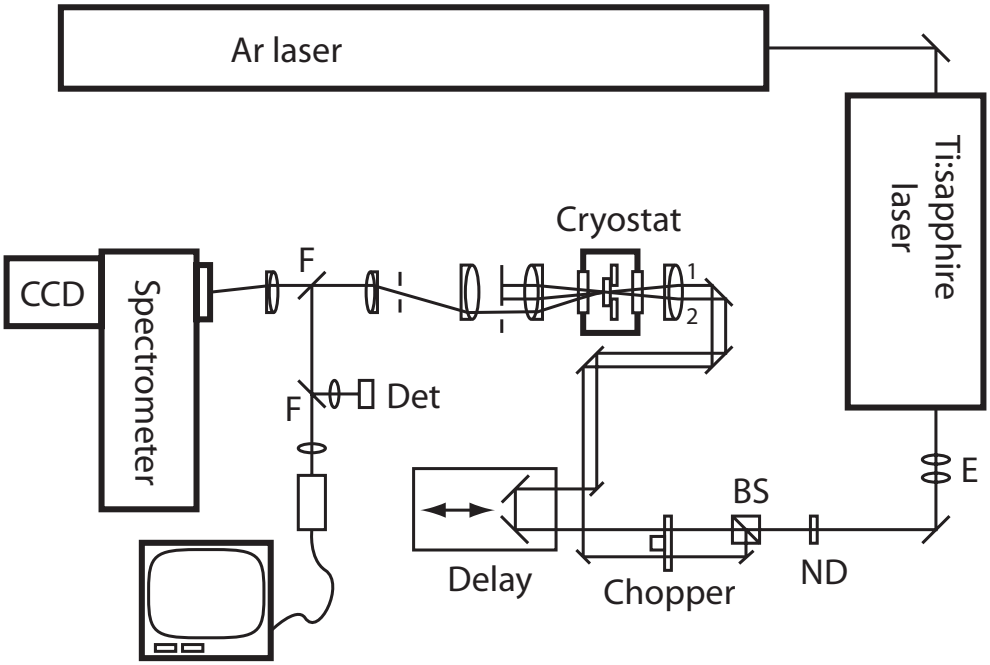

Figure 18: Four-wave mixing setup, described in the text. Labels correspond to those used in Fig. 17.

The laser beams incident on the sample are labeled 1 and 2 for convenience and the incident directions are given by the wave vectors $\mathbf{k}_1$ and $\mathbf{k}_2$, respectively. Beam 2 passes through the delay stage and the time delay between the pulses, τ_{12}, is said to be positive when pulse 2 arrives after pulse 1 (signals occurring at negative delays will not be discussed here). The intensity of the two beams is adjusted such that the intensity of beam 2 is roughly twice that of beam 1. Considering the case of a positive delay, pulse 1 arrives at the sample and induces a macroscopic polarization by resonantly exciting electron-hole pairs in the material. In the absence of inhomogeneous broadening, this polarization maintains its coherence for a limited time ($\approx T_2$) after the arrival of pulse 1. If pulse 2 arrives within this time, it interferes with the coherent polarization, resulting in a spatially modulated polarization grating. If the intensity of the incident beams is sufficiently high, this will result in a periodic modulation of the refractive index,[12] which diffracts a part of pulse 2 into the detection direction $2\mathbf{k}_2 - \mathbf{k}_1$. If the FWM signal is integrated over time, it has the following dependence on the time delay:

$$I_{\mathrm{FWM}}(\tau_{12}) \propto \exp(-2\tau_{12}/T_2) \qquad \text{(homogeneous broadening)}. \tag{20}$$

In the case of a quantum dot ensemble, where inhomogeneous broadening dominates over the homogeneous broadening, the situation is considerably different. Here, electron-

[12] The intensity dependence of the refractive index is related to the third-order non-linear susceptibility, $\chi^{(3)}$.

hole pairs are excited within a range of resonance frequencies, corresponding to the spectral width of the laser pulse (since this is typically narrower than the inhomogeneous broadening of the quantum dots). The phase evolution is different for different oscillators and the overall phase coherence is lost on a timescale similar to the pulse duration. Although no macroscopic polarization remains, the phase of the individual oscillators remains well defined with respect to the original pulse, within the dephasing time T_2. On the arrival of the second pulse at time τ_{12} after the first, the phase evolution of the oscillators is reversed. As a result, they are (partially) back in phase at a time $2\tau_{12}$ after the arrival of the first pulse, at which time they emit a so-called photon echo in the $2\mathbf{k}_2 - \mathbf{k}_1$ direction. Although the temporal shape of the echo signal depends on the range of resonance frequencies excited, the delay-dependence of the time-integrated signal is independent of the inhomogeneous broadening, and it differs from the homogeneously broadened case only by a factor of two in the exponent:

$$I_{\mathrm{FWM}}(\tau_{12}) \propto \exp(-4\tau_{12}/T_2) \qquad \text{(inhomogeneous broadening)}. \tag{21}$$

For systems where either homogeneous or inhomogeneous broadening dominates, the delay dependence of the FWM signal can therefore be used to directly derive the total dephasing time T_2.

The FWM signal from the sample was spatially filtered through an aperture in the far field as well as the image plane and detected (time-integrated) with a Si photodiode. The photocurrent from the diode was preamplified and measured at the difference frequency of the two beams using a lock-in amplifier to ensure that only a signal caused by the presence of the two beams was detected. By selecting the correct geometry, minimizing scattered light by focusing on a suitable position on the sample, carefully spatially filtering the signal, choosing the optimum level of preamplication, and using phase-locked detection at the difference frequency, the FWM signal intensity could be measured with a dynamic range covering 6 orders of magnitude.

3.3.3 Speckle analysis

A recently developed technique to measure the coherence of optical excitations in solids is time-resolved speckle analysis [70, 71], which involves analyzing the temporal behavior of intensity fluctuations (speckles) in *secondary emission* (SE). Secondary emission designates light that is emitted from an optically excited sample in non-specular directions (i.e. not transmitted, reflected, or diffracted), and therefore involves one or more scattering processes. SE includes contributions from incoherent photoluminescence and coherent Rayleigh scattering. Rayleigh scattering can arise from structural imperfections in the sample, and it is also strongly enhanced when the incident light is tuned close to an absorption resonance in the material (resonant Rayleigh scattering). Furthermore, the temporal behavior of the scattering following short-pulse excitation reflects the dynamics of the system. In a pioneering work, Hegarty *et al.* [72] pointed out that the resonant enhancement of Rayleigh scattering could be used to determine the homogeneous broadening

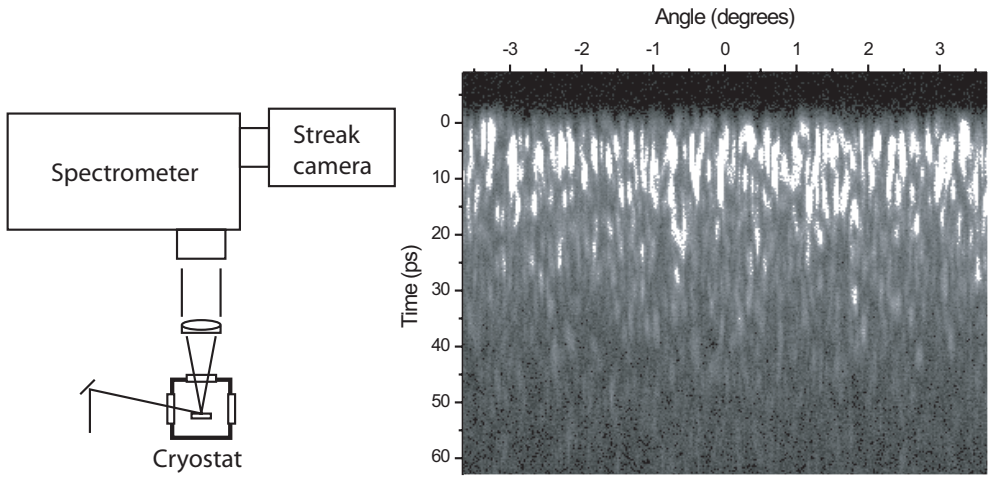

Figure 19: Speckle analysis: Experimental setup and a typical speckle pattern in secondary emission from an inhomogeneously broadened quantum well. The streak camera is rotated 90° from its conventional configuration so that its time axis is perpendicular to the spectrometer slit.

of optical transitions, even in an inhomogeneously broadened system. The time-dynamics and coherence properties of resonant SE have since been studied in detail (for a recent review, see Ref. [26]). Speckle analysis is particularly appealing method to investigate the SE since it can be used to directly evaluate the time-dependent degree of coherence without relying on interferometric measurements or non-linear processes.

For speckle analysis, samples were mounted in a liquid-He cryostat. Quantum-well or quantum-dot excitons were resonantly excited with pulses from a mode-locked Ti:sapphire laser at grazing incidence. SE emitted in different directions was collected perpendicular to the sample surface and synchronously detected with a streak camera, with a time resolution down to several picoseconds. The second axis of the camera was used for the angular detection. The experimental configuration is shown schematically in Fig. 19, along with a typical speckle pattern. Following the excitation at $t = 0$, coherent and incoherent light is emitted from the sample, $I = I_{\mathrm{coh}} + I_{\mathrm{incoh}}$. Due to interference, the coherent emission results in a speckle pattern in the angular direction. Furthermore, as a result of the inhomogeneous broadening of the excited resonances, the interference pattern evolves in time. The coherence of the secondary emission can be defined as

$$c = \frac{\overline{I_{\mathrm{coh}}}}{\overline{I}}, \tag{22}$$

where the bars denote an average over the emission directions. From the experimental data, the coherence at a given time can be determined by calculating the intensity variance

over a sufficient number of speckles ($N \geq 100$) in the angular direction

$$c^2 = N \frac{\overline{(I - \overline{I})^2}}{\overline{I}^2}. \tag{23}$$

For an inhomogeneously broadened ensemble of oscillators (frequency variance σ), the intensity of coherent emission is [70]

$$\overline{I_{\mathrm{coh}}} = e^{-2\gamma t}(1 - e^{-\sigma^2 t^2}) \approx e^{-2\gamma t}, \tag{24}$$

where the approximation is valid for $t > \sigma^{-1}$. In this limit, the SE coherence is given by

$$c = \frac{e^{-2\gamma t}}{e^{-2\gamma_1 t}} = e^{-2\gamma_2 t}. \tag{25}$$

From the speckle pattern, the two contributions to the dephasing rate ($\gamma = \gamma_1 + \gamma_2$) can therefore be independently determined, by separating the time decay of the SE emission intensity and its coherence.

4 Localized excitons in quantum wells

Interface roughness is an important parameter for the optical and electrical properties of quantum wells. The photoluminescence spectrum of quantum wells with imperfect interfaces is largely determined by how the length scales of the interface roughness compare to the diameter, localization length and diffusion length of the quantum-well excitons. When quantum wells are grown with molecular-beam epitaxy, the interface roughness can be tailored to some extent by interrupting the growth at the interfaces, as described in Chapter 2. This modifies the potential landscape in the quantum well plane, resulting in a varying degree of exciton localization and ultimately in a splitting of the exciton resonance into discrete peaks corresponding to quantum well thickness variations of one monolayer (ML). In this limit, a spatially varying micro-photoluminescence spectrum consisting of ultra-narrow lines can be observed, indicating the existence of zero-dimensional quantum-dot-like states.

This chapter describes optical investigations of GaAs/AlAs quantum wells fabricated with growth interruption at neither, one, or both interfaces. A continuous range of well widths was obtained by growing 3–4 quantum wells of different nominal thickness on a single wafer without rotating the substrate, as described in Sec. 3.1.1. Through growth-interruption (GI), the characteristic length scale of in-plane variations in the quantum well potential was tuned through several distinct regimes. Section 4.1.1 discusses the effect of weak exciton localization on photoluminescence lineshape in conventionally grown quantum wells. In Sec. 4.1.2 the effect of interrupting growth on either the top or bottom interface is investigated briefly. In these cases, the typical length scale of potential fluctuations is smaller than or similar to the exciton localization length and the interfaces are characterized as microrough. PL and micro-PL studies of quantum wells where growth is interrupted on both interfaces are presented in Sections 4.2 and 4.3. Finally, in Sec. 4.4, the time-resolved secondary emission from three-dimensionally localized excitons in quantum wells is investigated.

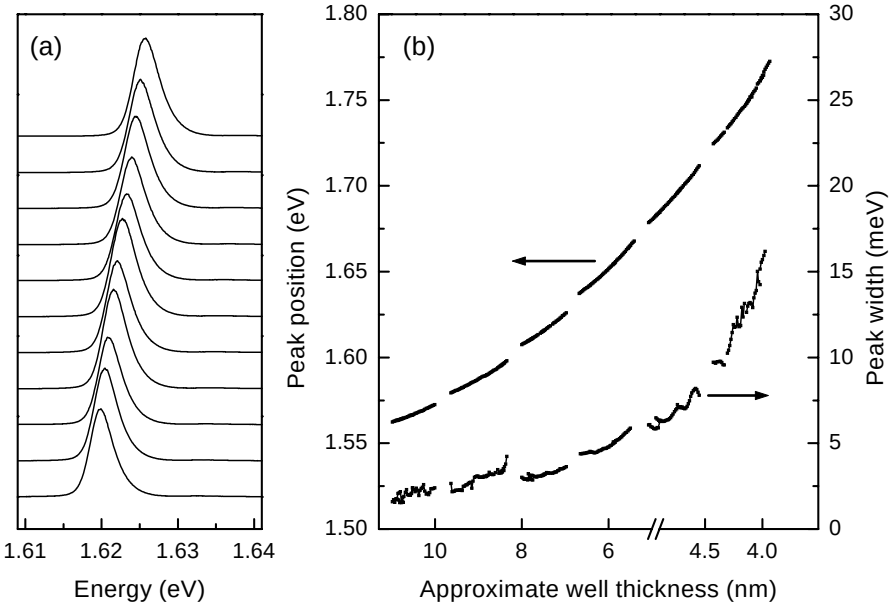

Figure 20: (a) Photoluminescence (measured at 50 K) of a continuously grown quantum well with varying thickness ($\approx$ 7-nm wide). The PL curves have been vertically offset for clarity. The total scan range corresponds to a thickness change of about 1 ML. (b) PL peak position and peak width (FWHM) for three quantum wells across the entire wafer. The position on the wafer has been converted to an approximate thickness scale.

4.1 Quantum wells with microroughness

MBE-grown quantum wells, grown continuously using typical growth rates, have a significant degree of interface roughness on the atomic scale, leading to a spatially varying potential in the quantum well plane. The potential is partially averaged over the electron and hole wavefunctions (see Sec. 2.4.1) and the exciton experiences an averaged center-of-mass potential, giving a finite inhomogeneous broadening of the excitonic resonance. Hence, the inhomogeneous broadening is often used as a measure of the structural quality of the quantum well [73]. The common case of quantum wells where (i) the interface roughness occurs on a length scale smaller than the exciton size and (ii) where the exciton-averaged potential fluctuations are much smaller than the exciton binding energy, have been treated theoretically in great detail (see, e.g., Refs. [74, 75, 76]). In this regime, the exciton-averaged quantum well potential can be adequately described as a white-noise potential, and only small corrections are introduced by more elaborate models [77]. As the length scale of interface roughness increases (e.g. as a result of growth interruption), the simple theoretical analysis breaks down and the problem must be considered numerically using a simulated interface structure.

4.1.1 Continuously grown quantum wells

Photoluminescence spectra from AlAs/GaAs quantum wells, grown using standard growth methods, were measured for reference. Fig. 20a shows the variation of the PL from a single quantum well for different points along a 5 mm section of the wafer. Similar spectra were recorded for three quantum wells across the wafer at 0.5-mm intervals, covering the full range of well widths from 4 nm to 11 nm. In Fig. 20b, spectral positions and widths (FWHM) of the luminescence peaks are plotted as a function of distance across the wafer. The position on the wafer has been converted into an approximate thickness scale for each well. The figure shows a smooth increase in transition energy and linewidth with decreasing well thickness, indicating that the exciton-averaged quantum well thickness varies smoothly across the wafer. The inhomogeneous broadening in narrower wells is larger because of the quadratic dependence of the confinement energy on the well width (it is reasonable to assume that the interface roughness is independent of the well thickness). MBE growth which occurs purely layer by layer would result in a distribution of monolayer-high islands which would coalesce into an atomically flat surface before islands of the next monolayer are formed. This would result in a periodic variation in the degree of interface roughness and, hence, in inhomogeneous broadening of the PL when scanning along the quantum well thickness gradient. The experimentally observed smooth variation in the PL peak width therefore suggests that the continuously grown wells have microrough interfaces extending through more than one monolayer with a fixed standard deviation. This is consistent with the results of Gammon *et al.* [31], obtained by measuring energies of confined LO-phonons in GaAs/AlAs quantum wells.

The PL spectra in Fig. 20 are recorded at a sample temperature of 50 K. At this temperature, the excitons can be assumed to be in thermal equilibrium, even in the narrowest wells measured here [78]. Consequently, the optical density of the quantum well can be determined directly from the measured PL spectra by assuming a Boltzmann distribution of carriers. The optical density of a 6-nm quantum well is plotted in Fig. 21, showing a broad asymmetric excitonic peak and the 2-D continuum edge (cf. Fig. 1). The experimental data was compared with the optical density for exciton states in a one-dimensional Gaussian random potential, derived analytically by Schnabel *et al.* [79]. This model takes into account the increased momentum uncertainty arising from localized exciton states in the fluctuating potential. For the ground-state exciton transition, the optical density, $\alpha(E)$, for a disordered potential with a mean energy E_0 is given by [79]

$$\alpha(E) \propto \frac{1}{2\eta}\left(1+\mathrm{erf}\left(\frac{E-E_0}{\sigma_E}-\frac{\sigma_E}{2\eta}\right)\right)\times\exp\left(\left(\frac{\sigma_E}{2\eta}\right)^2-\frac{E-E_0}{\eta}\right). \qquad (26)$$

The relevant fitting parameters are the standard deviation of the potential variation, σ_E, and the localization energy parameter, $\eta = \hbar^2\Delta K^2/2M$, derived from the wavevector uncertainty ΔK, with M being the exciton mass. The predicted lineshape corresponds well to the experimental data, as shown in Fig. 21. In addition to Eq. (26), a smooth step function of the form $(1+\exp[-(E-E_c)/\Delta E])^{-1}$ has been introduced to represent the

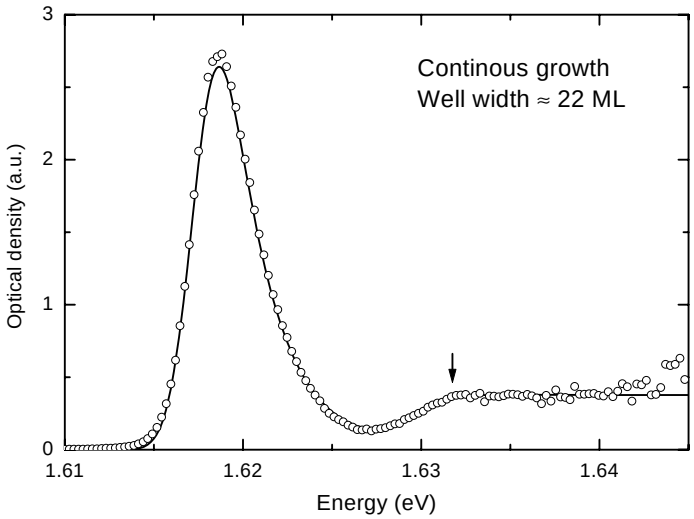

Figure 21: Optical density of a continuously grown quantum well. The asymmetric shape is indicative of exciton localization. The two-dimensional continuum edge is indicated with the arrow.

2-D continuum edge.

The potential variation σ_E derived from the lineshape fit is around 4 meV for the narrowest wells and decreases to 1 meV for the widest wells. In all cases, σ_E is significantly smaller than the exciton binding energy (see below), confirming the validity of the analysis. The localization energy parameter follows a similar dependence on well width, and the ratio σ_E/η is nearly constant for all wells and equal to 0.67 ± 0.03. This ratio is also close to the value obtained by Schnabel *et al.* in InGaAs quantum wells [79]. The σ_E/η ratio has been a subject of recent controversies regarding electronic and optical properties of disordered systems, as discussed in Sec. 4.4. The momentum uncertainty ΔK from the lineshape fit can be converted to a minimum localization radius via the uncertainty relation $\Delta K \Delta R > 1$, yielding lower limits for localization radii at 4 nm for the narrowest well, increasing to 8 nm for the widest. The latter value, however, is somewhat overestimated since the fitting procedure does not take into account the homogeneous broadening which contributes significantly to the linewidth in wider wells.

It is instructive to compare the localization radius with the two-dimensional exciton radius. The well-width dependent exciton binding energy can be determined directly from the PL spectra presented above. Following Ref. [80], it can be assumed that E_B equals the energy difference between the exciton density-of-states maximum and the continuum edge, which is indicated by the arrow in Fig. 21 (taken as $E_c + 3\,\Delta E$ in the fitted step function). Binding energies for different well widths are shown in Fig. 22, along with the theoretical prediction [80, 81] and previously reported data on GaAs/AlAs quantum

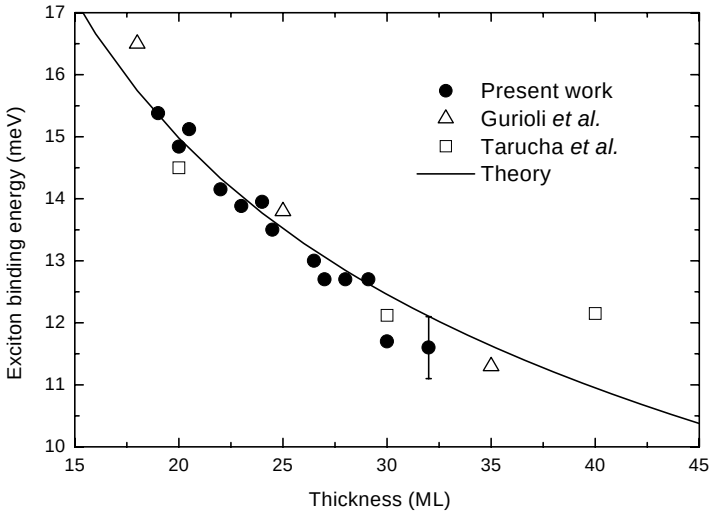

Figure 22: Well-width dependent exciton binding energy in GaAs/AlAs quantum wells. References to previous work are given in the text. The estimated uncertainty, arising mainly from uncertainty in determining the position of the continuum edge, is shown by representative error bars for one measurement point.

wells [80, 82]. The 2-D exciton Bohr radius derived from the binding energies is 6–7 nm in the whole range of quantum well widths investigated here. The localization radius is therefore similar to the exciton radius, reflecting the fact that the correlation length of the exciton-averaged quantum well potential in continuously grown quantum wells is determined by the exciton radius rather than the (shorter) correlation length of interface disorder.

4.1.2 Quantum wells with growth interruption at one interface

Atomic-resolution transmission electron microscopy and scanning tunneling microscopy studies generally confirm that atomically flat islands can develop on the GaAs surface upon interruption of MBE growth (see, e.g., Fig. 3). The lateral size of these growth islands can reach tens or hundreds of nanometers [83, 84], possibly with a distribution of ML-deep holes smaller than the exciton diameter [85]. Growth islands up to 15 nm × 40 nm on an $Al_{0.35}Ga_{0.65}As$ surface have also been reported [84]. Cross-sectional TEM measurements, however, revealed considerable microroughness on overgrown AlAs surfaces, even after growth interruption [83]. Below, PL spectra of quantum wells where growth has been interrupted at only one of the interfaces are presented.

Figure 23a shows PL from a quantum well where growth was interrupted at the bottom

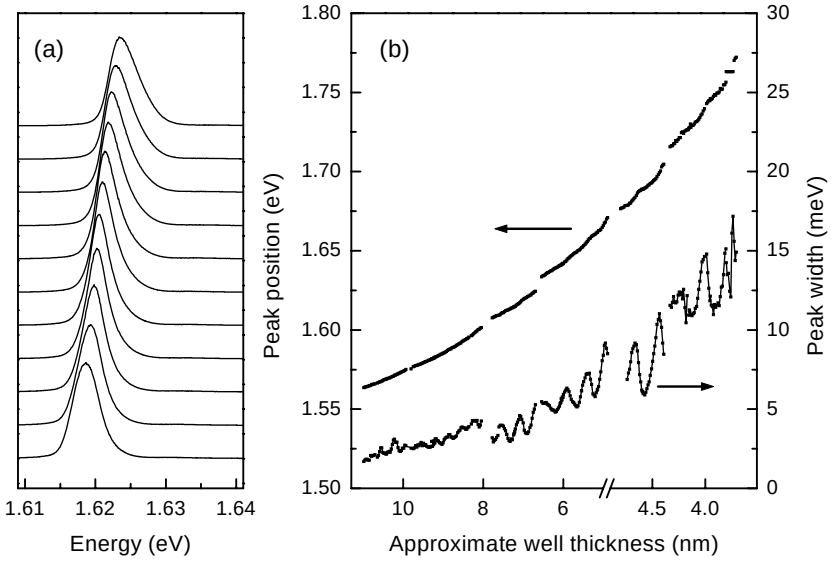

Figure 23: (a) Photoluminescence spectra from a quantum well where growth has been interrupted at the bottom interface. The PL curves represent a thickness change of about 1 ML. (b) PL peak position and peak width across the wafer.

interface only, i.e. after growing the lower AlAs barrier. The photoluminescence peak shape resembles that of the continuously grown quantum wells but the growth interruption introduces a slight modulation of the peak position as a function of well width, most clearly seen for narrow wells in Fig. 23b. Furthermore, the width of the PL peak oscillates strongly with the well thickness, in some cases dropping below the corresponding linewidth of the continuously grown well. The small change in the peak shape is consistent with TEM observations indicating that significant microroughness remains on the AlAs/GaAs interface after growth interruption [83]. The oscillations in peak width, however, indicate a degree of flattening of the bottom interface and a periodically varying island density. The periodic variation is attributed to a tilt of the bottom interface. The period of the observed linewidth oscillation corresponds to about half the monolayer thickness variation of the quantum well, i.e. to a gradient of about 0.1 ML/mm in the scan direction.

In the case of growth interruption at the top interface, the PL is split into a doublet (Fig. 24a). The *average* PL energy increases continuously with a weak modulation, similar to the previously described case. For intermediate well widths, the two peaks can be resolved and fitted individually. With decreasing well thickness, each individual peak shifts to higher energy and gains intensity and then stays pinned or moves to lower energies as the intensity drops again, with a decrease in the peak width (Fig. 24b). The partial splitting of the PL peak immediately confirms that growth interruption results in larger growth islands on the GaAs surface than on the AlAs surface. The amplitude

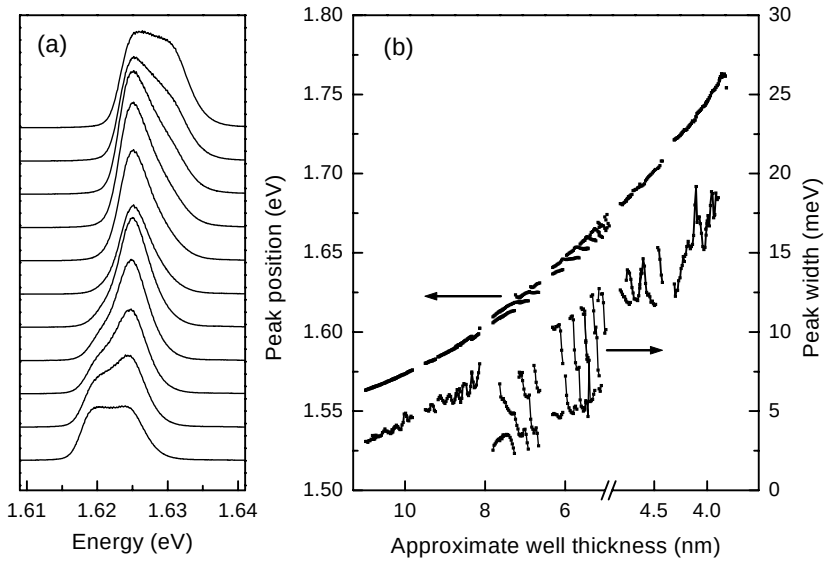

Figure 24: (a) Photoluminescence spectra from a quantum well where growth has been interrupted at the top interface. The PL curves represent a thickness change of about 1 ML. (b) PL peak position and peak width across the wafer.

of the potential variation (total peak width) also increases since the exciton no longer averages out the discrete thickness fluctuations on the top interface. The inhomogeneous broadening of the individual peaks is similar to the continuously grown quantum wells, reflecting the substantial roughness that remains at the bottom interface.

It is clear that the behaviour of the PL spectra plotted in Figs. 23 and 24 is not predicted by the simple white-noise potential model. The data can, however, be compared with the results of Castella and Wilkins [77], who have simulated the 2-D quantum well potential for larger length scales of potential fluctuations. In order to characterize the different regimes of interface roughness, a localization length parameter is defined, representing (approximately) the minimum lateral extension of a potential fluctuation which has a bound state:[13]

$$\xi_0 = \frac{\pi\hbar}{\sqrt{2MV_0}}. \tag{27}$$

where V_0 is the height of the lateral confinement potential and M is the exciton mass. In the simplified case of a quantum well with a flat bottom interface and a top interface with monolayer-high islands with a typical size ξ, the spectral shape of the quantum well density of states is determined by the ratio ξ/ξ_0 rather than simply the ratio of island

[13]This parameter has a finite value in the two-dimensional case, whereas a one-dimensional attractive potential always has at least one bound state.

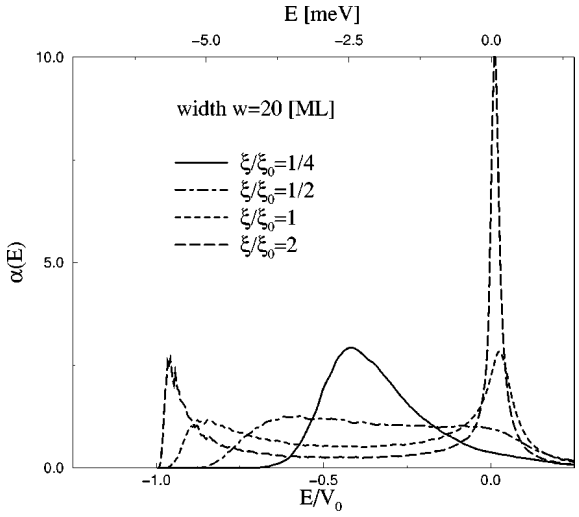

Figure 25: Calculated absorption spectra of quantum wells ($GaAs/Al_{0.4}Ga_{0.6}As$) with islands of different size on the top interface, showing a gradual splitting of the excitonic peak. The island coverage is fixed at 30%. From Ref. [77].

size to the exciton diameter [77]. Thus, longer-scale fluctuations are required to localize excitons in wider quantum wells.

Figure 25 shows calculated absorption spectra for different ξ/ξ_0 ratios. V_0 is set by the difference in the confinement potential between a quantum well of thickness n ML and $n+1$ ML. Although the real structure of the interfaces is more complicated than assumed in the calculation, there are clear qualitative similarities between the experimental data presented above and the calculated spectra for $\xi < \xi_0$. The spectrum evolves from a single asymmetric peak to a doublet structure with increasing island size. For $\xi/\xi_0 = 1/2$, the doublet is not well resolved, similar to the spectra of Fig. 24. It should be noted, that if the density of islands is low, a single peak is always expected for $\xi < \xi_0$, since there are no bound states. As the density of growth islands increases, however, they coalesce and form larger islands. This is fully consistent with the evolution of the PL signal in Fig. 24a from a double peak to a single peak for a thickness change of half a monolayer. The doublet structure is most clearly observed in quantum wells with a thickness below 8 nm ($\xi_0 = 14$ nm).

From the comparison with Fig. 25, it can therefore be concluded that the "effective" island size, defined by a combination of roughness on the two interfaces, is no larger than about 7 nm in the quantum wells presented above. The significant splitting of the exciton peak, predicted when the typical island is similar to or larger than the localization length, is only observed when growth is interrupted on both interfaces, as discussed in detail in the following section.

4.2 Quantum wells with monolayer islands

It was realized early on that growth islands with sizes comparable to or larger than the exciton diameter can be created by interrupting growth at both quantum well interfaces, resulting in a splitting of the PL into several lines with reduced inhomogeneous linewidth [73]. Initially, such narrow luminescence lines were assigned to laterally extended regions with a well-defined monolayer thickness [73, 86]. More detailed investigations on these "monolayer peaks" in growth-interrupted quantum wells revealed, however, that narrow exciton luminescence was not necessarily indicative of quantum wells having perfect interfaces and integer monolayer widths. Gammon *et al.* [87] demonstrated a wafer-to-wafer variation in absolute energies of ML peaks in GI GaAs/AlAs wells grown under nominally identical conditions. Warwick *et al.* [88] observed a significant variation in peak energy in $Al_{0.37}Ga_{0.63}As$/GaAs wells in a single sample which could not be explained by alloy fluctuations. The simplest model which can account for this behavior is that of bimodal interface roughness [88]. It is now commonly accepted that discrete luminescence lines can originate from extended quantum well regions that differ in effective thickness by approximately one monolayer and exhibit microroughness on a length scale smaller than the exciton diameter. Optically, the presence of microroughness has been inferred from measurements of GI GaAs quantum wells with $Al_xGa_{1-x}As$ ($x \leq 0.4$) barriers [89, 90, 91, 92, 93, 94] as well as pure AlAs barriers [31, 83].

In order to investigate this regime of interface roughness, measurements were carried out on two wafers, one containing three quantum wells (nominally 10 nm, 7 nm, and 5 nm) and another containing four wells (11 nm, 8.5 nm, 6.5 nm and 5 nm). In the following, these will be referred to as Wafer A and Wafer B, respectively. In both cases, growth was interrupted for 120 s before and after growing the well material and as before, binary barrier and well materials are chosen to eliminate effects of alloy composition on ML peak positions, making the results more reproducible. The sample structure and growth conditions were described in more detail in Sec. 3.1.1.

4.2.1 Monolayer splitting of quantum well excitons

Figure 26a shows the dramatic change in the quantum well photoluminescence spectra which occurs when a growth interrupt is introduced both before and after growing the wells. As predicted by numerical calculations (Fig. 25), the exciton luminescence splits into discrete peaks with nearly fixed positions, as shown in Fig. 26b. Only two or three peaks are observed simultaneously within an excitation spot of approximately 50 μm, demonstrating the high quality of the interfaces. As the probe is scanned across the surface, the position of each peak is generally pinned within ± 0.2 meV until the peak has lost approximately half its maximum intensity, then it broadens and shifts gradually to higher energies. From Fig. 26 it is evident that due to the peak shift, a sub-monolayer splitting between peaks will be observed when two or three peaks are simultaneously

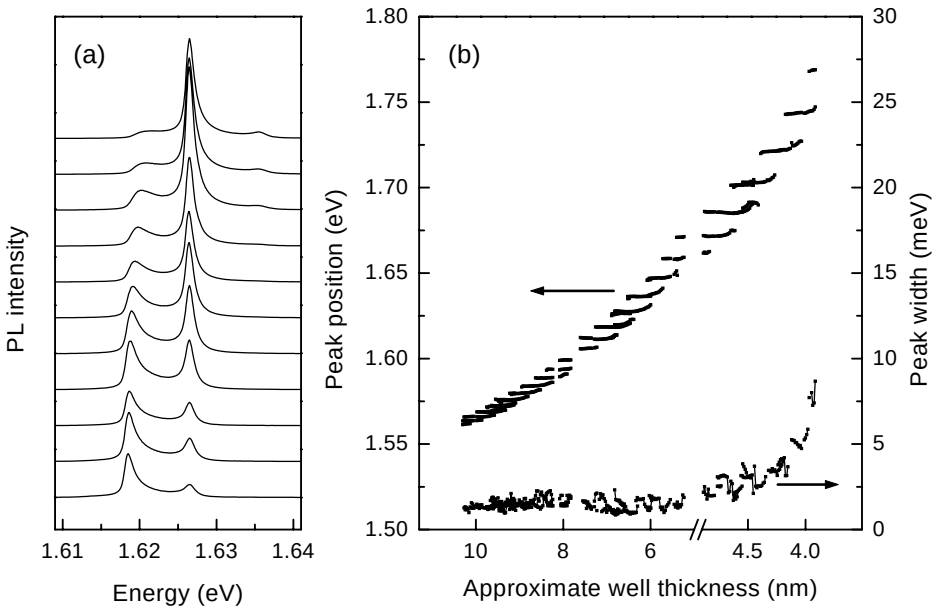

Figure 26: (a) Photoluminescence spectra (measured at 50 K) of a quantum well where growth has been interrupted at both interfaces. The vertically offset PL curves correspond to different positions on the wafer and the total scan range corresponds to a thickness change slightly below 1 ML. (b) Positions and widths of individual PL peaks for three quantum wells across the entire wafer.

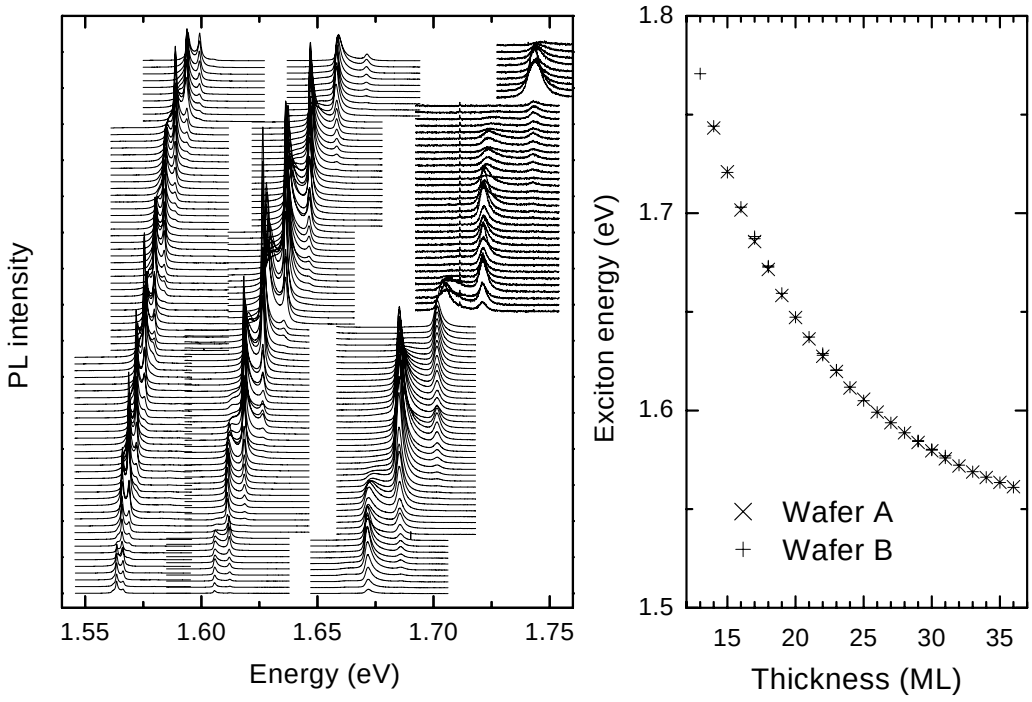

Figure 27: Photoluminescence spectra of growth interrupted quantum wells recorded at 50 K, showing the full range of monolayer peaks from 13 ML to 36 ML thickness. Monolayer peak positions measured on two wafers, grown under similar conditions, are plotted on the right.

visible in the spectrum. Such sub-monolayer splitting (typically 0.8–0.9 ML) has been previously reported in the literature [86, 88, 90, 92, 94].

Minimum linewidths of the monolayer peaks stay constant at around 1.3 meV in Wafer A, increasing to about 5 meV only for the narrowest wells. Similar discrete peaks were also measured in Wafer B, with minimum linewidths around 0.8 meV. The smaller linewidth can be partly attributed to reduced exciton electron scattering [95], supported by the observation of reduced trionic PL at low temperatures.[14] The narrow AlAs barriers in Wafer B allow for tunneling of free carriers to the spacer layers between the quantum wells, resulting in reduced charging effects.

Photoluminescence spectra measured for the three quantum wells across the entire surface of Wafer A are shown in Fig. 27. Peaks corresponding to 22 discrete quantum

[14]PL measured at T <30 K showed a considerably more complex spectral structure, with additional peaks appearing at the low-energy side of the monolayer peaks, which are attributed to charged excitons (trions) and defect-bound states.

well thicknesses differing by one monolayer can be resolved. The total thickness variation across the wafer is approximately 8 ML for the 10 nm well, 6 ML for the 7 nm well, and 4 ML for the 5 nm well, corresponding to a 23% thickness gradient across the whole wafer. This is in agreement with the thickness gradient expected from the geometry of the MBE reactor [47]. In order to determine accurately the absolute thickness of the wells, the position on the wafer is found where the thickness difference between wells (counted in ML steps in the PL spectra) matches exactly the RHEED-calibrated thickness difference. At this position, the actual well thickness must equal the nominal thickness and, therefore, absolute quantum well widths can be assigned to the series of ML peaks, accurate to within 1 ML. Similar spectra were recorded for Wafer B. A comparison of the PL spectra of Fig. 26a with the simulation shown in Fig. 25 suggests that the effective island size is similar to or larger than the exciton localization length. The monolayer peak splitting can be used to accurately determine V_0 in Eq. (27) as a function of well width, giving a localization length which varies approximately linearly from 6 nm for a 14-ML well to 17 nm for a 35-ML well (see Fig. 28).

The positions of all monolayer peaks from Wafers A and B are plotted in Fig. 27. The data points correspond to the energies at which the PL peaks are pinned before blue-shifting as the peaks lose intensity. From the figure, it is clear that ML peak positions within each wafer and between wafers are in excellent agreement. Typical variations in peak position between Wafers A and B are of the same order as the variation within the wafers (below 0.5 meV). For larger well widths, the agreement is in many cases better than 0.1 meV which, for well widths around 7 nm, corresponds to a maximum exciton-averaged thickness difference of less than 0.02 ML. It should be emphasized that, besides the different barrier configurations and different nominal well widths, several months passed between the growth of Wafers A and B, proving that *reproducible* ML peak positions can be obtained under similar growth conditions. The largest deviations in peak positions (up to 0.3 ML) are observed for the narrowest wells (<16 ML) and for peaks measured close to the wafer edges where growth tends to be anomalous. The fact that reproducible monolayer positions are observed immediately indicates that *atomically flat* surfaces are formed upon growth interruption, since a degree of microroughness on the growth surfaces would result in a randomness in the monolayer peak energy at different positions on the wafer and on different wafers. This does not imply, however, that the quantum well *interfaces* are atomically flat, since a segregation of atoms from the well into the barrier occurs during overgrowth, as discussed in the following section.

4.2.2 Modeling monolayer peak energies

In the literature, simple quantitative models have generally been employed in order to explain the experimentally observed ML peak splitting in the exciton luminescence from growth-interrupted quantum wells. These models assume that one or both interfaces consist of extended monolayer-high but atomically rough areas with sizes comparable to

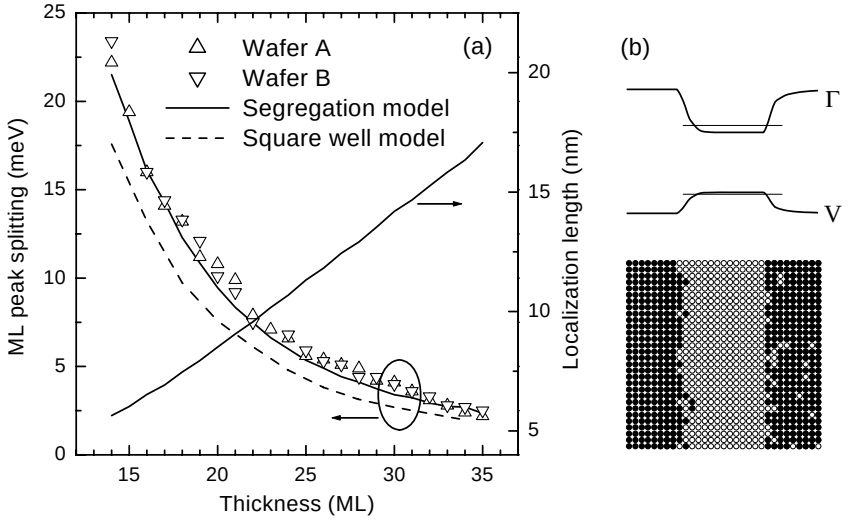

Figure 28: (a) Experimental values of the monolayer splitting in growth-interrupted quantum wells (symbols) and calculated results for two types of quantum well potential (lines). The in-plane localization length parameter for the quantum wells is also shown. (b) Simulated interface structure of a 14-ML quantum well with initially monolayer-flat growth interfaces along with the corresponding well potential.

or larger than the exciton radius [31, 83, 84, 86, 87, 88, 91, 92].

With knowledge of the accurate (within 1 ML) width of the growth-interrupted quantum wells, it is possible to model the transition energies of the monolayer peaks. Solutions of the one-dimensional Schrödinger equation for a simple finite-barrier square well potential, however, deviate significantly from measured transition energies, especially in narrow quantum wells. In order to generate a more realistic quantum well potential, surface segregation of atoms during overgrowth should be taken into account [46]. Calculated ML peak splittings for the two types of well potential and measured values from wafers A and B are plotted in Fig. 28a. The calculated interface structure and the resulting quantum well potential for a 14 ML quantum well are shown schematically in Fig. 28b. Excellent agreement between calculated and measured values of the peak splitting is obtained when segregation effects are included. The calculation of the electronic states was carried out using the methods described in Sec. 2.4.2. Well-width dependent heavy-hole exciton binding energies were calculated using the interpolation formula provided by Gurioli *et al.* [80] (shown in Fig. 22).

Surface segregation results in an atomically rough interface structure, even though monolayer-flat growth islands are formed following growth interruption. The segregation

of Al atoms into the GaAs quantum well gives atomic roughness extending only through approximately 2 ML, according to the simulation. The segregation length of Ga in AlAs is longer than that of Al in GaAs, but the effect of Ga segregation on transition energies is smaller since it occurs in the barrier rather than the quantum well. The bimodal interface roughness is a direct consequence of atomic segregation during overgrowth of growth interrupted surfaces and gives inhomogeneously broadened monolayer peaks with positions and widths that depend on growth parameters. Surface segregation might be responsible for the blue-shift of ML peaks observed with increasing growth temperatures [31, 96], although the peak shift reported in these studies is larger than predicted by the present model.

4.3 In-plane exciton localization

In the previous section, it was shown that monolayer peaks in growth-interrupted quantum wells are pinned at a certain energy over a range of well widths but exhibit a blue-shift before fully disappearing with decreasing well thickness. This shift, and the simultaneous broadening of the monolayer peak to the high energy side, can be attributed to exciton localization in the plane of the quantum well, caused by monolayer thickness fluctuations. In the narrowest wells measured here ($w \leq 4.5\,\mathrm{nm}$), the combined electron and hole confinement potential V_0, given by the monolayer peak splitting, is similar to the exciton binding energy. In wider wells, the electron and hole confinement potentials are considerably smaller than E_B and the excitons can be considered as being localized in quantum dots belonging to the weak confinement regime [28].

Due to reduced scattering, the homogeneous linewidth of localized excitons is substantially narrower than that of delocalized excitons [97, 98]. In the photoluminescence spectra presented above, this reduction in linewidth is masked by the inhomogeneous broadening resulting from sampling over a relatively large area, which averages over many localized states. By reducing the probe area, ultra-sharp lines have previously been observed in quantum well photoluminescence and attributed to the roughness-induced localization of exciton states [39, 40, 99, 100]. Fig. 29a shows a micro-photoluminescence spectrum of a $\approx$21 ML growth-interrupted quantum well, spatially resolved in one dimension. The PL is excited through the microscope objective with a 25-μm defocused laser spot. A pattern of spectrally sharp peaks is clearly visible on the low-energy side, each peak arising from an area smaller than the spatial resolution. Substantial fine structure is also seen on the high-energy peak, indicating a degree of microroughness on the extended growth islands. The broadening of the monolayer peak amounts to an exciton-averaged thickness fluctuation below ± 0.1 ML, consistent with atomic-scale segregation-induced roughness. In the 50-K PL spectra presented above, the thermal energy of the excitons exceeds the inhomogeneous broadening of the upper monolayer peak and excitons populate delocalized states above the mobility edge, while at 10 K, weakly localized states within the upper monolayer peak become increasingly populated.

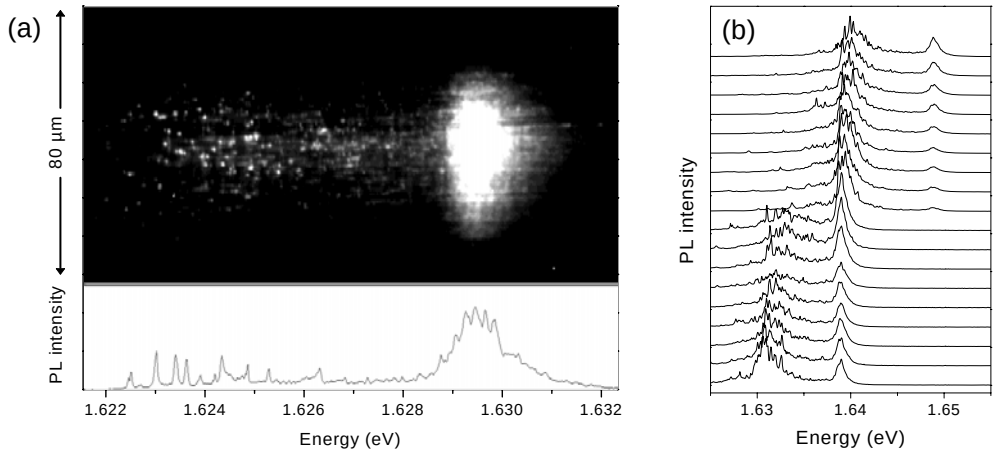

Figure 29: (a) Spatially resolved photoluminescence, measured at 10 K. The lower panel shows a cross section through the upper image, representing PL emission from an area on the sample corresponding to the spatial resolution of the detection system. (b) Micro-photoluminescence spectra from a growth-interrupted quantum well, recorded at different wafer positions, corresponding to a total well thickness variation of 1 ML. The spectra have been vertically displaced for clarity.

Micro-PL spectra for a range of quantum well widths (Wafer A) are plotted in Fig. 29b, covering a total thickness change of one monolayer. As the probe is scanned in the direction of decreasing well thickness, each monolayer peak first appears with a width around 1 meV, increasing in intensity to a maximum value without broadening or shifting in energy. As the well thickness decreases further, the peak broadens and shifts to higher energy, and individual emission lines become more clearly resolved. These observations are consistent with the interface model discussed in the previous sections and confirm that the broadening and shifting of ML peaks occurs simultaneous to the appearance of spatially localized exciton states with different quantization energies.

To illustrated the localization features more clearly, Fig. 30a shows micro-PL spectra from a narrower quantum well, recorded with a high spectral resolution. The top spectrum is excited with a 1-μm laser spot but collected from a larger area, while the bottom spectrum is excited and detected through a sub-micron-sized aperture. The position of (delocalized) exciton peaks corresponding to 18 and 19 ML thickness were determined from the 50 K PL data and corrected for the temperature dependence of the bandgap. The intensity of the upper monolayer peak is dramatically reduced in aperture-PL, consistent with the more delocalized nature of these states. Individual sharp lines corresponding to more strongly localized excitons are clearly identified, however. For these lines, the lateral size of the confinement potential can be estimated with a simple model by assuming a two-dimensional square box shape for the dots. The calculation indicates a wide size

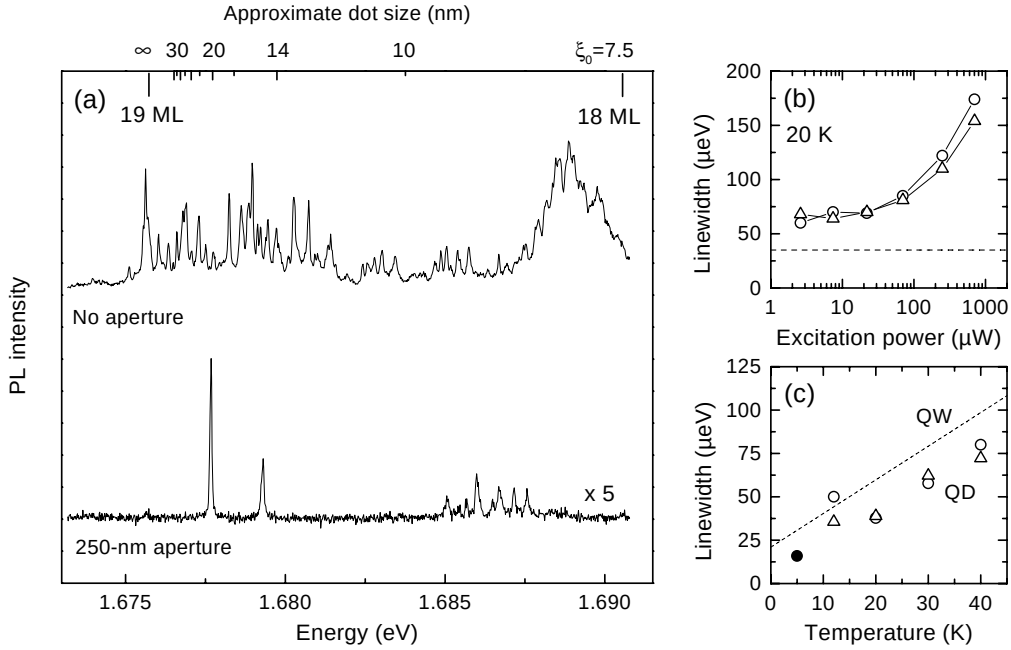

Figure 30: (a) Micro-photoluminescence spectra of a 5-nm growth-interrupted quantum well at 12 K. The lower spectrum is measured through an Al mask with a 250-nm aperture. The top axis indicates an approximate lateral size of the exciton localization potential. (b) Excitation power dependence of the single-dot linewidth. (c) Temperature dependence of the single-dot linewidth (open symbols). The dashed line shows the homogeneous linewidth in a continuously grown quantum well (from Ref. [71]). The solid circle shows the homogeneous linewidth determined from speckle analysis (see Sec. 4.4)

distribution of dots, with typical sizes ranging from approximately 12 nm to 50 nm.

The spectral linewidth of a number of individually localized excitons was determined from micro-PL spectra recorded through different apertures. The linewidth shows no systematic dependence on the dot size and typically lies in the range 50–70 μeV at 12 K (before correcting for the spectrometer response). The intensity of the single lines increases linearly with excitation power up to about 10 μW and saturates fully at around 300 μW due to Pauli blocking of the individual state. The spectral linewidth increases more rapidly above the saturation point, as shown in Fig. 30b, although the dependence is still sub-linear ($w \propto P^{0.35}$). The two lines plotted in the figure are emitted from dots with a similar quantization energy (≈ 4 meV). When the temperature is increased from 12 K to 20 K, the variation in linewidth between dots is considerably reduced, suggesting that the linewidth at low temperature is affected by local field fluctuations due to trapping of charges at shallow localization centers in the vicinity of the dots, resulting in a dot-dependent spectral jitter of photoluminescence lines. The slight increase in temperature is sufficient to thermally excite the weakly localized carriers and average out these fluctuations. Local field fluctuations are discussed in more detail in Sec. 5.2.1.

The single-exciton linewidth increases with temperature whereas the intensity decreases rapidly until only a broad PL background is detected at around 50 K. Fig. 30c shows the linewidth as a function of temperature, corrected for the spectrometer response. The linewidth increase is comparable to the 2.0-μeV/K (FWHM) acoustic phonon scattering coefficient measured in narrow (continuously grown) GaAs quantum wells [71], although the dot linewidth is slightly lower. Furthermore, a 16-μeV linewidth is measured at 5 K, as discussed in the following section. On the basis of this data, it is not possible to confirm whether the linewidth shows a thermally activated increase corresponding to acoustic-phonon scattering between discrete exciton levels, similar to that initially reported by Gammon, *et al.* [101]. However, the linearity of the data (excluding the 10-K values) is consistent only with a low activation energy (≤ 1 meV).

4.4 Secondary emission from growth-interrupted quantum wells

Time-resolved secondary emission from excitons in growth-interrupted quantum wells was measured and speckle analysis was used to determine the homogeneous linewidth. The SE from a 6.5 nm quantum well (Wafer B) is shown in Fig. 31a. The inset shows the time-integrated SE spectrum when the excitation is in resonance with the upper monolayer peak, revealing a strong resonant enhancement of the SE, as well as relaxation to localized states within the lower monolayer peak. The SE intensity from the upper peak decays monotonically with time, following the short-pulse excitation, while the SE from the lower peak shows an initial rise and a subsequent, slower decay. The secondary emission from the upper monolayer has an initial coherence (Fig. 31b) which decays exponentially in time, while the emission from the lower monolayer is incoherent, consistent with a relaxation process involving phonon emission.

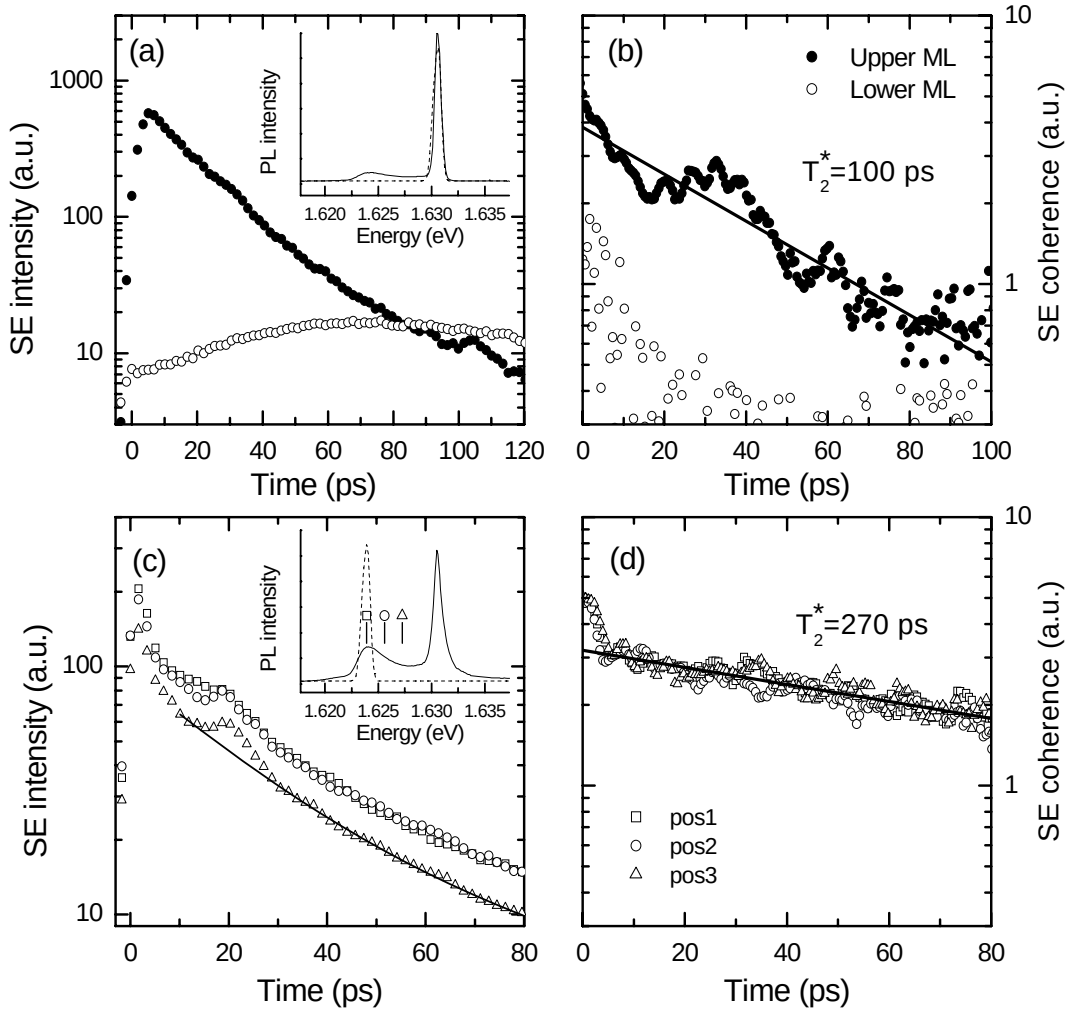

Figure 31: (a) Time-resolved intensity of secondary emission from a growth interrupted quantum well, for resonant excitation of the upper monolayer peak. The resonant SE (solid circles) and the SE from the lower monolayer peak (open circles) was detected. The inset shows the spectrally resolved time-integrated SE (solid line) and the spectral shape of the laser pulse (dashed line). (b) Coherence of secondary emission from the upper monolayer peak, showing an exponential time decay. The oscillations in the data are caused by an insufficient number of statistically independent speckles in the analysis. The non-resonant emission is incoherent (within the experimental uncertainty). (c) SE intensity for excitation of different parts of the lower monolayer peak, indicated in the inset. The solid line is a representative double exponential fit. (d) Coherence decay within the lower monolayer peak.

Figures 31c and 31d show the intensity and coherence of secondary emission when different parts of the lower monolayer peak are resonantly excited. The inset of Fig. 31c shows the time-integrated spectrum, excited with a laser pulse covering both monolayer peaks, as well as the spectrally narrower pulse used for probing the localized excitons at different energies. Resonant excitation of localized states in the lower monolayer peak results in an immediate rise of the Rayleigh scattering, in contrast with the quadratic rise expected for a spatially invariant but inhomogeneously broadened ensemble of oscillators (Eq. (25)), as demonstrated in Ref. [104]. The time dependence of the SE intensity and coherence are similar for the three positions within the monolayer peak, consistent with the energy-independent linewidth observed in micro-PL. The population decay in Fig. 31c can be fitted with double exponential decay curves. Similar decay constants of approximately 16 ps and 60 ps were obtained for all three excitation energies. This behavior agrees with population relaxation in monolayer islands that was measured in a transient grating experiment by Fan *et al.* [103]. The initial population decay of the localized excitons is slightly (less than a factor of two) slower than in the upper monolayer peak. Although the origin of the two population decay times is not quite clear, it can be assumed that the slower decay represents a state lifetime of an exciton ensemble which is closer to a quasi-equilibrium state [103]. The SE coherence of the localized excitons decays with a time constant $T_2^* = 270$ ps, nearly three times larger the one measured for the upper monolayer peak and up to four times larger than typical coherence times measured in continuously grown quantum wells at this temperature.

The results of the speckle analysis on the 6.5 nm growth-interrupted quantum well are summarized in Fig. 32. The average homogeneous linewidth (FWHM) of the localized excitons at 5 K is around 16 μeV, as also shown in Fig. 30. Contrary to previous reports [103], the contribution of "pure" dephasing (γ_2) determined here is not negligible and the ratio between the two contributions is similar to that reported for a continuously grown quantum well [71] at a similar temperature. The above analysis also quantifies the transverse relaxation at low temperature more accurately than in Ref. [103], where it is deduced by subtracting a lifetime contribution, inferred from a non-exponential population decay, from the homogeneous linewidth.

Recent measurements on Rayleigh scattering from multiple quantum wells (MQWs) showed oscillations in the time decay of the secondary emission intensity which were attributed to quantum-mechanical level repulsion in the disordered potential [105]. In order to explain the observed results, the authors used σ_E/η ratios ranging from approximately 4 to 30 to characterize the disorder potential of different quantum wells with similar thickness (presumably grown without growth interruption). These values are far from the ratio determined in Sec. 4.1.1, and show a surprisingly large variation between wells. It was later shown that the temporal oscillations in SE intensity can arise from exciton-polariton coupling between different quantum wells in the MQW structure [106]. Level repulsion might, however, play a role in growth interrupted quantum wells where the length scale of interface roughness has been tuned to a suitable value. It has been predicted, that evidence of level repulsion can be derived from level statistics in micro-photoluminescence

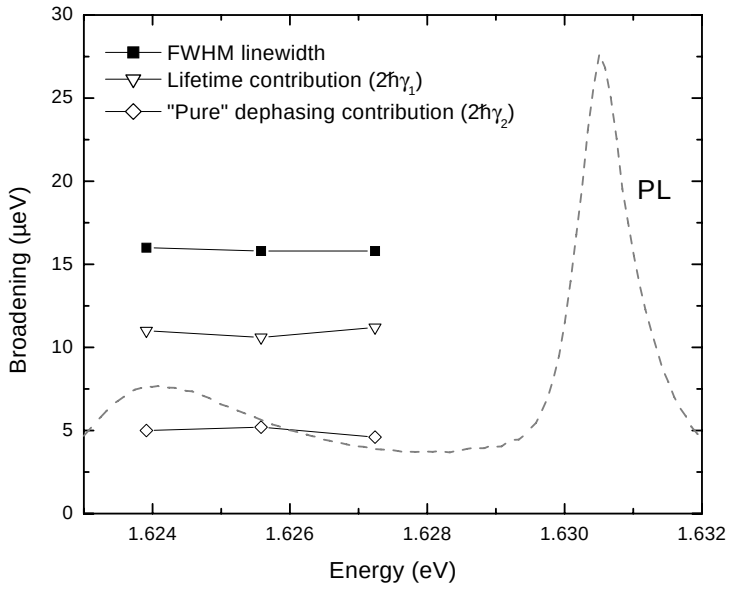

Figure 32: Contributions to the homogeneous linewidth at 5K, determined from speckle analysis of secondary emission. The photoluminescence spectrum is shown for reference (dashed line).

spectra [107]. Preliminary investigations of this kind were carried out using the present set of growth-interrupted quantum wells but no conclusive evidence for level repulsion was found, partly because of anomalously increased single-exciton linewidth at low temperature. It is plausible, however, that level repulsion can be observed in micro-PL by selecting the correct combination of temperature, probe area, and correlation length.

5 Self-assembled quantum dots

In recent years, interest in self-assembled quantum dot (SAQD) systems has grown rapidly. This has been partially driven by their technological promise for optoelectronic applications. Quantum dot lasers based on the (In,Al,Ga)As material system have received particular attention [108], and the limits of emission wavelength, power, and threshold current in such devices are being pushed further and further. The optical response of single SAQDs is also a subject of intense research, having strong similarities with atomic spectroscopy [109]. In spite of rapid developments within SAQD research, however, a lot of questions remain unanswered. Relatively little is known, for example, about their non-linear optical response [26]. The optical and electronic properties of self-assembled quantum dots are, in general, quite complicated and can vary significantly depending on the particular materials and fabrication methods. Furthermore, accurate theoretical modeling of the electronic structure of strain-induced self-assembled quantum dots remains a formidable task and simulations of realistic dot structures have only recently been presented [35].

This chapter presents optical investigations on self-assembled InGaAs and InAlGaAs quantum dots. A description of the sample fabrication has been given in Sec. 3.1.1. Basic optical characterization of the quantum dot samples, using photoluminescence and photoluminescence excitation spectroscopy will be described in Sec. 5.1. Sec. 5.2 discusses micro-photoluminescence studies on these samples, in particular the photoluminescence linewidth of individually localized excitons. In Sec. 5.3, the linewidth is compared with the homogeneous linewidth of the dot ensemble measured using four-wave mixing techniques.

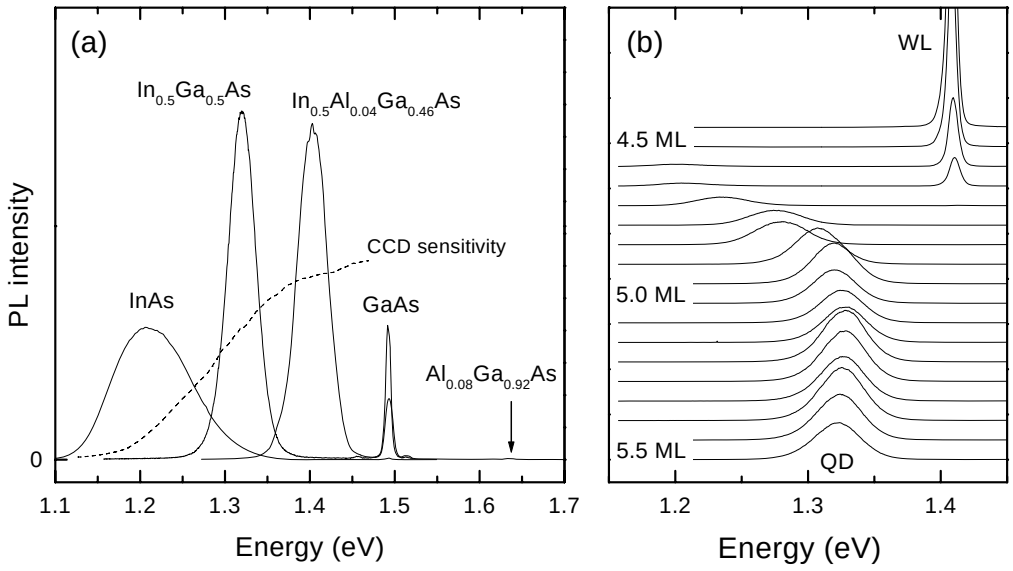

Figure 33: (a) 10-K PL spectra for InAs/GaAs, InGaAs/GaAs and InAlGaAs/AlGaAs quantum dots, normalized to the same integrated emission intensity. The arrow indicates the position of the AlGaAs barrier. The sensitivity curve of the silicon CCD detector is shown as a dashed line. (b) PL spectra recorded across a whole wafer, corresponding to different deposited thickness of InGaAs, as indicated.

5.1 Basic optical properties

5.1.1 Energy-level engineering

The emission wavelength of InAlGaAs-based quantum dots, typically grown with molecular-beam epitaxy or metalorganic chemical vapor deposition, can be tuned within a large range. Recent studies report emission wavelengths from 650 nm (InAs/AlGaAs, 4.2 K) [110] to 1520 nm (InAs/InGaAs, 300 K) [111]. The emission wavelength can be changed by varying the growth conditions (e.g. Refs. [112, 113]), the chemical composition of the dots (e.g. Refs. [54, 55]) or the barrier material (e.g. Refs. [114, 115]), or by introducing thin layers of material (with a composition different from the barrier) on top of and/or below the dot layer (e.g. Refs. [116, 117, 118, 119]). In many cases, the emission wavelength is engineered to match specific application areas but for the present work, the main focus was on tuning the quantum dot emission to overlap with the range of available detectors and laser sources. Preliminary investigations were also made on using thermal annealing to shift the QD emission wavelength, as discussed below.

Photoluminescence from three quantum dot samples is shown in Fig. 33a. Pure InAs

quantum dots (4 ML deposited) show broad emission around 1.21 eV, close to the detection limit of silicon-based CCD detectors. Emission was shifted to 1.32 eV by growing $In_{0.5}Ga_{0.5}As$ dots on GaAs. The energy was further increased to 1.40 eV by adding Al to the dots and barrier. The PL peaks from the latter samples have a Gaussian shape with a FWHM of 40 meV and 41 meV, respectively. A sample of $In_{0.5}Ga_{0.5}As$ dots with $Al_{0.35}Ga_{0.65}As$ barriers (not shown here) showed a weak QD luminescence at 1.57 eV. The ground-state exciton energy of the $In_{0.5}Ga_{0.5}As$ dots is substantially higher than the value calculated in Sec. 2.4.2, whereas the wetting layer energy (see below) fits almost exactly. The discrepancy can be partly attributed to the simplicity of the model, which does not correctly describe the geometry or the strain distribution in the dots. The experimental data suggests that a disk-like geometry, with a dot height smaller than indicated by AFM measurements, gives a more appropriate picture. This is consistent with partial evaporation of the dots during overgrowth.

All the samples discussed here were grown without substrate rotation and continuous variations in deposited thickness and composition across the wafers are therefore observed. Fig. 33b shows PL spectra along the thickness gradient (constant composition) of the wafer containing $In_{0.5}Ga_{0.5}As$ dots. At 4.5 ML deposited thickness, only luminescence from the wetting layer is observed. As the thickness increases, quantum dots start to appear and the wetting layer peak simultaneously shifts to higher energy and decreases in intensity, indicating an efficient carrier relaxation to the dots. Initially, the QD emission occurs at low energy but around the nominal deposition thickness of 5 ML, the dots have developed into a stable shape, in accordance with RHEED observations (Fig. 9). As more material is deposited, the dot luminescence is slightly red-shifted, corresponding to an increase in the dot size. AFM investigations confirm that dots first form in tight clusters around structural defects on the substrate acting as nucleation sites, but eventually develop into a randomly dispersed ensemble of dots with similar shapes and sizes (see Fig. 4) and a density of $1–2\times10^{10}\,cm^{-2}$.

5.1.2 Temperature dependence

Figure 34a shows the temperature dependence of the PL peak position for $In_{0.5}Ga_{0.5}As$ quantum dots. At low temperature, the peak position follows the $In_{0.5}Ga_{0.5}As$ bandgap [120], with a constant offset of approximately 0.5 eV added to account for strain and confinement effects. Above 75 K, the PL peak position deviates from this curve and approaches the curve defined by a thermalized carrier population, assuming a Maxwell-Boltzmann distribution of carriers within the quantum dot states. It can be concluded that the dots are randomly populated with carriers (flat distribution) below 75 K and the PL intensity therefore corresponds directly to the (optical) density of states. Above 125 K, however, the thermal energy is sufficient for carriers to fully thermalize within the quantum dot ensemble. The integrated PL intensity (from dots, wetting layer and barrier) decreases with temperature, especially above 250 K.

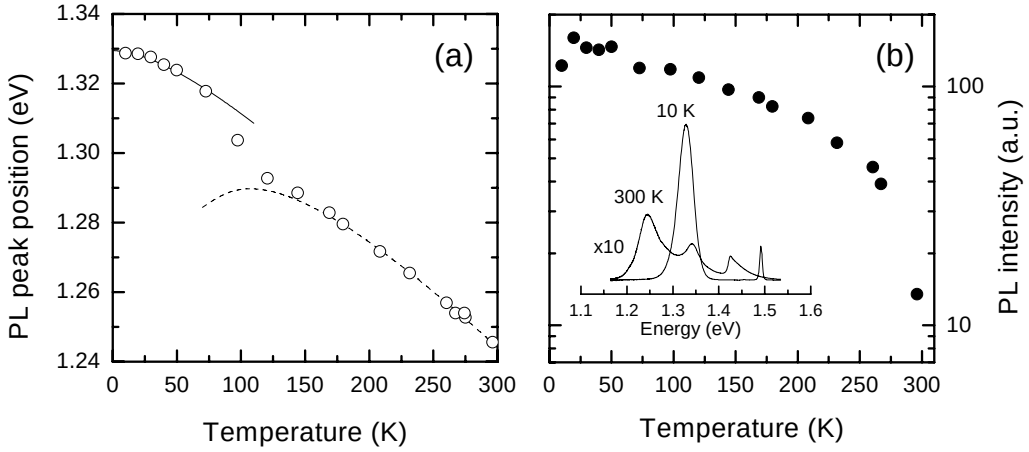

Figure 34: (a) Temperature dependence of the PL peak energy for $In_{0.5}Ga_{0.5}As$ quantum dots. The solid line follows the $In_{0.5}Ga_{0.5}As$ bandgap while the dashed line takes into account thermalization within the dot ensemble. (b) Integrated PL intensity. The PL spectra for low temperature and room temperature are shown in the inset.

One of the predicted advantages of using quantum dots in semiconductor lasers is the temperature-insensitivity of the threshold current [12]. In an ideal quantum dot system with a sufficiently large level spacing, the distribution of carriers remains unaffected by temperature and carriers are not "lost" to non-lasing states. In reality, however, quantum dots lasers have shown rather poor temperature characteristics at room temperature, mainly due to temperature-dependent carrier recombination in the barrier material, arising from a high density of native defects [121]. The increased defect density in the barrier results from the low substrate temperatures necessary for growing the dots. Several ways have been suggested to improve the temperature stability, including thermal annealing [122] or hydrogen passivation [123] of defects, as well as direct tunneling injection into the dots [124]. Thermal annealing has been reported to yield higher luminescence intensity at room temperature than at low temperature [125] and close to ideal threshold current and internal quantum efficiency in quantum dot lasers [122].

Thermal annealing at temperatures that are sufficiently high to repair growth-induced crystal defects inevitably result in diffusion of indium through the crystal. Diffusion of indium out of the dots smoothens the confinement potential, blue-shifting and narrowing the ground-state PL peak and reducing the spacing of excited states [126, 127, 128, 129]. Post-growth annealing was carried out on the $In_{0.5}Ga_{0.5}As$ quantum dot samples studied here, to examine the viability of tuning the room-temperature emission wavelength to 980 nm for laser applications. The samples were capped with 150 nm of SiO_2 to reduce out-diffusion of As and annealed in N_2 ambient. Fig. 35 shows the results of annealing experiments. The QD ground-state emission is shifted to higher energy and the inhomogeneous broadening is reduced. The wetting layer also shifts to higher energy due to In

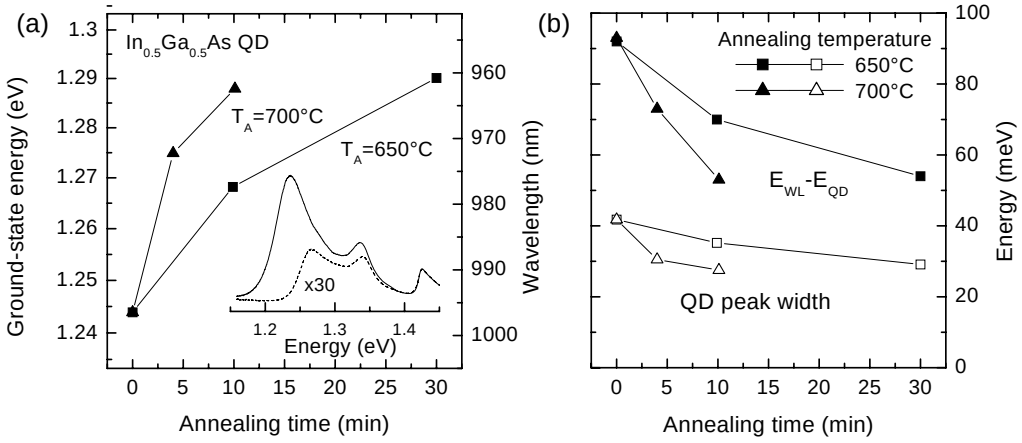

Figure 35: (a) Effect of rapid thermal annealing on the position of the ground-state luminescence peak at room temperature. The inset shows the PL spectra before (solid line) and after (dashed line) annealing. (b) Reduction in energy difference between dot ground states and the wetting layer (solid symbols) and narrowing of the ground state PL peak, measured at 10 K (open symbols).

interdiffusion but by a smaller amount. The effect of annealing for 10 min at 700°C is nearly equivalent to annealing 30 min at 650°C, implying that the indium diffusion length $l_D = \sqrt{4Dt}$ is similar in these two cases ($D = D_0 \exp[-E_d/kT]$ is the diffusion constant of In). This gives an activation energy for diffusion, $E_d \approx 1.7$ eV, which agrees reasonably with activation energies measured using other methods [130]. Even with glass covering the sample surface, significant out-diffusion of As takes place during the annealing, resulting in a drop in PL intensity at room temperature (the PL intensity at 10 K remained unaffected). In order to prevent As out-diffusion and improve the barrier structure, the samples must be annealed under As overpressure, e.g. in the growth chamber.

5.1.3 Energy level structure

At low excitation intensity and low temperature, only luminescence from the quantum dot ground states and the barriers is observed, indicating fast carrier relaxation from the wetting layer and within the dots. At high excitation intensity, however, the population of quantum dot states can be saturated. The Pauli exclusion principle prohibits carriers from relaxing to occupied states at lower energy and, as a result, PL emission from the higher-lying states can be observed. In dots where the level splitting is sufficiently large, compared to the inhomogeneous broadening of the ensemble, high-intensity excitation can be used to determine the position of the excited states of the localized excitons. Fig. 36 shows the excitation power dependence of the PL from two quantum dot samples. A micro-PL configuration with a slightly defocused laser spot was used to obtain high

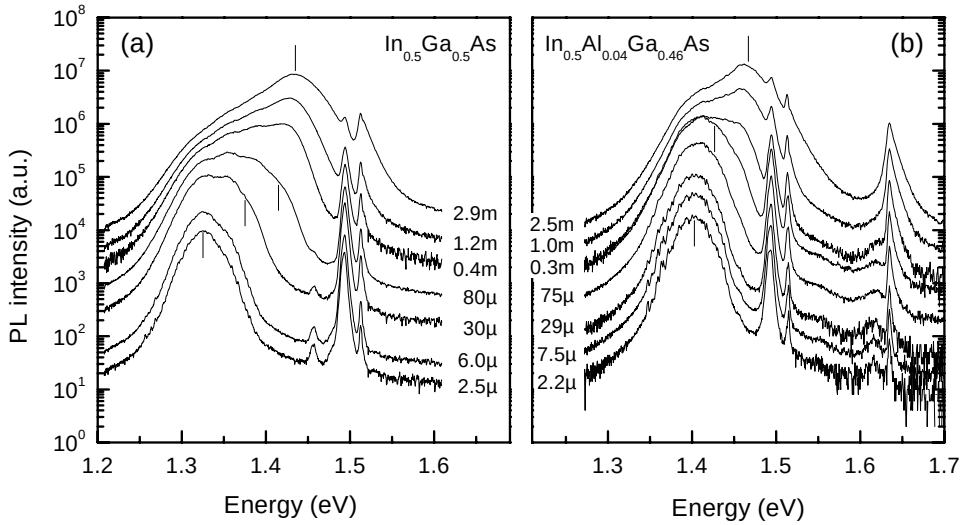

Figure 36: State-filling spectroscopy on (a) InGaAs and (b) InAlGaAs quantum dots. The positions of the wetting layer transition and the excited dot levels, determined from PLE measurements, are indicated with vertical lines. The excitation power (in W) is indicated (excitation spot size $\approx 1\,\mu$m).

excitation intensities, corresponding to approximately 100 kW/cm^2 for the highest powers used here. The level splitting is not sufficient to resolve the excited-state structure but the maximum of the PL spectrum at the highest excitation power corresponds well to the wetting layer position determined from photoluminescence excitation spectroscopy, shown in Fig. 37.

Macroscopic PLE spectra were measured by exciting the samples with a tunable Ti:sapphire laser and recording the full PL spectrum for different excitation energies. Representative cuts, integrated over a narrow interval of detection energies, are shown in Fig. 37. For the InGaAs dots (Fig. 37a), the PLE signal shows a peak, labeled E_1, which occurs approximately 50 meV above the detection energy, irrespective of which part of the PL peak is detected. For low detection energies, a second peak E_2 is visible at $E_{\mathrm{det}} + 90$ meV. The third peak appears at 1.44 eV, independent of detection energy, and can be attributed to the wetting layer exciton transition. Similarly, a peak E_1 is seen in the InAlGaAs dots (Fig. 37b), approximately 22 meV above the detection energy. A PLE enhancement due to optical-phonon relaxation to the detection energy is also observed. Strong LO-phonon relaxation can also be observed in resonantly excited PL spectra, as discussed in the following section. No further excited states are resolved in the PLE spectrum but a wetting layer transition appears at around 1.47 eV. The wetting layer transition occurs 80 meV below the GaAs barrier in the InGaAs dots, but 170 meV below the AlGaAs barrier in the InAlGaAs dots. Calculations (identical to those discussed in Sec. 2.4.2) indicate a wetting layer thickness of 5 ML for the latter case. The average

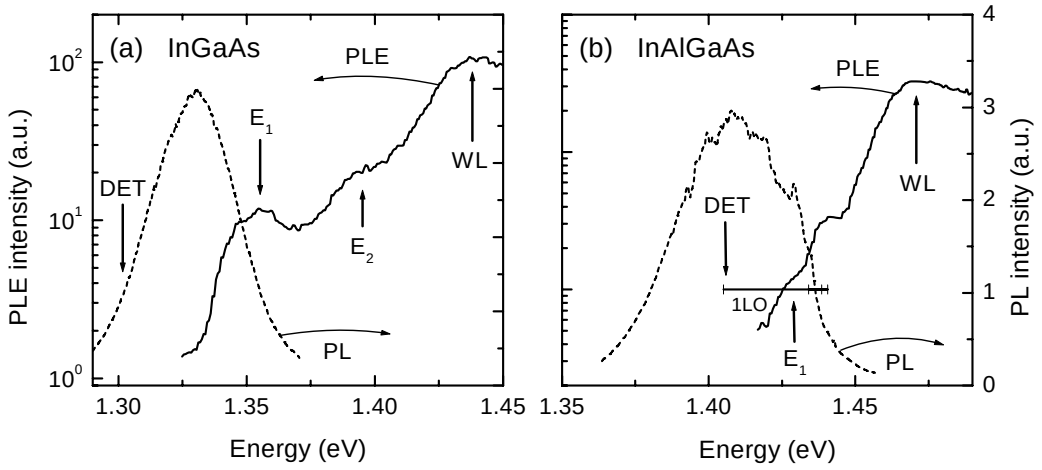

Figure 37: PL (dashed lines) and PLE spectra (solid lines) from (a) InGaAs and (b) InAlGaAs quantum dots. Positions of excited dot states (E_n) and the wetting layer (WL) are indicated. Bulk LO-phonon energies in the InAlGaAs dots are also shown as horizontal bars.

energy difference from the quantum dot ground state to the wetting layer is 105 meV in the InGaAs dots and 55 meV in the InAlGaAs dots. From these observations, it can be concluded that the wave functions of excitons confined to InAlGaAs dots have a larger lateral size (smaller excited-state splitting) and a weaker lateral confinement (smaller energy difference between ground-state and wetting layer) than wave functions of excitons in InGaAs dots.

5.1.4 Time-resolved photoluminescence

Photoluminescence lifetimes in InAlGaAs quantum dots were measured using pulsed resonant and non-resonant excitation and a streak camera for detection. In the non-resonant case, the carrier dynamics is complicated, involving many relaxation channels with different time constants (see e.g. Refs. [131, 132, 133]). For resonant excitation at low temperature, the situation is somewhat simpler since population transfer to or from higher energy states can be ruled out. Fig. 38a shows time-integrated PL spectra obtained using pulsed non-resonant and resonant excitation of a sample containing 10 layers of quantum dots. The non-resonant spectrum shows the typical Gaussian distribution and a strong signal around 1.48 eV, originating from long-lived impurity-bound exciton states in the GaAs substrate. PL spectra for three different excitation energies resonant with different parts of the QD ensemble are also shown. The main peak in each spectrum corresponds to resonantly enhanced secondary emission at the excitation energy. This peak also has a tail to the low-energy side due to acoustic phonon emission.

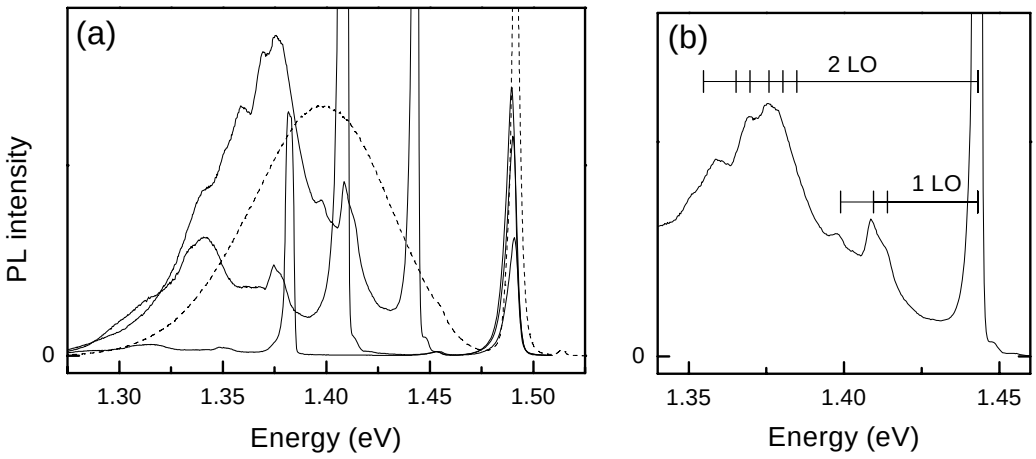

Figure 38: (a) PL spectra excited resonantly (solid lines) and non-resonantly (dashed line) using pulsed excitation. (b) One of the resonantly excited PL spectra, illustrating the phonon relaxation. Bulk LO-phonon energies of the dot material and two-phonon combinations are shown as horizontal bars.

Significant carrier relaxation also occurs by emission of LO phonons. One of the resonantly excited spectra is shown in Fig. 38b, along with the LO-phonon energies in the dots. Contributions from the InAs-like, GaAs-like and even a weak AlAs-like mode are observed. The 6 different two-phonon combinations are also shown. The phonon energies plotted for the InAs-like and GaAs-like modes are bulk values for $In_{0.53}Ga_{0.47}As$ (29.2 meV and 33.6 meV, respectively) [120], confirming that effects of strain and confinement on the LO-phonon energies are small. The energy of the AlAs-like mode in this quaternary alloy has not been previously reported but the value observed here (44.2 meV) agrees closely with that of the AlAs-like mode in $Al_{0.04}Ga_{0.96}As$ [134]. It should be pointed out that relaxation between states with a separation which is not resonant with a particular LO-phonon energy is reduced but not suppressed. Calculations have shown [135], that the phonon confinement results in a coupling with acoustic phonons which broadens the LO-phonon resonance considerably, thus reducing the phonon bottleneck effect. By measuring PLE spectra of individual InGaAs dots, Toda *et al.* [136] also observed a continuum-like density of states above the first excited state of the dots, which facilitates acoustic-phonon relaxation.

PL transients for resonant and non-resonant excitation are plotted in Fig. 39a. The non-resonantly excited PL transients are non-exponential, showing a faster decay for shorter times, corresponding to initial relaxation to lower lying states. The actual inter-level relaxation time, however, is much faster than the initial PL decay time, as indicated by the fast rise of the non-resonant PL. The initial and final decay times converge to a similar value at the low energy side of the QD ensemble, where fewer states are available

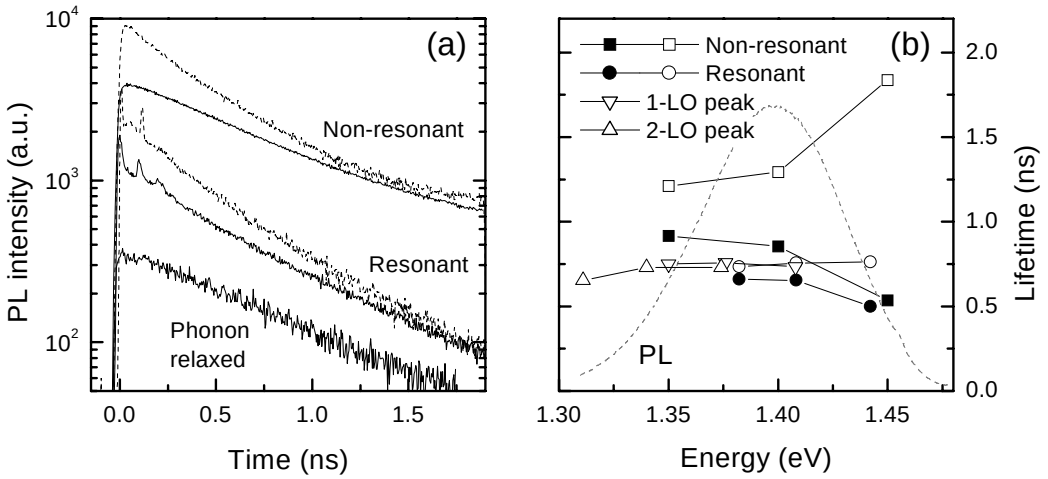

Figure 39: (a) Photoluminescence transients for non-resonant and resonant excitation, measured on the high energy side of the dot distribution (dashed lines) and close to the center of the distribution (solid lines). PL from excitons that have relaxed by LO-phonon emission is also plotted. (b) Decay time for the initial (solid symbols) and final (open symbols) part of the PL decay. The photoluminescence spectrum is shown for reference.

for relaxation. Decay times derived from exponential fits to the initial part of the transients ($t < 0.5\,\mathrm{ns}$) and at the limit of the measurement range ($t > 1.5\,\mathrm{ns}$) are shown in Fig. 39b. Slower PL decay is observed in the non-resonant case, consistent with carrier relaxation from higher-lying states.

Resonantly excited PL transients also show a slightly faster decay for short times but eventually reach a decay time of about 750 ps. A similar lifetime is obtained from PL transients corresponding to the LO-phonon peaks in Fig. 38 which invariably show a fast rise and monoexponential decay over the full measurement range. Similar decay times have been observed for InAs/GaAs quantum dots under resonant excitation, and shown to be independent of temperature up to about 50 K, while at higher temperatures, the lifetime increases sharply [137]. This behavior has been attributed to a non-radiative recombination channel which is active at low temperatures [138]. Although the state lifetime measured in resonant PL at low temperature presumably does not represent the true radiative lifetime of the exciton, it is nevertheless an important parameter for analyzing the homogeneous linewidth of quantum dot transitions, discussed in the following sections. From the above data is can be concluded that the population lifetime contribution to the FWHM homogeneous linewidth is $\hbar/(750\,\mathrm{ps}) = 0.9\,\mu\mathrm{eV}$.

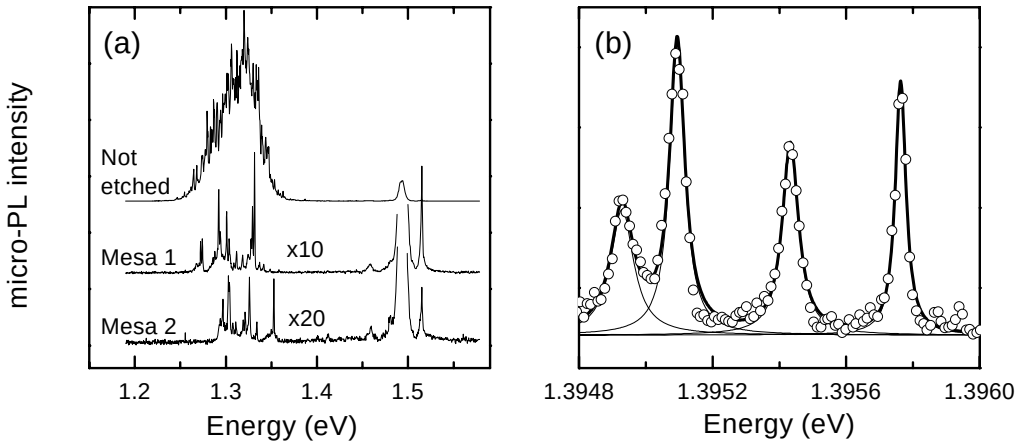

Figure 40: (a) 10-K photoluminescence spectra from etched mesas containing a limited number of InGaAs quantum dots. A micro-PL spectrum from an unetched area is shown for comparison. (b) Spectrally resolved emission lines from single InAlGaAs quantum dots. The solid lines represent Lorentzian peak fits.

5.2 Microphotoluminescence of quantum dots

5.2.1 Single-dot luminescence

In order to resolve emission from individual quantum dots, the detection area was reduced by mesa ething or metal masking. Fig. 40a shows micro-PL spectra of InGaAs quantum dots, collected from an unprocessed area of the sample, and from two etched mesas. Etched mesas showed a poor luminescence efficiency at high temperature, and were found to deteriorate over time. Metal masking was therefore used primarily as a way of improving the spatial resolution, without disturbing the local environment of the dots. When emission from patterned samples is measured with a high spectral resolution, individual PL lines are resolved. In many cases, the emission is fairly well described as collection of Lorentzian lines of different widths, as shown for a sample of InAlGaAs quantum dots in Fig. 40b. In reality, however, the situation is more complicated. If the emission line itself is assumed to be Lorentz-broadened then, after convolution with the spectrometer response, it becomes a Voigt function. An additional Gaussian broadening of the emission line occurs if random (and continuous) spectral fluctuations take place on a time scale shorter than the integration times used in the PL experiment. In this case, the measured line also has a Voigt profile, with an additional Gaussian contribution. Furthermore, the observed lineshape at low temperature is often slightly asymmetric, with a tail on the low energy side, which can be attributed to acoustic phonon emission [139].

Micro-PL spectra measured with different excitation intensities are plotted in Fig. 41. With increasing excitation power, the intensity of individual PL lines grows linearly, up

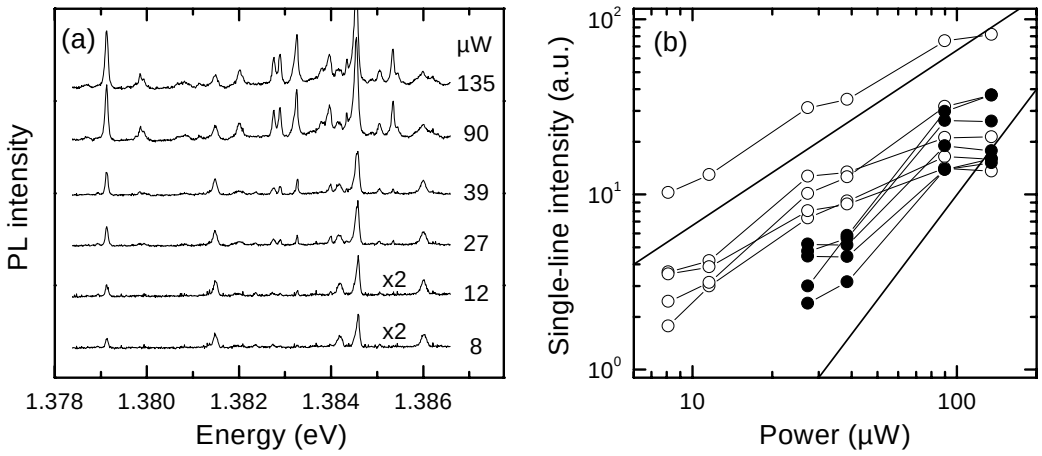

Figure 41: (a) Micro-PL spectra corresponding to different exciation powers. (b) Integrated intensities of individual emission lines. The solid lines follow a linear and quadradic dependence on excitation power.

to a point where the PL intensity saturates due to state filling and eventually decreases. Additional lines also appear, increasing in intensity as the square of the incident power. The latter group of lines are attributed to biexciton emission. Biexciton binding energies of 2–3 meV have been reported in InGaAs/GaAs and InAs/AlGaAs quantum dots [140, 141]. Eventually, the spectrum becomes a complicated collection of multi-exciton emission lines. Detailed studies of multi-exciton luminescence from single self-assembled quantum dots can be found in the literature (see, e.g., [109, 140, 141, 142, 143]) and no attempt was made here to correlate different emission lines to specific dots. All PL experiments discussed below were carried out in the linear regime.

The histogram in Fig. 42a shows the distribution of linewidths in InGaAs and InAlGaAs quantum dot samples. A broad range of PL linewidths is observed in both types of dots, with most typical linewidths being around 40–60 μeV in InGaAs dots, and 60–80 μ in InAlGaAs. These values are obtained before correcting for the response of the spectrometer which has a slightly better resolution at the longer wavelength of the InGaAs dots ($\approx$ 18 μeV FWHM at 940 nm versus $\approx$ 23 μeV at 886 nm). The linewidth shows no systematic dependence on energy within the quantum dot ensemble, as shown in the inset. Measurement artifacts, such as inaccuracies in the fitting procedure (see Sec. 3.2.2) and accidental overlapping of lines cannot account for the range of linewidths observed here. It should also be noted that broader lines ($>$ 100 μeV) deviate significantly from Lorentzian shape and are better described as Gaussian. Intensity-dependent measurements (Fig. 42b) reveal that the width of all lines increases with excitation power, by about 10–20 μeV/decade for narrower lines and up to ten times faster for broader lines. Although the power dependence is much weaker ($w \propto P^{0.1}$–$P^{0.2}$) than the linear excita-

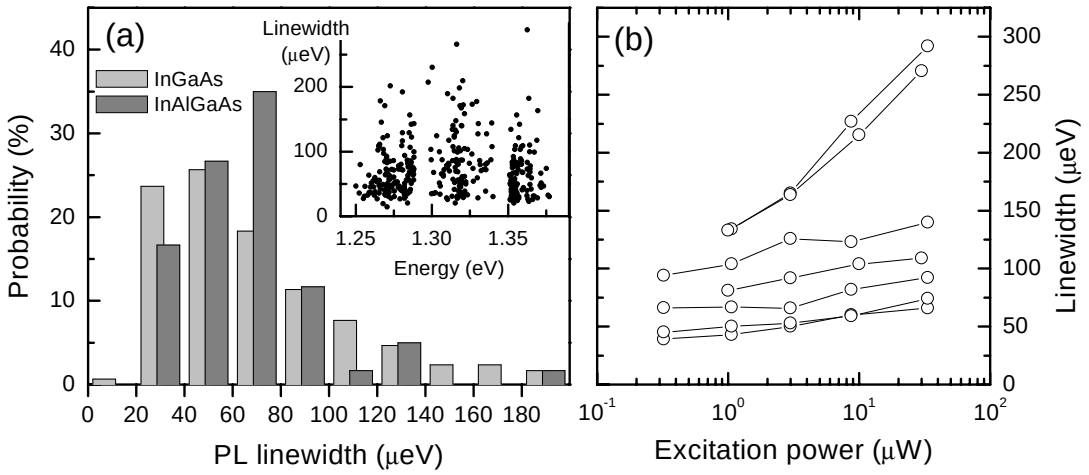

Figure 42: (a) Linewidth statistics for two quantum dot samples. The PL was measured at 10 K, using 1 μW of 632.8-nm excitation. The inset shows the energy distribution of linewidths for the InGaAs quantum dot sample. (b) Intensity dependence of the linewidth for different lines within the distribution.

tion dependence of the homogeneous linewidth observed, e.g., in InGaAs quantum wells [144], it confirms that excitation-dependent effects are partly responsible for the measured linewidth distribution. PL linewidths in the range 30–60 μeV have been observed previously in different self-assembled quantum dot systems [145, 146, 147] and (incorrectly) assumed to represent the homogeneous linewidth.

Recent studies of PL emission from single self-assembled III-V [148, 149] and II-VI [150, 151, 152] quantum dots have revealed large (1–3 meV) fluctuations in the spectral position of single emission lines. In general, these have been attributed to the presence of fluctuating local electric fields. An electric field in the material results in a bending of the conduction and valence bands which reduces the separation of the confined electron and hole energy levels in the dots, an effect referred to as the *quantum-confined Stark effect* [22, 23]. Different sources of the electric field fluctuations have been suggested. Fast spectral fluctuations contributing to strong line broadening in self-assembled InP dots were attributed to trapping of weakly bound charges at nearby localization centers in the wetting layer [148]. The effect disappeared at temperatures above 40 K, when the weakly bound charges were thermally excited. Discrete spectral shifts were observed in real-time on a time scale of minutes in $In_{0.55}Ga_{0.45}As/Al_{0.35}Ga_{0.65}As$ dots [149]. In the latter case, spectral fluctuations were found to be absent at low excitation power. A similar sample ($In_{0.5}Ga_{0.5}As/Al_{0.35}Ga_{0.65}As$) grown for the present study also showed discrete spectral shifts and blinking in single-dot emission, while no such behavior was observed for dots with lower Al content in the barrier. This suggests that variations in the charge state of nearby deep defects, related to the high Al concentration [134, 153], could be responsible

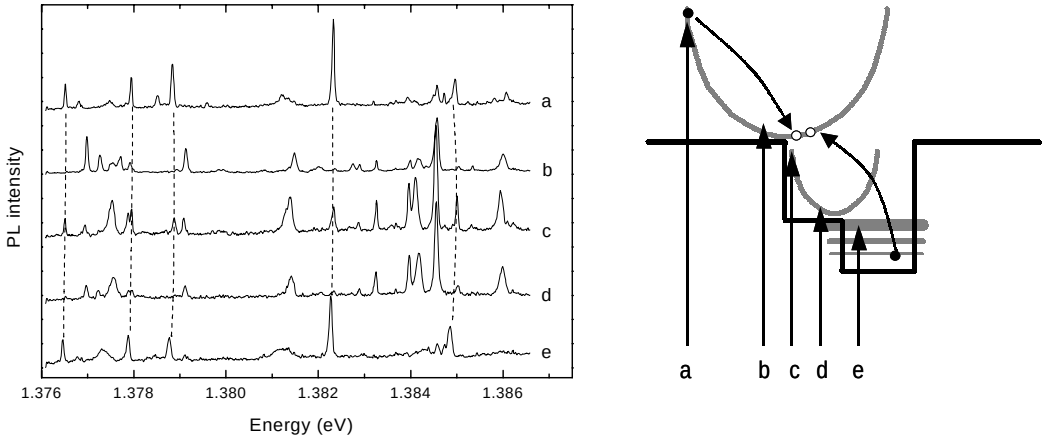

Figure 43: Micro-photoluminescence spectra of InAlGaAs quantum dots for different excitation energies. The excitation energies are indicated schematically on the band diagram, which also illustrates a possible Auger scattering process between electrons in the dots and in the barrier.

for spectral fluctuations in the single-dot emission. Based on results from excitation-energy-dependent PL measurements and four-wave mixing experiments presented below, it can be concluded that the linewidth distribution shown in Fig. 42 arises mainly from local field fluctuations, occurring on time scales below 1 s, i.e. faster than can be detected with the present experimental setup. The amplitude of these fluctuations is two orders of magnitude smaller than those discussed in the above-mentioned reports, and could arise from changes in the charge state of neighboring dots, roughness-induced localization in the wetting layer, or trapping of charges at defects centers. The linewidth broadening could also be related to the presence of the built-in electric field (see below). By comparing with the Stark shifts observed for single quantum dots in transverse [154] and lateral [155] fields, it can be estimated that a 10 μeV shift in the line position can be caused by a single electron or hole placed 50–75 nm away from the dot, which agrees with a typical distance between dots.

5.2.2 Dependence on excitation energy

Micro-PL spectra of small ensembles of quantum dots exhibit a significant dependence on excitation wavelength, as shown for InAlGaAs dots in Fig. 43a. The different spectra correspond to excitation in the barrier, wetting layer or directly in the excited states of the dots. The excitation wavelengths used are indicated on the energy band diagram of Fig. 43b and labeled (a)–(e). In order to compensate for the decreased absorption, the excitation intensity for wavelengths (b)-(e) was progressively increased to keep the

total PL intensity approximately constant. Single-exciton lines in spectrum (a) are also observed in spectra (c) and (e), while they are nearly absent when excitation takes place close to the band edge of the barrier or the wetting layer (spectra (b) and (d), respectively). In (e), excitation occurs approximately 50 meV above the QD ground state where the line pattern depends only weakly on the precise excitation wavelength due to the high density of excited states. Spectra (b) and (d) share a new set of PL lines, which are also observed in spectrum (c). It should be emphasized, that in (b) and (d) the excitation occurs in the continuum of the barrier and wetting layer, respectively, and not resonant with the band-edge exciton transition.

The above observations can be explained as follows. The PL measured for near-band-edge excitation is attributed to negatively charged excitons, assuming that in equilibrium, the dots contain electrons from residual donors in the MBE-grown material. In InAs quantum dots, excitation above the barrier band edge has also been reported to result in an increased population of charged exciton states, the appearance of which is anticorrelated with neutral exciton states [141]. The absence of charged exciton luminescence at excitation energies away from the band edge, on the other hand, can be attributed to Auger scattering between free non-equilibrium carriers generated by the optical excitation and confined electrons in the dots. Such a process is shown schematically in the band diagram of Fig. 43b. Dots occupied by (neutral) excitons are not strongly affected by this scattering mechanism, due to the smaller carrier-exciton Coulomb interaction. Spectrum (c) represents an intermediate situation, where single-exciton PL is observed but the energy of excited carriers is not sufficient to completely remove excess charge from the dots. Similar effects were also observed in InGaAs/GaAs dots, where charged-exciton lines dominated the micro-PL spectra for excitation up to 200-300 meV above the barrier band edge but decreased rapidly in intensity for higher excitation energy. Charged exciton lines were not present in the spectra under He-Ne excitation (440 meV above the band edge).

Changing the excitation wavelength also affects the position and linewidth of single-dot emission lines. The change in position can be attributed to a photo-induced screening of the built-in electric field. The electric field induced by the surface potential results in a Stark shift in the position of the individual lines. Continuous illumination above the barrier bandgap induces a steady-state carrier concentration in the depletion region, which screens the built-in electric field and reduces the Stark shift. Stark shifts of emission lines from individual self-assembled InAlAs/AlGaAs quantum dots under applied electric field have been reported, amounting to 150–300 μeV [154] at a field strength which equals the estimated built-in electric field for a gold-coated sample (15 kV/cm, see Sec. 3.1.2). In Fig. 44a, a large shift is observed already when changing the excitation wavelength from 531 nm to 633 nm. The direction of the shift is consistent with a reduction in the built-in field at the shorter excitation wavelength. The magnitude of the shift varies between dots due to differences in geometry and amounts to 250–500 μeV for the lines shown here, when comparing excitation directly into the dots and an excitation wavelength of 531 nm. The PL linewidth is also reduced at shorter wavelengths, as demonstrated in Fig. 44b. It is difficult to conclusively identify the reasons for this behavior but possible explanations

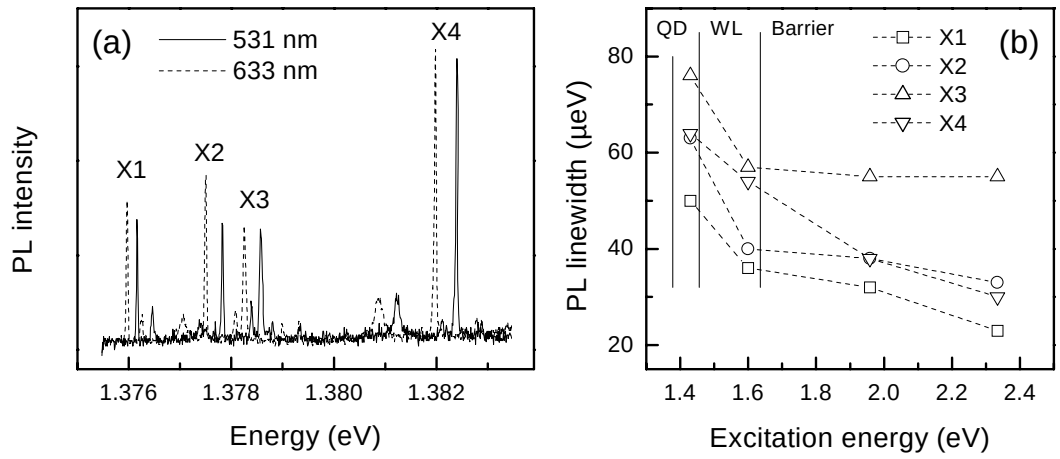

Figure 44: (a) Stark shift of single-dot lines for different excitation wavelengths. (b) Excitation-energy dependence of the single-dot linewidth, plotted for the lines labeled X1–X4 in (a). The lines are not observed at all excitation energies, as explained in the text.

include more efficient scattering of free charges out of the quantum dots and a reduction in the built-in electric field for short wavelengths, as opposed to increased carrier-carrier scattering and/or field fluctuations due to higher local carrier concentrations for resonant excitation into the dots or the wetting layer. At an excitation wavelength of 531 nm, a fraction of the measured lines has a width approaching the resolution limit of the spectrometer. Numerical analysis shows, that these lines can be described with a Voigt profile given by the spectrometer response function with an added Lorentzian broadening of $6 \pm 2\,\mu$eV. Subtracting a lifetime broadening of about $1\,\mu$eV (Sec. 5.1.4), gives a *lower limit* for the pure dephasing time in these quantum dots of $T_2^* = 300 \pm 100$ ps at 10 K. This value is an order of magnitude larger than previous estimates from micro-PL investigations on III-V quantum dots [145, 146, 147] and similar to the T_2^* observed for three-dimensionally localized excitons in growth-interrupted quantum wells (Sec. 4.4).

5.2.3 Temperature dependence

Micro-PL spectra from a small ensemble of InAlGaAs quantum dots in the temperature range 10–90 K are plotted in Fig. 45a. By lining up single-dot features in the spectra, it is possible to accurately determine the shift in bandgap with temperature. As the temperature increases, individual PL lines become broader and the average PL position shifts to lower energy. Single emission lines at the high energy side disappear while the relative intensity of lines on the low-energy side increases. Comparing the measured shift of individual PL lines with the average PL position (Fig. 45b) gives a dependence similar

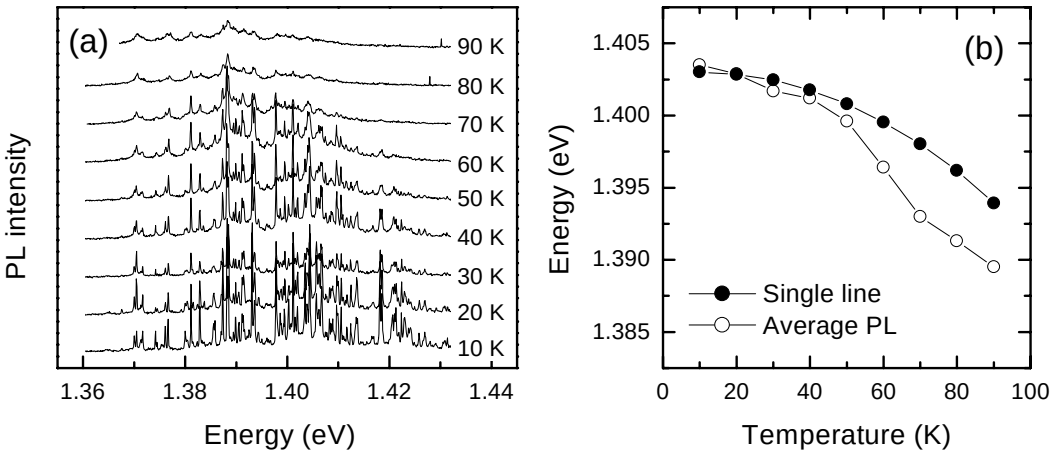

Figure 45: (a) Micro-PL spectra recorded at different temperatures. The spectra have been shifted horizontally to compensate for the change in bandgap and vertically for clarity. (b) The bandgap shift in the dots, determined from the position of individual emission lines (shifted arbitrarily) and the average energy of the total photoluminescence. A clear signature of thermalization is observed above 50 K.

to that observed in macroscopic PL for InGaAs dots (Fig. 34a).

In order to provide more information about the thermalization process, the variation in single-dot linewidth with temperature is plotted in Fig. 46. In addition to significant broadening of the sharp (zero-phonon) PL lines, a broad PL background also appears with increasing temperature, which is attributed to wide acoustic-phonon sidebands in the emission [139, 156]. For both samples, widths of several lines close to the center of the macroscopic PL peak were measured. Dashed lines in Fig. 46b indicate the range of measured linewidths, while data for representative lines are plotted as symbols. The temperature dependence can be divided into three parts, a finite linewidth at zero temperature, a weak linear increase at low temperature ($< 50\,\mathrm{K}$), and a temperature-activated behavior at higher temperature. This general behavior agrees with the recent temperature-dependent four-wave mixing measurements on InGaAs quantum dots [156], as well as PL linewidth data on other III-V quantum dots [146], and on II-VI quantum dots [139]. A function of the form

$$\gamma(T) = \gamma_0 + aT + \frac{b}{\exp(E_a/\mathrm{k}T) - 1} \tag{28}$$

was used to fit the linewidth data. The offset γ_0 includes the lifetime broadening as well as the dot-dependent broadening attributed to local field fluctuations, and will, therefore, depend on temperature. In the fitting procedure, however, γ_0 was assumed to be independent of temperature. This assumption means that any temperature dependence will affect the other fitting parameters. The lifetime contribution is small, however, and expected

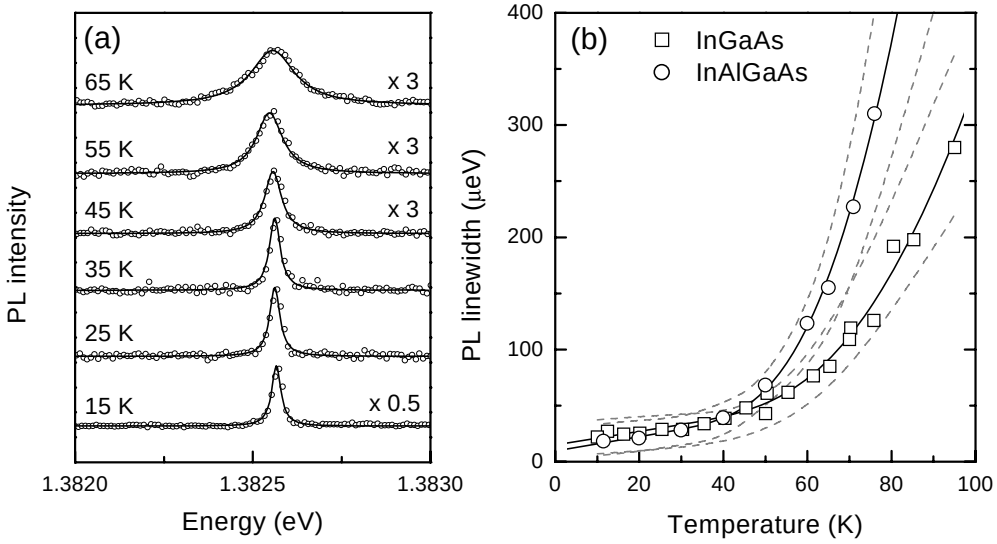

Figure 46: (a) A single InAlGaAs quantum-dot emission line measured at different temperatures, along with Lorentzian fits (solid lines). (b) Temperature dependence of the spectral width of representative lines in two different types of dots. Dashed lines indicate the range of measured linewidths for different emission lines. The solid lines are fits to representative data points, as described in the text.

to decrease with temperature in this range [137, 138]. Some PL lines showed a reduction in linewidth as the temperature was increased from 10 K to 20 K, similar to what was observed for localized excitons in quantum wells (Fig. 30). Otherwise, all lines showed a similar linear increase with temperature below 50 K, suggesting that the difference in low-temperature linewidth does not significantly affect the temperature dependence in this range. The linear part of the temperature dependence has been attributed to inelastic acoustic phonon scattering [139, 156], and to virtual acoustic phonon scattering processes within the exciton ground state [157]. The fit gives $a = 0.5 \pm 0.1\,\mu$eV/K, which is lower than the 1.6–3-μeV/K acoustic phonon scattering coefficient measured in InGaAs quantum wells [144], reflecting the reduced density of states in the dots.

The last term in Eq. (28) describes a phonon-activated contribution to the linewidth, corresponding to scattering between two states separated by an energy E_a, while b reflects the coupling strength. For the InGaAs sample, $E_a = 31 \pm 2$ meV and $b = 9 \pm 3$ meV, while for the InAlGaAs dots, $E_a = 30 \pm 2$ meV and $b = 24 \pm 8$ meV. Remarkably, the activation energies are independent of the exciton confinement, but in good agreement with optical phonon energies in the dots. Furthermore, the coupling parameters are similar to those observed for LO-phonon coupling in InGaAs quantum wells [144]. An enhanced interaction between excitons and LO phonons in strained quantum dots has been predicted and demonstrated experimentally [32]. The stronger coupling observed in the InAlGaAs dots is also consistent with an enhancement of exciton-LO-phonon coupling with increasing lateral dot size which was predicted by calculations but not conclusively demonstrated experimentally [32]. The larger lateral size of the InAlGaAs quantum dots, compared to the InGaAs dots, was inferred from the smaller splitting of the exciton ground state and first excited state in these dots (Fig. 37). It can be concluded, that the rapid increase in the single-dot linewidth above 50 K is a result of strong coupling between excitons in the ground states of the dots and LO phonons.

Since the LO-phonon increase in linewidth coincides with the thermalization in the quantum dot ensemble, it can also be concluded that carriers are ejected from the dots into the wetting layer within the exciton lifetime. From there, they can subsequently be captured by other dots and reach thermal equilibrium. For InAlGaAs quantum dots close to the center of the inhomogeneous distribution, it requires about 60 meV to remove an exciton from the dot and dissociate it in the wetting layer. The energy of a single LO phonon (≈ 30 meV) is therefore sufficient to eject *either* electrons or holes from the dots, depending on the difference in confinement in the conduction and valence bands, and provided that this difference is larger than the exciton binding energy in the dots (E_B). In InGaAs dots, however, the corresponding dissociation energy is close to 110 meV, and the difference in confinement energy must therefore be close to 50 meV+E_B. Model calculations presented in Sec. 2.4.2 indicated an energy difference of 70 meV between the lowest hole level in the dots and the hole level in the wetting layer. However, the calculation overestimated the total energy for removing an exciton from the dot by a factor of 2, as demonstrated in Sec. 5.1.3. Combined with the rather large valence band offset used in the calculation (compared to, e.g., Refs. [158, 159, 160]), it is plausible to

assume that the LO-phonon energy is sufficient to eject holes from the quantum dots to the wetting layer in both types of dots studied here. Ground-state electrons are presumably not affected because of the stronger confinement in the conduction band.

In Ref. [156], FWM measurements on $In_{0.7}Ga_{0.3}As/GaAs$ quantum dots revealed a non-linear temperature dependence of the homogeneous linewidth with an activation energy of 16 meV. This energy was attributed to acoustic-phonon scattering to the first excited hole state in the dots. In this case, it is likely that a single LO-phonon energy is insufficient to eject carriers from the dot ground states into the wetting layer, since the confinement is about twice as strong as in the case of $In_{0.5}Ga_{0.5}As$ dots. Furthermore, the strength of the LO-phonon coupling might be reduced because of the smaller dot size [32].

5.3 Four-wave mixing in quantum dots

In order to conclusively determine the (ensemble-averaged) homogeneous linewidth of the quantum dots, four-wave mixing measurements were carried out on a 10-layer sample of InAlGaAs dots. Four-wave mixing experiments on self-assembled III-V quantum dots have not been previously reported, except in optical amplifier structures [68, 156], where waveguiding in the quantum dot plane is used to enhance the interaction between the dots and the light field. In a standard experimental geometry, where the propagation of the light is approximately parallel with the growth axis, the absorption of the quantum dots (and, hence, the non-linear signal) is very low. Using the published value of the absorbance in InAs quantum dots [161] it can be estimated that only about 0.5% of the dots are optically excited for each mW of average beam power in the experiments presented here. Measurements were carried out with 10–40 mW (without chopping) in beam 2 and roughly half in beam 1 (the experimental setup is shown in Sec. 3.3.2).

Figure 47 shows an initial attempt at measuring a FWM signal from the quantum dots. The excitation beams were incident from the front side of the sample and the excitation wavelength corresponds to the high-energy side of the quantum dot distribution. A sharp peak is observed in the signal at zero delay and at delay intervals of about 12 ps, which corresponds to the time required for a pulse to travel through the sample and back again after being internally reflected at the back side. Similar signals were observed in a reference sample without quantum dots and are attributed to two-photon absorption in the bulk crystal. In the quantum dot sample, however, a contribution to the FWM signal is observed which is not present in the reference. The FWM response is complicated by the multiple reflections, but for positive delays the time-integrated signal decays with a time constant of about 12 ps, corresponding to $T_2 \approx 48$ ps, under the assumption of a photon echo (Eq. (21)). This assumption is reasonable, even though the laser pulse only excites a subset of the entire quantum dot ensemble, since the spectral width of the laser is still significantly larger than the homogeneous broadening of the dots. It was confirmed that the signal strength increases as the third power of the excitation intensity, as expected for a third-order non-linear process. After optimizing the experimental setup, as described

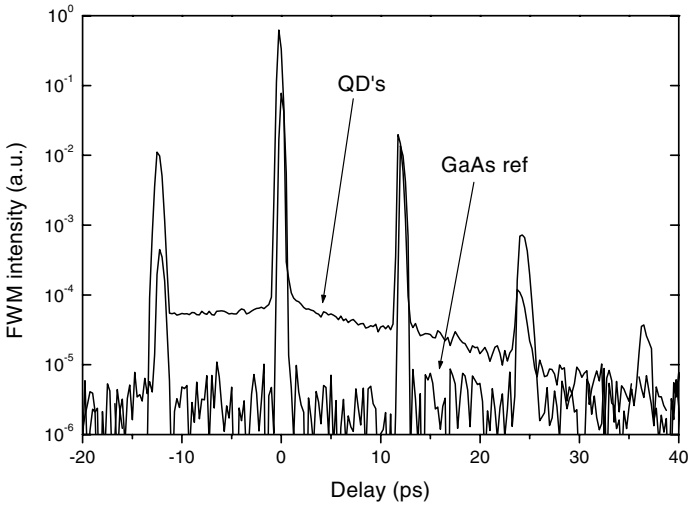

Figure 47: Four-wave mixing signal from a sample containing InAlGaAs quantum dots, and from a reference sample without dots. The strong peaks are due to multiple reflections of excitation pulses inside the sample which is transparent at the excitation wavelength ($\lambda \approx 860\,\mathrm{nm}$).

in Sec. 3.3.2, and anti-reflection coating the back side of the sample to avoid internal reflections, the signal was improved considerably and an additional component in the FWM response with a much longer decay time was observed, as shown below.

5.3.1 Detuning dependence

The optimized four-wave mixing signal from InAlGaAs quantum dots is plotted in Fig. 48 for different values of detuning of the laser relative to the quantum dot peak. At the high-energy side of the QD ensemble, the signal consists of an initial rapidly decaying component and a weaker component with a significantly longer decay time. As the excitation energy is tuned closer to the center of the dot distribution, the fast component decreases in intensity and eventually disappears, leaving only the slow decay. Similar behavior was observed in FWM measurements on self-assembled CdSe/ZnSe quantum dots [63]. The delay-dependence of the FWM signal at different excitation energies was fitted with double exponential decay curves. The fitted values of the signal amplitudes corresponding to the two components of the FWM response are shown in Fig. 49. The amplitude of the slow part peaks around 1.4 eV, while the fast part increases in intensity up to the wetting layer transition energy around 1.47 eV. A comparison with state-filling experiments (on a single-layer sample) presented in Sec. 5.1.3 reveals a correspondence between the distribution of ground states and the intensity of the slow FWM response on one hand, and between the density of excited states and the fast response on the other

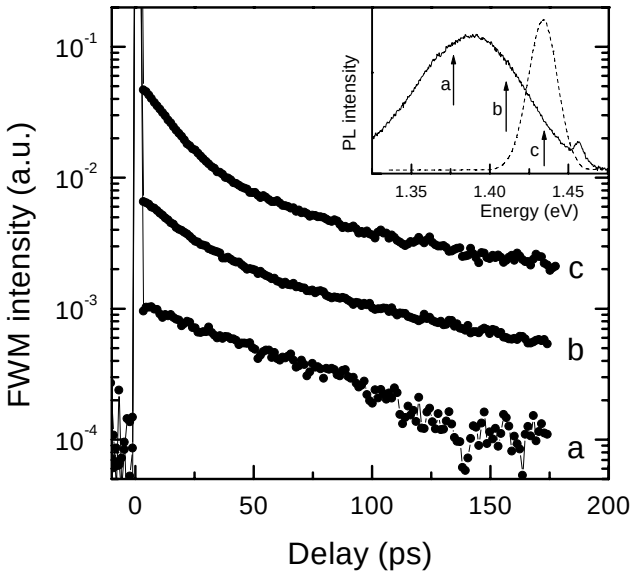

Figure 48: Four-wave mixing signals for different excitation energies within the quantum dot ensemble (shifted for clarity). The different excitation positions are indicated on the PL spectrum in the inset along with the spectrum of the laser pulse.

hand (see Fig. 49). It is therefore natural to associate the slow decay with excitons localized in ground states of the quantum dots, which can not relax to lower-lying states, while the fast response is attributed to excited states, where the state density is higher and relaxation to lower-lying states is possible.

The T_2 time for the fast FWM component decreases from about 80 ps at the center of the QD distribution to below 20 ps as the energy approaches the wetting layer transition. The excited-state population lifetime (T_1) is known to decrease rapidly for excited dot states close to the wetting layer [162] but can only partly account for the observed total dephasing. The decay time of the fast FWM component is presumably affected by scattering within the excited states, although it does not vary significantly with temperature (see below) or excitation intensity (within the experimentally obtainable range). The decay time for the slow component is also independent of excitation intensity (within the experimental accuracy) and has a value of 93 ± 30 ps. No systematic dependence on detuning is observed, primarily due to a large scatter in the data [163]. The total dephasing time of the ground state is therefore 370 ± 120 ps, which amounts to a homogeneous linewidth of only $3.5 \pm 1\,\mu$eV (at 5 K). Subtracting the 1-μeV population lifetime contribution gives a pure dephasing time $T_2^* = 0.5 \pm 0.2$ ns which is among the longest exciton coherence times measured in semiconductor systems [164].

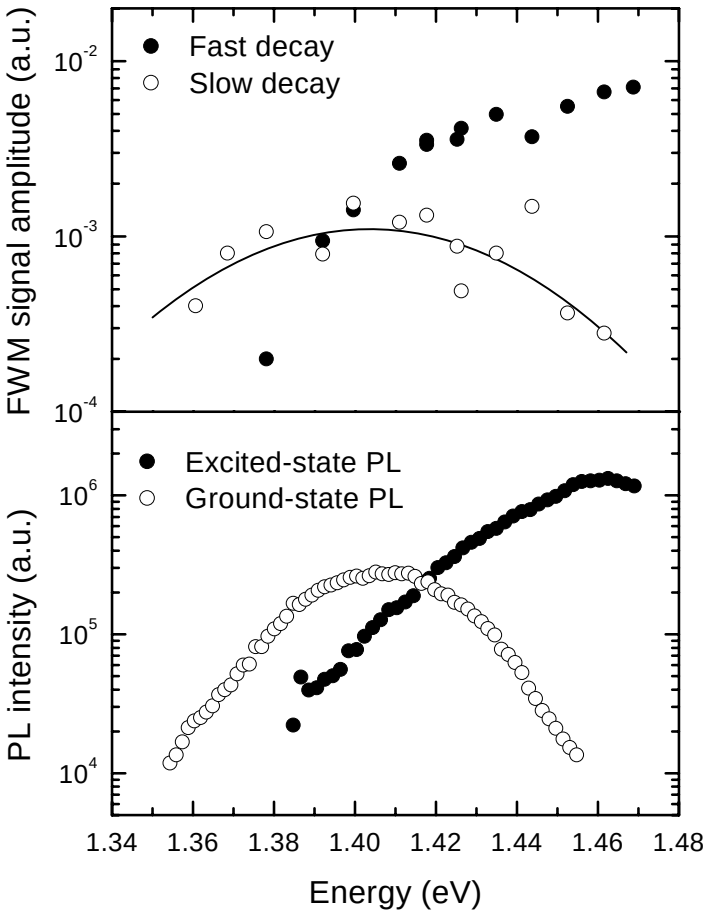

Figure 49: Amplitudes of the two components to the FWM response (upper graph), determined from double exponential fits. The solid line is a Gaussian fit to the amplitude of the slowly decaying part. The lower graph shows PL spectra recorded at low excitation power, corresponding to emission from ground states (open circles) and at high excitation power (solid circles), with the ground-state contribution subtracted, corresponding to PL from excited states only.

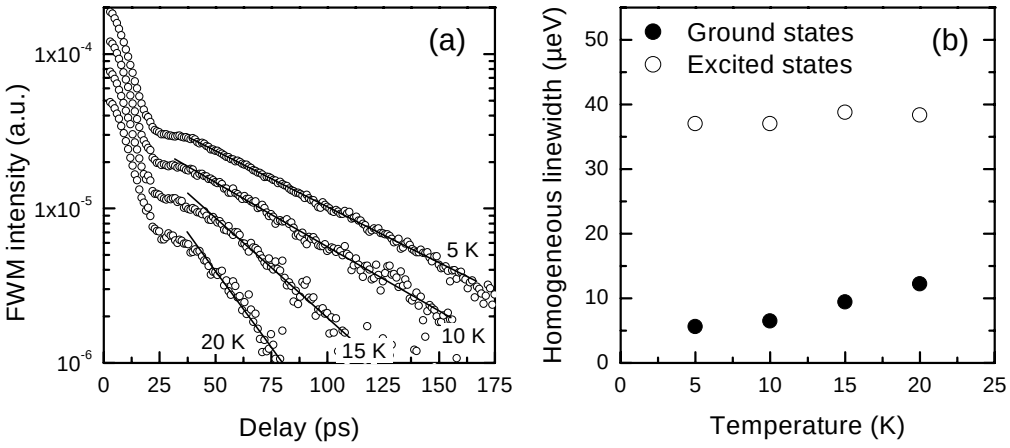

Figure 50: (a) Four-wave mixing response of InAlGaAs quantum dots at different temperatures. Exponential fits to the slowly decaying part are shown as solid lines. (b) Homogeneous linewidth corresponding to the fast (open circles) and slow (solid circles) FWM decay, attributed to excited states and ground states of the dots, respectively.

5.3.2 Temperature dependence

The FWM signal strength decreases rapidly with increasing temperature and measurements above 20 K did not yield reliable results. The temperature dependence of the FWM response between 5 K and 20 K is shown in Fig. 50, for excitation on the high-energy side of the QD ensemble. As before, the decay is characterized by a fast and a slow component, although the FWM decay curves look distinctly different in this case. The FWM traces in Fig. 50a are recorded at a different position on the sample and with a slightly different experimental arrangement than those shown in Fig. 48. The reason for the differences in the signal is unclear. The measured decay times are also shorter, corresponding to a homogeneous linewidth of 5.5 μeV and 37 μeV at 5 K for the slow and the fast decay, respectively. At 10 K, the homogeneous linewidth is 6.5 μeV, which agrees with the width of the narrowest single-dot emission lines observed in the micro-PL spectra at this temperature, as discussed above. Furthermore, the homogeneous linewidth determined by FWM increases by about 0.5 μeV/K above 10 K, in accordance with measurements of the PL linewidth. From this data, it is not possible to determine whether the homogeneous linewidth of the quantum dot ground state extrapolates to the 1-μeV limit imposed by the population lifetime or whether a component of pure dephasing remains at 0 K, as suggested, e.g., in Ref. [165]. Additional measurements below 5 K are required to conclusively answer this question. In addition, the origin of the homogeneous linewidth of the excited state transitions and its independence on temperature, warrant further investigation.

A comparison between the above results and those on excitons localized in quan-

tum wells (Sec. 4.4), indicates that the more strongly confined excitons in self-assembled quantum dots show a longer pure dephasing time (T_2^*) that is less sensitive to excitation and temperature effects, although the differences are not striking. There is, however, a dramatic difference in the state lifetime and, consequently, in the total dephasing time (T_2) in these two systems. Following the arguments of Citrin [166], the commonly observed increase in exciton lifetime with increased confinement has been explained by the momentum uncertainty resulting from the spatial localization, often referred to as the spatial coherence effect. Even though the electron and hole wavefunction overlap in real space increases, the localized exciton has a larger spectrum of k-vectors and its overlap with radiative modes (around $k = 0$) is reduced. The particular nature of the confinement in strain-induced quantum dots, which results in an decreased electron-hole overlap [32], also enhances the exciton lifetime. In self-assembled quantum dots, the combination of a long ground-state lifetime, fast interdot relaxation, and large homogeneous broadening at elevated temperatures (all factors resulting from the non-ideal nature of the quantum dots) makes them attractive for application in semiconductor lasers while the low modal gain resulting from their small active volume remains as one of the main drawbacks.

6 Summary and conclusions

In this thesis, different optical signatures of exciton localization in semiconductor nanostructures have been presented and discussed, ranging from modifications of optical density spectra in continuously grown quantum wells with microrough interfaces, to sharp emission lines and increased coherence lifetimes in self-assembled quantum dots. Some of the underlying physical processes were outlined, including the basic properties of excitons in semiconductors, their coherence properties and interactions with the environment. Different semiconductor heterostructures that provide three-dimensional confinement of the exciton wave function were described, with particular emphasis on self-ordered nanostructures. It was shown how different length scales of interface roughness can be realized in quantum wells through growth interruption. A structural investigation of strain-induced growth islands was also presented, demonstrating the possibility of fabricating well defined quantum dots for stronger exciton localization using standard MBE growth techniques. Simple models of the electronic structure of disordered quantum wells and strained quantum dots were sketched, since accurate theoretical descriptions are beyond the scope of this work.

Experimental apparatus for measuring photoluminescence with high spatial and spectral resolution was constructed in order to optically probe individually localized excitons. The applicability of the technique was tested on several localized exciton systems. In order to improve the spatial resolution beyond the far-field limit, quantum dot samples were patterned using electron-beam lithography. Metal masks with sub-micron-sized apertures were found to be preferable over etched mesa structures, since metal masking introduces only minor modifications of the local environment of the dot. Although the resolution of the present lift-off process is not sufficient to spatially isolate single quantum dots, the number of dots within the detection area was reduced sufficiently so that PL emission from individual dots was easily separated spectrally.

The spectral resolution of the detection system was analyzed, showing considerable wavelength dependence due to the imaging properties of the spectrometer. The spectrometer response was identified as a Voigt function, and the effect of measuring spectral lines of different shapes was discussed. Spectral lineshape analysis was also discussed as a method of determining the coherence time of localized excitons. Two other techniques of measuring coherence times were described; standard four-wave mixing and the more novel method of speckle analysis, which can be used to directly evaluate the transverse exciton relaxation time.

Quantum wells with different length scales of interface roughness were investigated. It was demonstrated that atomically smooth growth islands are formed on AlAs and GaAs surfaces following growth interruption. A degree of microroughness always occurs at quantum well interfaces, however, due to surface segregation of atoms during overgrowth. A bimodal (or multimodal) interface roughness is thus unavoidable when atomically smooth islands, extending laterally over many lattice constants, are formed during growth. Furthermore, the segregation modifies the shape of the potential well, causing a blue-shift of transition energies that depends on the segregation length and, therefore, on the growth temperature.

If MBE growth is interrupted at both quantum well interfaces, the resulting length scale of potential fluctuations is sufficiently large (compared to the exciton localization length) to result in a monolayer splitting of the exciton density of states. Variations in the position of ML peaks and observation of sub-ML splitting in macroscopic photoluminescence spectra of growth-interrupted quantum wells can be attributed to exciton localization at potential fluctuations with lateral sizes exceeding the localization length, as well as segregation-induced microroughness on the growth islands. Reproducible monolayer peak positions in similarly grown samples can, however, be obtained by measuring quantum wells of continuously varying thickness at temperatures where weakly bound excitons are thermally excited.

Exciton localization in disordered quantum wells was demonstrated directly by spatially resolved micro-photoluminescence imaging and individual emission lines were measured with high spectral resolution. The PL linewidth analysis was complemented by a study of secondary emission from localized excitons at low temperature. By analyzing the coherence of the secondary emission, it was confirmed that the localized excitons exhibited substantially longer T_2^* times than commonly observed in quantum wells. The population lifetime contribution to the linewidth, and hence to the total dephasing time, was shown to be approximately twice as large (at 5 K). Anomalously increased photoluminescence linewidth was observed at low temperatures (< 20 K) and attributed to fluctuating local electric fields due to charges trapped at shallow localization centers. It should be recognized, that the PL linewidth only provides an upper limit of the homogeneous linewidth of the system and care should be taken when interpreting results from PL measurements in terms of dephasing times, especially at low temperatures.

Studies of localized excitons in self-assembled quantum dots were also presented. Basic optical properties of different quantum dot samples were determined, focusing on dots based on ternary and quaternary (In,Ga,Al)As alloys. The effect of post-growth annealing was investigated, demonstrating that the emission wavelength of the dots can be tuned to shorter wavelengths and their inhomogeneous linewidth reduced, at the expense of reducing the strength of the confinement. The dot formation and the energy level structure of the dots was shown to vary strongly with composition. A small fraction of Al in the dots is sufficient to slow down dot formation, resulting in flatter islands on a thicker wetting layer, when compared to dots of similar composition but without Al. Resonant photoluminescence measurements revealed that carriers can efficiently relax within the quantum dot ensemble through acoustic and optical phonon emission. A well defined ground state population lifetime was determined from time-resolved photoluminescence transients.

Photoluminescence from individual self-assembled quantum dots was investigated using micro-PL spectrocopy. In particular, the spectral linewidth of single-dot luminescence was studied, including its dependence on temperature and excitation conditions. It was concluded, that the measured low-temperature luminescence linewidth of individual quantum dots results mainly from spectral fluctuations in the position of the PL line, and not from the homogeneous broadening of the excitonic transition. At low temperature (and only under specific excitation conditions) only a fraction of the dots exhibit emission lines approaching the homogeneous linewidth. Furthermore, the excitation energy was shown to affect the charge state of the dots and thereby the overall ground state of the quantum dot ensemble. The temperature dependence of the photoluminescence and the single-dot PL linewidth indicated a strong interaction between excitons and LO phonons in the dots. It was concluded that the energy level structure in the samples studied here allows for excitation of holes from the dots to the wetting layer through the absorption of one LO phonon. The hole evaporation results in an increased linewidth and thermal redistribution of carriers above 50 K.

Degenerate two-beam four-wave mixing experiments were used to independently determine the (averaged) homogeneous linewidth of the quantum dots. The ensemble was well characterized by two coherence times, indicating a faster dephasing of excited exciton states and a much longer ground-state dephasing time. The latter corresponds well to the minimum linewidths observed in micro-PL measurements. It is plausible to assume that below 5 K, exciton coherence times in excess of 1 ns can be obtained in self-assembled quantum dots. When considered together with recent advances in substrate prepatterning to accurately position the dots, the long coherence time makes this system an interesting candidate for the study of coherent interactions for quantum information processing. The rapid increase of linewidth with temperature, however, makes quantum dot devices operating under ambient conditions far from ideal and restricts suggested applications that rely on a narrow homogeneous linewidth, such as multi-channel detection [7] or amplification [167], to the low-temperature regime. On the other hand, the increase in homogeneous linewidth acts favorably for quantum dot lasers [168], and with state-

of-the art growth techniques [169], the inhomogeneous broadening can be reduced to a point where it is approaching the homogeneous broadening of the individual dots at room temperature. Coupled with a number of additional technological advantages [108], this makes self-assembled III-V quantum dots well suited for application in solid-state lasers and this issue is being pursued further, as a continuation of the present work.

Over the duration of this Ph.D. project, nearly 4000 scientific articles on semiconductor quantum dots have been published internationally. It is clear that this thesis only covers a minute part of the extensive developments that have occurred within this maturing field of research. Nevertheless, significant progress is yet to be made, especially in applying quantum dots to novel semiconductor devices, and continued advances in this field may be expected in the coming years.

References

[1] G. L. Snider, A. O. Orlov, I. Amlani, X. Zuo, G. H. Bernstein, C. S. Lent, J. L. Merz, and W. Porod, J. Appl. Phys. **85**, 4283 (1999).

[2] E.C. Behrman, L.R. Nash, J.E. Steck, V.G. Chandrashekar, and S.R. Skinner, Information Sciences **128**, 257 (2000).

[3] M. Bruchez, Jr., M. Moronne, P. Gin, S. Weiss, and A.P. Alivisatos, Science **281**, 2013 (1998).

[4] W.C.W. Chan and S. Nie, Science **281**, 2016 (1998).

[5] P. Recher, E.V. Sukhorukov, and D. Loss, Phys. Rev. Lett. **85**, 1962 (2000).

[6] S. Komiyama, O. Astafiev, V. Antonov, T. Kutsuwa, and H. Hirai, Nature **403**, 405 (2000).

[7] J.L Jimenez, L.R.C. Fonseca, D.J. Brady, J.P. Leburton, D.E. Wohlert, and K.Y. Cheng, Appl. Phys. Lett. **91**, 3558 (1997); D.J. Brady and J.L. Jimenez, in *1999 Digest of the LEOS Topical Summer Meeting* (IEEE, 1999), p. 3.

[8] S. Maenosono, C.D. Dushkin, S. Saita, and Y. Yamaguchi, Jpn. J. Appl. Phys. **39**, 4006 (2000).

[9] B. Lounis, H.A. Bechtel, D. Gerion, P. Alivisatos, and W.E. Moerner, Chem. Phys. Lett. **329**, 399 (2000).

[10] C. Santori, M. Pelton, G. Solomon, Y. Dale, and Y. Yamamoto, Phys. Rev. Lett. **86**, 1502 (2001).

[11] V. Zwiller, H. Blom, P. Jonsson, N. Panev, S. Jeppesen, T. Tsegaye, E. Goobar, M.-E. Pistol, L. Samuelson, and G. Bjork, Appl. Phys. Lett. **78**, 2473 (2000).

[12] Y. Arakawa and H. Sakaki, Appl. Phys. Lett. **40**, 939 (1982).

[13] M. Asada, Y. Miyamoto, and Y. Suematsu, IEEE J. Quantum Electron. **QE-22**, 1915 (1986).

[14] Y. Miyamoto, M. Cao, Y. Shinagi, K. Furuya, Y. Suematsu, K.G. Ravikumar, and S. Arai, Jpn. J. Appl. Phys. **26**, L225 (1987).

[15] N. Kirstaedter, N.N. Ledentsov, M. Grundmann, D. Bimberg, V.M. Ustinov, S.S. Ruvimov, M.V. Maximov, P.S. Kop'ev, Zh.I. Alferov, U. Richter, P. Werner, U. Gösele, and J. Heydenreich, Electron. Lett. **30**, 1416 (1994).

[16] J.W. Strutt, Phil. Mag. **41**, 107 (1871).

[17] C. Christiansen, Ann. Phys. **23**, 298 (1884).

[18] J.A. Dobrowolski, in *Handbook of optics*, W.G. Driscoll, ed. (McGraw-Hill Book Company, 1978)).

[19] A.I. Ekimov, Al.L. Efros, and A.A. Onushchenko, Solid State Commun. **56**, 921 (1985).

[20] R. Dingle, W. Wiegmann, and C.H. Henry, Phys. Rev. Lett. **33**, 827 (1974).

[21] C. Weisbuch and B. Vinter, *Quantum Semiconductor Structures* (Academic Press, 1991).

[22] N. Peyghambarian, S.W. Koch, and A. Msyrowicz, *Introduction to Semiconductor Optics* (Prentice Hall, 1993).

[23] C.F. Klingshirn, *Semiconductor Optics* (Springer, 1995).

[24] P.Y. Yu and M. Cardona, *Fundamentals of Semiconductors* (Springer, 1996).

[25] C. Weisbuch and B. Vinter, *Quantum Semiconductor Structures* (Academic Press, 1991).

[26] J. Shah, *Ultrafast Spectroscopy of Semiconductors and Semiconductor Nanostructures* (Springer, 1999).

[27] R. Loudon, *The Quantum Theory of Light* (Oxford Science Publications, 1997).

[28] D. Bimberg, M. Grundmann, and N.N. Ledentsov, *Quantum Dot Heterostructures* (John Wiley & Sons, 1999).

[29] M. Sugawara, ed., *Self-Assembled InGaAs/GaAs Quantum Dots*, Semiconductors and Semimetals, Vol. 60 (Academic Press, 1999).

[30] A. Zunger, ed., MRS Bulletin, **23(2)** (1998).

[31] D. Gammon, B.V. Shanabrook, and D.S. Katzer, Phys. Rev. Lett. **67**, 1547 (1991).

[32] R. Heitz, I. Mukhametzhanov, O. Stier, A. Madhukar, and D. Bimberg, Phys. Rev. Lett. **83**, 4654 (1999).

[33] J. Behrend, M. Wassermeier, W. Braun, P. Krispin, and K.H. Ploog, Phys. Rev. B **53**, 9907 (1996).

[34] K. Ploog, J. Crystal Growth **174**, 522 (1997).

[35] J. Shumway, A.J. Williamson, A. Zunger, A. Passaseo, M. DeGiorgi, R. Cingolani, M. Catalano, and P. Crozier, Phys. Rev. B **64**, 125302 (2001).

[36] N. Liu, J. Tersoff, O. Baklenov, A.L. Holmes, Jr., and C.K. Shih, Phys. Rev. Lett. **84**, 334 (2000).

[37] R. Zimmermann and E. Runge, phys. stat. sol. **164**, 523 (1997).

[38] A. Zrenner, L.V. Butov, M. Hagn, G. Abstreiter, G. Böhm, and G. Weimann, Phys. Rev. Lett. **72**, 3382 (1994).

[39] K. Brunner, G. Abstreiter, G. Böhm, G. Tränkle, and G. Weimann, Appl. Phys. Lett. **64**, 3320 (1994).

[40] H.F. Hess, E. Betzig, T.D. Harris, L.N. Pfeiffer, and K.W. West, Science **264**, 1740 (1994).

[41] A. Gustafsson, M.-E. Pistol, L. Montelius, and L. Samuelson, J. Appl. Phys. **84**, 1715 (1998).

[42] N.H. Bonadeo, G. Chen, D. Gammon, D.S. Katzer, D. Park, and D.G. Steel, Phys. Rev. Lett. **81**, 2759 (1998).

[43] N.H. Bonadeo, J. Erland, D. Gammon, D. Park, D.S. Katzer, and D.G. Steel, Science **282**, 1473 (1998).

[44] J.R. Guest, T.H. Stievater, G. Chen, E.A. Tabak, B.G. Orr, D.G. Steel, D. Gammon, and D.S. Katzer, Science **293**, 2224 (2001).

[45] Q. Wu, R.D. Grober, D. Gammon, and D.S. Katzer, Phys. Rev. Lett. **83**, 2652 (1999).

[46] J.R. Jensen, J.M. Hvam, and W. Langbein, J. Appl. Phys. **86**, 2584 (1999).

[47] J.R. Jensen, *MBE-Grown Semiconductor Nanostructures with Electronic and Photonic Confinement*, Ph.D. thesis (Technical University of Denmark, 2001).

[48] W. Langbein, *Vielteilcheneffekte und Ladungsträgerdynamik in Typ-II-Übergitterstrukturen*, Ph.D. thesis (Universität (TH) Karlsruhe, 1995).

[49] Code supplied by R. Ferreira.

[50] I. Magnusdottir, private communication.

[51] C.B. Sørensen, *MBE-Growth, Processing and Characterization of Low-Dimensional GaAs/AlAs Heterostructures*, Ph.D. thesis (Technical University of Denmark, 1998).

[52] E.C. Lightowlers, in *Growth and Characterisation of Semiconductors*, R.A. Stradling, P.C. Klipstein, ed. (Adam Hilger, Bristol, 1990) p. 135.

[53] P.M. Petroff, S.P. Denbaars, Superlattices and Microstructures **15**, 15 (1994).

[54] H. Li, Q. Zhuang, Z. Wang, and T. Daniels-Race, J. Appl. Phys. **87**, 188 (2000).

[55] O. Baklenov, D.L. Huffaker, A. Anselm, D.G. Deppe, and B.G. Streetman, J. Appl. Phys. **82**, 6362 (1997).

[56] Y. Nakata, Y. Sugiyama, and M. Sugawara, *Molecular Beam Epitaxial Growth of Self-Assembled Quantum Dots*, in Ref. [29], p. 117.

[57] P. Rai-Choudhury, ed., *Handbook of Microlithography, Micromachining, and Microfabrication, Vol. 1* (SPIE Press, 1997).

[58] C. Walther, R.P. Blum, H. Niehus, W.T. Masselink, and A. Thamm, Phys. Rev. B **60**, R13962 (1999).

[59] E.H. Rhoderick, *Metal-Semiconductor Contacts* (Clarendon Press, 1978).

[60] T.P. Chen, Y.L. Luo, S. Fung, and C.D. Beling, Solid State Commun. **102**, 833 (1997).

[61] H. Gislason, *Growth and Optical Characterization of GaAs Quantum Wires*, Ph.D. thesis (Technical University of Denmark, 1997).

[62] A. Hartmann, Y. Ducommun, K. Leifer, and E. Kapon, J. Phys.: Condens. Matter **11**, 5901 (1999).

[63] H.P. Wagner, H.-P. Tranitz, H. Preis, W. Langbein, K. Leosson, J.M. Hvam, Phys. Rev. B **60**, 10640 (1999).

[64] F.A. Jenkins and H.E. White, *Fundamentals of Optics* (McGraw-Hill, 1981).

[65] C.J. Sansonetti, M.L. Salit, and J. Reader, Appl. Opt. **35**, 74 (1996).

[66] P.W. Milonni and J.H. Eberly, *Lasers* (John Wiley & Sons, 1988).

[67] F. Troiani, U. Hohenester, and E. Molinari, Phys. Rev. B **62**, R2263 (2000).

[68] P. Borri, W. Langbein, J. Mørk, J.M. Hvam, F. Heinrichsdorff, M.-H. Mao, and D. Bimberg, Phys. Rev. B **60**, 7784 (1999).

[69] K. Matsuda, K. Ikeda, T, Saiki, H. Tsuchiya, H. Saito, and K. Nishi, Phys. Rev. B **63**, 121304 (2001).

[70] W. Langbein, J.M. Hvam, and R. Zimmermann, Phys. Rev. Lett. **82**, 1040 (1999).

[71] W. Langbein and J.M. Hvam, in *Advances in Solid State Physics*, Vol. 39, B. Kramer, ed., 463 (Springer, 1999).

[72] J. Hegarty, M.D. Sturge, C. Weisbuch, A.C. Gossard, W. Wiegmann, Phys. Rev. Lett. **49**, 930 (1982).

[73] M. A. Herman, D. Bimberg, and J. Christen, J. Appl. Phys. **70**, R1 (1991).

[74] R. Zimmermann and E. Runge, J. Lumin. **60**, 320 (1994).

[75] Al.L. Efros, C. Wetzel, and J.M. Worlock, Phys. Rev. B **52**, 8384 (1995).

[76] V. Sa-yakanit, Ph. Roussignol, and G. Slavcheva, Phys. Rev. B **62**, 5079 (2000).

[77] H. Castella and J.W. Wilkins, Phys. Rev. B **58**, 16186 (1998).

[78] A. Melliti, M.A. Maaref, and R. Planel, J. Lumin. **78**, 25 (1998).

[79] R.F. Schnabel, R. Zimmermann, D. Bimberg, H. Nickel, R. Lösch, and W. Schlapp, Phys. Rev. B **46**, 9873 (1992).

[80] M. Gurioli, J. Martinez-Pastor, M. Colocci, A. Bosacchi, S. Franchi, and L.C. Andreani, Phys. Rev. B **47**, 15755 (1993).

[81] L.C. Andreani and A. Pasquarello, Phys. Rev. B **42**, 8928 (1990).

[82] S. Tarucha, H. Okamoto, Y. Iwasa, and N. Miura, Solid State Commun. **52**, 815 (1984).

[83] D. Bimberg, F. Heinrichsdorff, R.K. Bauer, D. Gerthsen, D. Stenkamp, D.E. Mars, and J.N. Miller, J. Vac. Sci. Technolog. B **10**, 1793 (1992).

[84] R.F. Kopf, E.F. Schubert, T.D. Harris, R.S. Becker, and G.H. Gilmer, J. Appl. Phys. **74**, 6139 (1993).

[85] R. Grousson, V. Voliotis, N. Grandjean, J. Massies, M. Leroux, and C. Deparis, Phys. Rev. B **55**, 5253 (1997).

[86] R.F. Kopf, E.F. Schubert, T.D. Harris, and R.S. Becker, Appl. Phys. Lett. **58**, 631 (1991).

[87] D. Gammon, B. V. Shanabrook, and D. S. Katzer, Appl. Phys. Lett. **57**, 2710 (1990).

[88] C.A. Warwick, W.Y. Jan, A. Ourmazd, and T.D. Harris, Appl. Phys. Lett. **56**, 2666 (1990).

[89] C.A. Warwick and R.F. Kopf, Appl. Phys. Lett. **60**, 386 (1992)

[90] B. Orschel, G. Oelgart, and R. Houdré, Appl. Phys. Lett. **62**, 843 (1993).

[91] J.C. Woo, S.J. Rhee, Y.M. Kim, H.S. Ko, W.S. Kim, and D.W. Kim, Appl. Phys. Lett. **66**, 338 (1995).

[92] Z.L. Yuan, Z.Y. Xu, B.Z. Zheng, C.P. Luo, J.Z. Xu, W. Ge, P.H. Zhang, and X.P. Yang, J. Appl. Phys. **79**, 1073 (1996).

[93] K. Fujiwara, H.T. Grahn, and K.H. Ploog, Phys. Rev. B **56**, 1081 (1997).

[94] M.K. Chin and C.P. Luo, J. Lumin. **79**, 233 (1998).

[95] A. Manassen, E. Cohen, A. Ron, E. Linder, and L.N. Pfeiffer, Phys. Rev. B **54**, 10609 (1996).

[96] D.S. Katzer, D. Gammon, and B.V. Shanabrook, J. Vac. Sci. Technolog. B **10**, 800 (1992).

[97] J. Hegarty, L. Goldner, and M.D. Sturge, Phys. Rev. B **30**, 7346 (1984).

[98] T. Takagahara, Phys. Rev. B **32**, 7013 (1985).

[99] D. Gammon, E.S. Snow, and D.S. Katzer, Appl. Phys. Lett. **67**, 2391 (1995).

[100] U. Jahn, S.H. Kwok, M. Ramsteiner, R. Hey, H.T. Grahn, and E. Runge, Phys. Rev. B **54**, 2733 (1996).

[101] D. Gammon, E.S. Snow, B.V. Shanabrook, D.S. Katzer, and D. Park, Science **273**, 87 (1996).

[102] D. Gammon, E.S. Snow, B.V. Shanabrook, D.S. Katzer, and D. Park, Phys. Rev. Lett. **76**, 3005 (1996).

[103] X. Fan, T. Takagahara, J.E. Cunningham, and H. Wang, Solid State Commun. **108**, 857 (1998).

[104] W. Langbein, K. Leosson, J.R. Jensen, J.M. Hvam, and R. Zimmermann, Phys. Rev. B **61**, R10555 (2000).

[105] V. Savona, S. Haacke, and B. Deveaud, Phys. Rev. Lett. **84**, 183 (2000).

[106] G. Malpuech, A. Kavokin, W. Langbein, and J.M. Hvam, Phys. Rev. Lett. **85**, 650 (2000).

[107] E. Runge and R. Zimmermann, phys. stat. sol. (b) **206**, 167 (1998).

[108] D. Bimberg, M. Grundmann, F. Heinrichsdorff, N.N. Ledentsov, V.M. Ustinov, A.E. Zhukov, A.R. Kovsh, M.V. Maximov, Y.M. Shernyakov, B.V. Volovik, A.F. Tsatsul'nikov, P.S. Kop'ev, Zh.I. Alferov, Thin Solid Films **367**, 235 (2000).

[109] M. Bayer, O. Stern, P. Hawrylak, S. Fafard, and A. Forchel, Nature **405**, 923 (2000).

[110] E.F. Duijs, F. Findeis, A. Zrenner, M. Bichler, and G. Abstreiter, phys. stat. sol. (b) **224**, 47 (2001).

[111] J. Tatebayashi, M. Nishioka, Y. Arakawa, Appl. Phys. Lett. **78**, 3469 (2001).

[112] L. Chu, M. Arzberger, G. Böhm, and G. Abstreiter, J. Appl. Phys. **85**, 2355 (1999).

[113] S. Fafard, Z.R. Wasilewski, C.Ni. Allen, D. Picard, M. SPanner, J.P. McCaffrey, and P.G. Piva, Phys. Rev. B **59**, 15368 (1999).

[114] A. Polimeni, A. Patane, M. Henini, L. Eaves, and P.C. Main, Phys. Rev. B **59**, 5064 (1999).

[115] Y.S. Kim, U.H. Lee, D. Lee, S.J. Rhee, Y.A. Leem, H.S. Ko, D.H. Kim, and J.C. Woo, J. Appl. Phys. **87**, 241 (2000).

[116] V.M. Ustinov, N.A. Maleev, A.E. Zhukov, A.R. Kovsh, A.Yu. Egorov, A.V. Lunev, B.V. Volovik, I.L. Krestnikov, Yu.G. Musikhin, N.A. Bert, P.S. Kop'ev, N.N. Ledentsov, and D. Bimberg, Appl. Phys. Lett. **74**, 2815 (1999).

[117] H.Y. Liu, X.D. Wang, J. Wu, B. Xu, Y.Q. Wei, W.H. Jiang, D. Ding, X.L. Ye, F. Lin, J.F. Zhang, J.B. Liang, and Z.G. Wang, J. Appl. Phys. **88**, 3392 (2000).

[118] F. Guffarth, R. Heitz, A. Schliwa, O. Stier, N.N. Ledentsov, A.R. Kovsh, V.M. Ustinov, and D. Bimberg, Phys. Rev. B **64**, 085305 (2001).

[119] J.S. Kim, P.W. Yu, J.Y. Leem, J.I. Lee, S.K. Noh, J.S. Kim, S.M. Kim, J.S. Son, U.H. Lee, J.S. Yim, and D. Lee, Appl. Phys. Lett. **78**, 3247 (2001).

[120] O. Madelung, ed., *Semiconductors: Group IV Elements and III-V Compounds*, Data in Science and Technology (Springer, 1991).

[121] M. Grundmann, Physica E **5**, 167 (2000).

[122] R.L. Sellin, Ch. Ribbat, M. Grundmann, N.N. Ledentsov, and D. Bimberg, Appl. Phys. Lett. **78**, 1207 (2001).

[123] E.C. Le Ru, P.D. Siverns, and R. Murray, Appl. Phys. Lett. **77**, 2446 (2000).

[124] L.V. Asryan and S. Luryi, IEEE J. Quantum Electron. **37**, 901 (2001).

[125] W.H. Jiang, X.L. Ye, B. Xu, H.Z. Xu, D. Ding, J.B. Liang, and Z.G. Wang, J. Appl. Phys. **88**, 2529 (2000).

[126] R. Leon, Y. Kim, C. Jagadish, M. Gal, J. Zou, and D.J.H. Cockayne, Appl. Phys. Lett. **69**, 1888 (1996).

[127] F. Heinrichsdorff, M. Grundmann, O. Stier, A. Krost, and D. Bimberg, J. Crystal Growth **195**, 540 (1998).

[128] W.H. Jiang, H.Z. Xu, B. Xu, X.L. Ye, J. Wu, D. Ding, J.B. Liang, and Z.G. Wang, J. Crystal Growth **212**, 356 (2000).

[129] N. Perret, D. Morris, L. Franchomme-Fossé, R. Côté, S. Fafard, V. Aimez, and J. Beauvais, Phys. Rev. B **62**, 5092 (2000).

[130] T. Otsuki, H. Aoki, H. Takagi, and G. Kano, J. Appl. Phys. **63**, 2011 (1988).

[131] M. Braskén, M. Lindberg, M. Sopanen, H. Lipsanen, and J. Tulkki, Phys. Rev. B **58**, R15993 (1998).

[132] S. Raymond, X. Guo, J.L. Merz, and S. Fafard, Phys. Rev. B **59**, 7624 (1999).

[133] S. Malik, E.C. Le Ru, D. Childs, and R. Murray, Phys. Rev. B **63**, 155313 (2001).

[134] S. Adachi, ed., *Properties of Aluminium Gallium Arsenide*, EMIS Datareviews Series No. 7 (INSPEC, IEE, 1993).

[135] X.-Q. Li, H. Nakayama, and Y. Arakawa, Phys. Rev. B **59**, 5069 (1999).

[136] Y. Toda, O. Moriwaki, M. Nishioka, and Y. Arakawa, Phys. Rev. Lett. **82**, 4114 (1999).

[137] M. Paillard, X. Marie, E. Vanelle, T. Amand, V.K. Kalevich, A.R. Kovsh, A.E. Zhukov, and V.M. Ustinov, Appl. Phys. Lett. **76**, 76 (2000).

[138] E. Dekel, D.V. Regelman, D. Gershoni, E. Ehrenfreund, W.V. Schoenfeld, and P.M. Petroff, Solid State Commun. **117**, 395 (2001).

[139] L. Besombes, K. Kheng, L. Marsal, and H. Mariette, Phys. Rev. B **63**, 155307 (2001).

[140] A. Kuther, M. Bayer, A. Forchel, A. Gorbunov, V.B. Timofeev, F. Schafer, J.P. Reithmaier, Phys. Rev. B **58**, R7508 (1998).

[141] J.J. Finley, A.D. Ashmore, A. Lemaître, D.J. Mowbray, M.S. Skolnick, I.E. Itskevich, P.A. Maksym, M. Hopkinson, and T.F. Krauss, Phys. Rev. B **63**, 073307 (2001).

[142] E. Dekel, D. Gershoni, E. Ehrenfreund, J.M. Garcia, and P.M. Petroff, Phys. Rev. B **61**, 11009 (2000).

[143] R. Rinaldi, S. Antonaci, M. DeVittorio, R. Cingolani, U. Hohenester, E. Molinari, H. Lipsanen, and J. Tulkki, Phys. Rev. B **62**, 1592 (2000).

[144] P. Borri, W. Langbein, J.M. Hvam, and F. Martelli, Phys. Rev. B **59**, 2215 (1999).

[145] H. Kamada, J. Temmyo, M. Notomi, T. Furuta, and T. Tamamura, Jpn. J. Appl. Phys. **36**, 4194 (1997).

[146] K. Ota, N. Usami, and Y. Shiraki, Physica E **2**, 573 (1998).

[147] K. Asaoka, Y. Ohno, S. Kishimoto, and T. Mizutani, Jpn. J. Appl. Phys. **38**, 546 (1999).

[148] P.G. Blome, M. Wenderoth, M. Hübner, R.G. Ulbrich, J. Porche, and F. Scholz, Phys. Rev. B **61**, 8382 (2000).

[149] H.D. Robinson and B.B. Goldberg, Phys. Rev. B **61**, R5086 (2000).

[150] R.G. Neuhauser, K.T. Shimizu, W.K. Woo, S.A. Empedocles, and M.G. Bawendi, Phys. Rev. Lett. **85**, 3301 (2000).

[151] J. Seufert, R. Weigand, G. Bacher, T. Kümmell, A. Forchel, K. Leonardi, and D. Hommel, Appl. Phys. Lett. **76**, 1872 (2000).

[152] V. Türck, S. Rodt, O. Stier, R. Heitz, R. Engelhardt, U.W. Pohl, D. Bimberg, and R. Steingrüber, Phys. Rev. B **61**, 9944 (2000).

[153] L. Pavesi and M. Guzzi, J. Appl. Phys. **75**, 4779 (1994).

[154] S. Raymond, J.P. Reynolds, J.L. Merz, S. Fafard, Y. Feng, and S. Charbonneau, Phys. Rev. B **58**, R13415 (1998).

[155] W. Heller, U. Bockelmann, and G. Abstreiter, Phys. Rev. B **57**, 6270 (1998).

[156] P. Borri, W. Langbein, S. Schneider, U. Woggon, R.L. Sellin, D. Ouyang, and D. Bimberg, Phys. Rev. Lett. **87**, 157401 (2001).

[157] T. Takagahara, Phys. Rev. B **60**, 2638 (1999).

[158] O. Stier, M. Grundmann, and D. Bimberg, Phys. Rev. B **59**, 5688 (1999).

[159] L.-W. Wang, J. Kim, and A. Zunger, Phys. Rev. B **59**, 5678 (1999).

[160] G. Cipriani, M. Rosa-Clot, and S. Taddei, Phys. Rev. B **61**, 7536 (2000).

[161] D. Birkedal, J. Bloch, J. Shah, L.N. Pfeiffer, and K. West, Appl. Phys. Lett. **77**, 2201 (2000).

[162] L.M. Smith, K. Leosson, J. Erland, J.R. Jensen, J.M. Hvam, and V. Zwiller, phys. stat. sol. (b) **224**, 447 (2001).

[163] D. Birkedal, K. Leosson, and J.M. Hvam, Phys. Rev. Lett. **87**, 227401 (2001).

[164] J. Kuhl, E.J. Mayer, G. Smith, R. Eccleston, D. Bennhardt, P. Thomas, K. Bott, and O. Heller, in *Coherent Optical Interactions in Semiconductors*, R.T. Phillips, ed. (Plenum Press, 1994).

[165] X.-Q. Li and Y. Arakawa, Phys. Rev. B **60**, 1915 (1999).

[166] D.S. Citrin, Phys. Rev. Lett. **69**, 3393 (1992).

[167] R.P. Mirin, D.J. Blumenthal, in *OSA Trends in Optics and Photonics. Advanced Semiconductor Lasers and their Applications*, L. Hollberg and R.J. Lang, eds., **31**, 183 (2000).

[168] M. Sugawara, K. Mukai, Y. Nakata, H. Ishikawa, and A. Sakamoto, Phys. Rev. B **61**, 7595 (2000).

[169] X.-D. Wang, Z.-C. Niu, S.-L. Feng, and Z.-H. Miao, Chinese Phys. Lett. **18**, 608 (2001).